BIOFABRICATION OF MUSCULAR AND NEURONAL *IN-VITRO* TISSUE FOR MULTI-CELLULAR ENGINEERED LIVING SYSTEMS

BY

GELSON J PAGAN-DIAZ

DISSERTATION

Submitted in partial fulfillment of the requirements
for the degree of Doctor of Philosophy in Bioengineering
in the Graduate College of the
University of Illinois at Urbana-Champaign, 2020

Urbana, Illinois

Doctoral Committee:

Professor Rashid Bashir, Chair
Professor Martha Gillette
Associate Professor Mattia Gazzola
Professor Joon Kong

ABSTRACT

The ability of designing, biofabricating and programming engineered tissue constructs, as well as modularly assembling them to achieve the engineering of heterotypic living systems is a key element for the progress of "New Biology". This perspective consists of utilizing engineering concepts for design of complex systems and combining with the principles and properties of multiple disciplines in cellular biology at various length scales to drive composition of living material that are organized in a way that allows for the emergence of novel functionalities. Advances in this field can constitute an experimental platform that can guide the discovery of factors that allow the emergence of properties that can translate into a richer toolbox with which to address real world problems.

One important example is the development of biological machines, namely consisting of motor neurons as a source of processing and activation and skeletal muscle as the actuator of the system. Towards this goal, advances in the generation of a neuro-muscular driven machine require an expansion of design parameters and arrangement of the assembled parts, guided by parameters established by natural processes. This dissertation presents advances on the expansion of this toolbox for the engineering of multicellular living systems consisting of muscle calls and motor neurons. The dissertation focuses on the modulation of the electrical activity of motor neuronal networks, the biofabrication of neural tissue containing motor neurons, and the redesigning of previous muscle-based walking robots for higher force generation.

First of all, the ability to uncover *in-vitro* methods to "reprogram" neural networks responsible for guiding the actuation of muscle is critical to engineer the dynamic functionalities needed in these biological machines. In this work, motor neurons were differentiated from mouse embryonic stem cells, which have been transfected to express a GFP reporter under the Hb9 promoter as well as Channelrhodopsin, to enable optogenetic stimulation of these neurons, which was used to design the training regimens. Past efforts have not considered reprogramming in terms of evoking long-term changes in firing patterns of in-vitro networks by training regimens during stages of neural development. Thus, in this dissertation, short and long-term programming of neural networks was explored by using optical stimulation to induce training regimens implemented during neurogenesis and synaptogenesis, and ultimately demonstrating correlation between these and the resulting plastic responses.

Furthermore, to design multicellular engineered living systems subunits that could facilitate the assembly of heterotypic biological machines, a novel biofabrication approach is proposed to form functional in-vitro neural tissue mimics (NTM) using mouse embryonic stem cells, a fibrin matrix, and 3D printed molds. This method can provide a large degree of design flexibility for development of in-vitro functional neural tissue models of varying shapes and forms for applications in the developments of engineered living systems for therapeutic biomedical research, drug discovery and disease modeling, and new engineering and research models. This type of biological manufacturing method is a good representation of the utilization

and expansion of biological design principles to guide the creation of self-organized complex functional structures, thus enriching the toolbox for the top-down engineering approach.

Finally, the development of skeletal muscle driven biological machines require optimized approaches for design given the mechanical dynamics between the actuating muscle and the scaffold. This means that advancing these biologically driven soft robots will involve employing different scaffold geometries and cellular constructs to enable a controllable emergence for increased production of force and functionality. Having the flexibility of altering geometry while ensuring tissue viability can enable advancing functional output from these machines through the implementation of new construction concepts and fabrication approaches. Furthermore, a forward engineering approach was developed to design next generation biological machines via direct numerical simulations and subsequent fabrication of high force producing biological machines.

The present thesis aims to propose the development of building blocks and modular technologies surrounding the realization of motor neuronal driven machines, through the implementation of effective training regimens to reprogram neural networks, implementing biofabrication techniques for neural tissues and optimizing design and scaling force produced by the muscle actuators in these biological machines. These stepwise enhancements in the engineering of the subunits are critical for the successful assembly of more complex structures and our understanding of how to build on these designs towards solving real world problems in medicine, environment, and manufacturing.

ACKNOWLEDGEMENTS

I would like to thank Dr. Rashid Bashir, for his outstanding guidance, mentorship and patience in this formative process, as well as for consistently leading by example. I would also like to thank the National Science Foundation Graduate Research Fellowship (Grant No. DGE-1144245) and the National Science Foundation Research Traineeship-Miniature Brain Machinery (Grant No. 1735252) for funding me during these years. Furthermore, I would like to acknowledge National Science Foundation Science and Technology Center Emergent Behavior of Integrated Cellular Systems (Grant No. 3939511) for supporting this research.

I am also very grateful to Professors M Taher A Saif, Martha Gillette, Joon Kong, Mattia Gazzola, Manu Platt and Roger Kamm for their guidance, inspiration and words of encouragement. Thank you to Ritu Raman and Caroline Cvetkovic for your mentorship throughout these years. Thank you to my colleagues, Tanmay Ghonge, Anurup Ganguli, Yongdeok Kim, Lauren Grant and Simone Douglas, for your companionship, conversation, friendship and moral support. Specially, thank you to Onur Aydin for all the conversations. I am excited for being your colleague in our field for many more years to come. Thank you, Krista Smith, Christian Konopka and Ian Berg for your amazing friendship across these years.

Finally, thank you Gelson Pagan and Teresita Diaz for being my role models, my support system and going above and beyond to teaching me tools and values that guide my everyday life and long-term goals, and James Martin for being the definition of passion for following your dreams throughout these years.

This thesis is dedicated first and foremost to T. D. A., the wind beneath my wings, and secondly to M. S. P., a true friend and a humble heart.

TABLE OF CONTENTS

CHAPTER 1: INTRODUCTION AND OVERVIEW

1.1 MOTIVATION

The field of engineering complex living systems *in-vitro* has been expanding as a subfield within tissue engineering for the past few decades(1, 2). This field consists of the development of biohybrid designs which take advantage of fabrication techniques to construct platforms which guide the functionality of biological tissue in order to achieve a desired function. These designs are being expanded with the interest of recapitulating a larger diversity of biological behaviors, which can serve to address real world biomedical problems such as modeling diseases for drug testing and development as well as for studying therapeutic approaches in regenerative medicine. On the other hand, a growing interest has been the modeling of phenomena of interest to study the emergence of biological properties in a more controlled setting through effective research models (3). This mindset consists of understanding the complexity of biological development, which can be exceedingly difficult through conventional means of observing live organisms. This is due in part to limitations on experimental freedom imposed by the organisms as well as technological constraints that currently exists. However, it is the very complexity of the organisms which composes the primary obstacles towards studying these complex phenomena. Thus, through the effort of trying to recapitulate these biomimetic properties in a lab setting, the goal is to become aware of what factors can be decoupled, which are essential for the property to emerge and to what extent.

This has led to the birth of the unique perspective of visualizing biological tissue as a material source.

From this viewpoint, biological cells are a material that has multiple unique properties: it can grow, heal, respond to outside stimulus and learn. Along that mindset, analogous to how engineering with metal has evolved from understanding each metal's physical property, (i.e. some metals being effective for electrical devices while others are more effective for building heavy physical structures), by understanding the biophysical, biochemical and biomechanical properties, the field will become more effective at engineering these *in-vitro* living systems. As the efforts have progressed, it has become clear the need to define design principles, or engineering principles which guide the use of biological knowledge towards recapitulating complex biological phenomena *in-vitro*. By a focused effort of creating a tissue engineering database, we can lay the grounds towards gaining a deeper understanding of how cooperative cell behavior leads to the formation of functional complex living systems. This would not only serve as an engineering-based approach of understanding the phenomena that happens in our bodies but would also serve to forward engineer these biohybrid systems to achieve more complex and, even perhaps, advanced functional outputs. This can have multiple positive repercussions in the way we study biological systems, as well as implement them for biomedicine.

These types of constructs can lead to development of more advanced "organ-on-chips" to allow for optimized disease modeling and in turn more efficient drug discovery and screening (2). On the other hand, realizing these systems with the expectation of addressing real-world problems through the engineering of biomimetic or bio-enhanced functionality gives the opportunity for development of unique and advantageous research models. This arises from the obstacles that currently limit the ability to engineer these multi-cellular living systems, as the

rules for the complexity that emerges during the interaction of biological structures at different levels of development still remains to be understood. Furthermore, one main engineering approach towards achieving these structures is a “top-down engineering” design and assembly of modular biological structures. It requires the use of mechanically and chemically guided differentiation of stem cells, with the goal of guiding the emergence of form and function. As a research model, development of these biological complex emergent systems can aid by addressing the question for the fundamental understanding of the biological design rules from a “top-down engineering” approach can potentially elucidate aspects and principles which would otherwise be too difficult to isolate from the complex phenomena involved.

1.2 BACKGROUND

Engineering of biological machines has been made possible by advances in biofabrication techniques. These machines have mostly involved the formation of biohybrid structures consisting of undifferentiated muscle cells being differentiated and installed on synthetic soft structures that direct actuation towards a design-specific functionality (4). These synthetic soft structures serve as scaffolds and have been manufactured through 3D printing of PEGDA, molding of PDMS or microfabrication of other such synthetic polymers (3, 5–10).

In the first generation of bio-machines, differentiated cardiac cells were effectively used as actuators, due to their spontaneous development of strong contractions (11). Furthermore, this initial biofabrication approach involved forming 2D sheets of differentiated muscle cells directly on soft polymer structures which bend when the cardiac muscle’s contractile forces are exerted directly on the polymer surface. In order to enhance experimental control on these biohybrid

systems, cardiac tissue was substituted with skeletal muscle, which contract only when globally stimulated. Furthermore, they have the added benefit of being able to interact with motor neurons, thus allowing for more advanced emergent behaviors to be recapitulated and engineered. This approach evolved greatly when it was discovered that cells embedded in a hydrogel would exert tactile forces on the soft surrounding environment, resulting in a compaction of the hydrogel-cell construct (12). This compaction would then permit the cell-cell interactions that enable myoblasts to fuse and differentiate into functional (i.e. contracting) myotubes.

This discovery has sparked numerous studies revolving the formation of 3D muscle constructs and has enabled the development of the biological robot, or bio-bot. It is composed of a 3D skeletal muscle tissue fitted around a 3D printed skeleton that is capable of walking due to the actuation of the muscle (13). This model has thus served as an experimental platform for the study and engineering of higher order functionalities of biological machines.

1.3 THESIS OVERVIEW

This dissertation is divided into three main chapters discussing improvements in biofabrication methodology for the engineering of *in-vitro* biological machines, represented on Figure 1-1 as a deconstruction of the approach towards specifically achieving biological machines actuated by muscle, driven by programmed neural signals.

The Chapter 2 proposes the integration of stimulus during the differentiation of motor neurons as a tool to enhance network responsivity to the stimulus after network formation. Furthermore, the chapter explores the resulting modulation of the neural network's electrical

activity's frequency profile when the stimulation during differentiation is coupled with stimulation during network formation.

The Chapter 3 presents the development of a protocol to enable the biofabrication of neural tissue. This will facilitate the integration processing capabilities of neurons to a diversity of experimental platforms, thus expanding the experimental freedom in neural related research design. The chapter first discusses the effects of cell concentration on tissue compaction and development and then proceeds to characterize the development of neural populations within the tissue with respect to intact 3D MEBs and well as its electrophysiological activity and interconnectivity. Furthermore, this chapter discusses the implementation of this protocol for the formation of human-derived engineered neural tissues.

The Chapter 4 proposes a redesign of the skeletal muscle-based biobot, by optimizing the process of modeling new structures which, through collaborative efforts, use predictive computational models that incorporate the inter-dynamics of muscle-to-scaffold. This new design algorithm used empirical biological data to propose a new design model to fabricate a larger and in turn stronger biobot, in order to facilitate the integration of motor neuronal tissues. This empirical data was then used to calibrate the computational model, to open the door for the efficient design of next generation muscle-driven biological machines.

The fifth and final chapters summarizes the findings in the context of the motivation and the field's state of the art. Furthermore, it discusses the applicability of this research to keep expanding the field in the realization of these engineered multi-cellular living systems, by

proposing next logical steps in this research as well as some exploratory ideas that could enhance the functionalities achieved in these findings. Finally, the chapter closes with closing remarks regarding the author's perspective on this quickly growing field of engineering biological machines through the combination of biomimicry and forward-engineering.

1.4 FIGURE

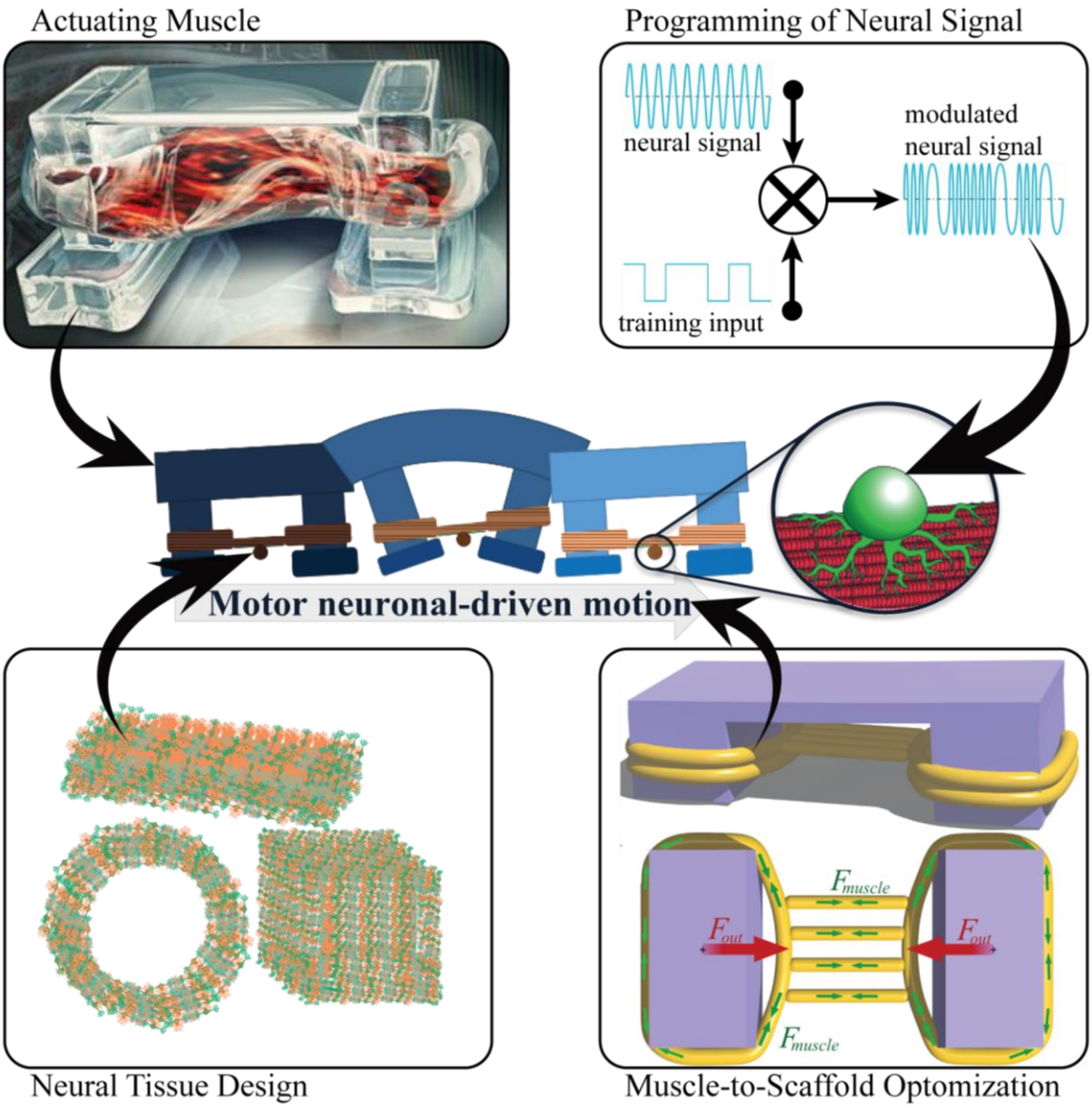

Figure 1-1. Engineering a motor neuronal driven biological machine requires various decoupled efforts. Previous works have developed a muscle-based platform. Presently there is a need to develop tools to be able to program and reconfigure neural sources to drive muscle actuation in a design specific fashion while also facilitating the assembly of the neural source on the muscle. Furthermore, optimizing the muscle-to-scaffold design would allow for more efficient transfer of force to movement as well as higher experimental freedom to achieve designs that also facilitate assembly.

1.5 REFERENCES

1. R. D. Kamm, R. Bashir, Creating living cellular machines. *Ann. Biomed. Eng.* **42**, 445–459 (2014).

2. R. D. Kamm, *et al.*, Perspective: The promise of multi-cellular engineered living systems. *APL Bioeng.* **2**, 040901 (2018).

3. R. M. Duffy, A. W. Feinberg, Engineered skeletal muscle tissue for soft robotics: fabrication strategies, current applications, and future challenges: Engineered skeletal muscle tissue for soft robotics. *Wiley Interdiscip. Rev. Nanomed. Nanobiotechnol.* **6**, 178–195 (2014).

4. R. Raman, R. Bashir, Biomimicry, Biofabrication, and Biohybrid Systems: The Emergence and Evolution of Biological Design. *Adv. Healthc. Mater.* **6**, 1700496 (2017).

5. L. Madden, M. Juhas, W. E. Kraus, G. A. Truskey, N. Bursac, Bioengineered human myobundles mimic clinical responses of skeletal muscle to drugs. *eLife* **4**, e04885 (2015).

6. O. Aydin, *et al.*, Neuromuscular actuation of biohybrid motile bots. *Proc. Natl. Acad. Sci.* **116**, 19841–19847 (2019).

7. Z. Li, *et al.*, Biohybrid valveless pump-bot powered by engineered skeletal muscle. *Proc. Natl. Acad. Sci.* **116**, 1543–1548 (2019).

8. C. Cvetkovic, *et al.*, Three-dimensionally printed biological machines powered by skeletal muscle. *Proc. Natl. Acad. Sci.* **111**, 10125–10130 (2014).

9. S. G. M. Uzel, *et al.*, Microfluidic device for the formation of optically excitable, three-dimensional, compartmentalized motor units. *Sci. Adv.* **2**, e1501429–e1501429 (2016).

10. A. W. Feinberg, Biological Soft Robotics. *Annu. Rev. Biomed. Eng.* **17**, 243–265 (2015).

11. V. Chan, *et al.*, Development of Miniaturized Walking Biological Machines. *Sci. Rep.* **2**, 1–8 (2012).

12. W. J. Polacheck, C. S. Chen, Measuring cell-generated forces: a guide to the available tools. *Nat. Methods* **13**, 415–423 (2016).

13. R. Raman, C. Cvetkovic, R. Bashir, A modular approach to the design, fabrication, and characterization of muscle-powered biological machines. *Nat. Protoc.* **12**, 519–533 (2017).

CHAPTER 2: MODULATING ELECTROPHYSIOLOGY OF MOTOR NEURAL NETWORKS VIA OPTOGENETIC STIMULATION DURING NEUROGENESIS AND SYNAPTOGENESIS[1]

2.1 INTRODUCTION

Inducing neuronal plasticity is one of the grand challenges in neuroengineering. Understanding and controlling nerve connectivity and their plasticity could have profound impacts in regenerative medicine (1–4), as studies have shown that engrafting Motor neuron containing Embryoid Bodies (MEBs) can improve recovery in motor nerve injuries(1, 3). The ability to enhance or control the electrophysiological functions of such MEBs could be used for improvement of motor function recovery. Furthermore, in the emerging field of engineering biohybrid neuronal-driven biological machines, it would be highly advantageous to forward-engineer programmable neural networks that could be installed within *in vivo* or *in vitro* systems in order to achieve targeted functional behaviors (5–7). While the mechanisms responsible for synaptic modulation and circuitry formation (i.e. memory and learning) have been studied in invertebrate and mammals, the complexity of neuronal plasticity pathways, such as potentiation and homeostatic plasticity, have made it difficult to control neural circuit development for *in vitro* applications (8). Furthermore, studies have shown varying degrees of emerging phenomena that

[1] This work is a reproduction of the following first authored journal article:
Gelson J. Pagán-Díaz, Jenny Drnevich, Karla P. Ramos-Cruz, Richard Sam, Parijat Sengupta, Rashid Bashir. Modulating behavior of motor neural networks via optogenetic stimulation during neurogenesis and synaptogenesis. *Scientific Reports*. 2019 (In revision)

Author Contributions: G.J.P.-D. performed the design, data acquisition and analysis, and writing of the manuscript; J.D. contributed by analyzing the RNA Sequencing data; K.P.R. and R.S. contributed with data acquisition and analysis; P.S. contributed to the conception, design of experiments, and editing of this manuscript.; R.B. led the project, the conception and design of experiments, contributed to data analysis, and edited the manuscript.

are correlated to neuronal plastic events that would imply "learning" or "memory storage" in neural circuits.(9–13) These varying degrees extend from neural mechanisms that regulate potentiation to feedback mechanisms with respect to associations to stimulation. Currently, *in vitro* micro electrode array (MEA) systems have aimed to study the effects of stimulation protocols in the resulting network dynamics for the past 30 years (13–19). While some of these studies have induced transient changes in the recorded signals, most have focused on changes of number of action potentials in mature primary neurons and in learning as a result of feedback to strengthen associations to the stimulation patterns. Due to the fact that these phenomena emerge from the multiple endogenous neuronal plasticity pathways, finding new approaches to enhance and modulate these plastic responses in a long-term way would be highly advantageous in the field.

Because most of these studies on plasticity have focused on modulation of mature neurons, we hypothesized that we could induce plasticity-related long-term electrophysiological changes in *in-vitro* neural networks, by implementing training regimens during early stages of differentiation, i.e. neurogenesis, coupled with training regimens during network formation, i.e. synaptogenesis. To this end, we used 465 nm pulsed light to induce depolarization in specific temporal patterns to implement a training regimen on differentiating channelrhodopsin (ChR2)-expressing motor neuronal embryoid bodies (MEBs) grown in suspension and continued the training regimen after seeding them on functionalized glass to allow for neurite extension and network development. In parallel, we seeded the MEBs on MEA chips while continuing training regimens to be able to characterize the network dynamics during network development. We first characterized responses to the optogenetic stimulation during neurogenesis by assessing morphological parameters, followed by analyzing the resulting electrophysiological responses including the network's synchronicity, firing patterns in power spectra and the system's responsivity to stimulation during

recording. These results showed a direct correlation between perturbations during differentiation and plastic responses occurring during network formation. Finally, through RNA sequencing studies, we observed genetic changes that serve to explain the observed modulations in these neuronal systems.

2.2 MATERIAL AND METHODS

2.2.1 MESC CULTURE AND DIFFERENTIATION

A feeder layer of myocin-C inactivated mouse embryonic fibroblast (MEF) was seeded at a cell density of ~3.5 x10^4 cells/cm^2 and cultured in DMEM (Dulbecco's modified Eagle's medium) supplemented with 1% fetal bovine serum, 1% L-glutamine and 1% penicillin-streptavidin. Subsequently, HB9:GFP transgenic mouse embryonic stem (mES) cells transfected with (Channelrhodopsin) ChR2-TdTomato were seeded on the feeder layer (mESC at a ratio of 1.5 mES cells per MEF. Media was changed to mESC proliferation medium and replaced daily.

Differentiation begun prior to mESC colonies coming in contact with one another. Cultures were trypsinized (0.05% Trypsin) after being exposed to embryonic stem cell differentiation medium (eDM) for an hour, and later seeded on 100 mL low adhesion dishes in 10 mL eDM. The next day, floating cells were collected to separate the culture from adhered non-neuronal lineages. On the following day, embryoid bodies (EBs) were replated in eDM supplemented with 1µM of retinoic acid (RA) (Sigma Aldrich, MA) and 1µM puromorphine (PM) (STEMCELL Technologies, MA). On D5, EBs were resuspended in eDM supplemented with RA and PM plus 10 ng/mL of growth factors, glial cell-derived neurotrophic factor (GDNF) and ciliary neurotrophic factor (CNTF) respectively. Media was changed daily.

2.2.2 MEA FABRICATION

Platinum micro-electrode array chip were fabricated on borofloat glass wafers following standard lithographic techniques. Photoresist LOR3A (MicroChem, MA, USA) was spun on clean substrates, followed by spin coated layer of photoactive S1805 (Dow Chemical Comp., MI). Spun substrates were exposed using an EVG 620 (i-line) aligner (EV Group Inc., Tempe, AZ) and developed. Ti/Pt (1:3) was later evaporated for a total thickness of 1000 Angstroms. To passivate traces between the detection area and contact pads, 300 nm of silicon nitride was deposited on the entire substrate using Plasma-Enhanced Chemical Vapor Deposition System (PlasmaLab International, WA). Finished chips were diced into 49 x 49 mm squares and fitted with acrylic wells bonded by Dow Corning Sylgard 184 (Ellsworth Adhesives, IL).

To ensure that thermally generated noise voltages were below membrane voltage fluctuations during neuronal electrical activity, electrode impedance was decreased through electrochemical treatment of the electrodes (21). Platinum black was formed on top of clean electrodes to achieve high surface area using a Gamry Reference 600 Potentiostat. The galvanostatic deposition was achieved by running a chronopotentiometry experiment at 2.83E-6 A/cm^2 vs. Ag/AgCl for 15 seconds in a solution of dihydrogen hexachloroplatinate (0.08 mM H_2PtCl_6-$6H_2O$, Sigma Aldrich, with 0.25 g/L of $(CH_3COO)_2Pb$ Alfa Aesar) for a total of 21.45 ng (1.71E-2 ng/μm^2) of crystallized platinum. The impedance reduction due to the platinum black deposition was examined by electrochemical impedance spectroscopy.

2.2.3 ELECTROPHYSIOLOGY RECORDING

MEA measurements were performed using a MEA 2100-Lite Amplifier (Multi Channel Systems MCS GmbH, Germany) at 37^{o}C. Electrical activity from ChR2+ MEBs cultured on MEA

were measured every other day. Measurements were performed in dark at a sampling rate of 10 kHz for 20 minutes in FS eDM with sealed covers to keep CO_2 concentration stable.

Optogenetic stimulation was performed using LED Driver (Doric Lenses, Quebec, Canada) attached to a single LED, Blue 465 nm with a Fiberoptic Patchcord for an incident intensity of 10 mW/mm^2 (Figure 2-1). Stimulation patterns were designed with Doric Neuroscience Studio. Optogenetic potentiation regimens were performed in a 3D printed casing which held the fiberoptic in place against the dish lid. During neurogenesis, stimulation was achieved by collecting MEBs and resuspending in a 35mm dish which fit in the 3D printed casing. During recording, stimulation was done by mechanically holding the fiberoptic against the MEA lid. Potentiation regimens consisted of 5ms pulses at 20Hz for one second every other second for 1 hour for a total of 1800 cycles, while stimulation during recording consisted of the same pattern for only 10 cycles at equidistant times during the 20 minutes recording sessions. Measurements and calculations of heat transfer from beam to the media showed that the energy imparted would cause temperature fluctuations of less than 1^oC, which are less than fluctuations from normal cell handling.

2.2.4 CRYO-SECTIONING

For phenotypic counting, EBs were sectioned and stained using adapted published protocols.(22) At D9, 20 EBs were sampled and fixed for 20 minutes in 4% paraformaldehyde. After washing with PBS, buffer was sequentially substituted with sucrose solutions (10% w/v, 20% w/v and 30% w/v). After an overnight wash at 30% w/v sucrose solution in 4^oC, EBs were embedded in OCT solution (Tissue-Tek, CA) and frozen on dry ice prior to storing in -20^oC. Molds were sectioned in 20µm thick layers unto SuperFrost Plus slides (ThermoFisher Scientific, MA) and air dried at room temperature for 1hr and followed by staining.

2.2.5 IMMUNOSTAINING AND IMAGING

Immunocytochemistry was performed on samples fixed with 4% paraformaldehyde and treated with 0.05% Triton-X. Permeabilized samples with blocked with 4% bovine serum albumin at 4^{o}C overnight. Samples were later stained with primary antibodies at 4^{o}C overnight, followed by staining of secondary antibodies at room temperature for 2 hrs. All antibodies were diluted in Antibody Diluent (ThermoFisher Scientific, MA). For phenotype quantification, MEBs were embedded in OCT solution and sectioned prior to staining. The used antibodies were 1) anti-NeuN antibody for neural populations, (clone A60, Alexa Fluor 555 conjugate), 2) anti-glial fibrillary acidic protein antibody for astrocyte populations, (clone GA5), 3) anti-oligodendrocyte transcription factor 2 protein antibody for oligodendrocyte populations, 4) anti-adenosine A_{2A} receptor protein antibody for excitatory populations, 5) anti-parvalbumin protein antibody for inhibitory populations and 6) DAPI as a nuclear stain. For synaptophysin clustering quantification between MEBs, the used primary antibody was anti-synaptophysin 1 polyclonal chicken antibody (Synaptic Systems, Germany). It was counter stained with goat anti-chicken IgY AlexaFluor 647 (Abcam, MA), respectively, along with DAPI as a nuclear stain. After washing overnight at 4^{o}C in blocking buffer, samples were mounted with Prolong Diamond antifade (ThermoFisher, MA) and imaged using Zeiss 880 Confocal microscope (Carl Zeiss Microscopy).

2.2.6 SCANNING ELECTRON MICROGRAPHS

SEM images were taken at 1kV after grounding the entire array through the contact pads, to avoid charging the insulating Nitride layer, at 100-300X magnification.

2.2.7 RNA EXTRACTION

Samples of MEBs were carefully collected and centrifuged at 14000 rpm for 15 minutes. After aspirating supernatant, samples were flash frozen using liquid nitrogen and immediately stored at -80°C, until mRNA extraction. Total RNA was collected and purified using the RNeasy Mini Kit Part 1 (Qiagen). The total RNA concentration was quantified using a Nanodrop spectrophotometer.

2.2.8 QUANTIFICATION AND STATISTICAL ANALYSIS

2.2.8.1 Spike/burst analysis

Multi-Channel Analyzer software was used for counting and analytically extracting temporal parameters of fast events. Raw data was digitally filtered using a 2^{nd} Order Butterworth high pass filter (cutoff frequency: 200 Hz). Action Potentials (APs), were detected as "spikes" by setting a threshold at 5x standard deviations from the noise magnitude distribution. Analysis of firing rate behaviors and burst parameters followed spike detection (citation for burst analysis). For this experiment, burst detection was defined by the following parameters:

- Max interval to start burst: 50 ms
- Max interval to end burst: 50 ms
- Min. interval between bursts: 100 ms
- Min. duration of burst: 50 ms
- Min. number of spikes in burst: 4

This analysis was done for active electrodes which were defined as electrodes which recorded at least 10 AP/min.

2.2.8.2 Spectral analysis

Spectral analysis was performed on the slow component of raw data to assess modulations in network behavior. Data extracted as ASCII files were filtered in MATLAB using Butterworth 2nd order high pass digital filter with a cutoff frequency of 200Hz. Spectral components in the frequency domain were obtained through Fast Fourier transform (FFT) between 0.1 – 200 Hz to remove DC components from data.

FFT was obtained for subsequent non-overlapping intervals of 10 s across the initial 4 minutes of spontaneous activity and normalized by the area under the curve. Calculated spectra were smoothed using a 3-point window moving average. Data was stored in 2D matrices, summed across electrodes and averaged across MEAs (n=3, mean ± std. dev, 2-tailed T-test).

2.2.8.3 Synaptophysin cluster counting

Stack images were superimposed for 10 microns in ImageJ. The Images were zoomed until 5-10 saturated pixels for SY38 were clear. Then a binary threshold was set so that only those pixels were conserved. Images were sampled ten times at regions between MEBs with a 150-by-150 µm area across three biological repeats by day (n=30, mean ± std. dev).

2.2.8.4 Quantifying network synchronicity

Overall network correlation was assessed through the automated use of spike data and a customized MATLAB code that calculated cross-correlation for discrete functions, as follows:

$$(f * g)[n] \stackrel{\text{def}}{=} \sum_{m=-\infty}^{\infty} f^*[m]g[m+n]$$

Here, f and g denote the discreet functions at point n, which represent the recorded MEA signals. Furthermore, f* denotes the complex conjugate and m is the lag or displacement, meaning

a feature in f occurring at n that occurs in g at n+m (23). Spike train data for each channel was cross-correlated with every other channel. Results were normalized so the autocorrelations have unit value at zero lag. The value at zero lag ($t_{ch\text{-}x}$=$t_{ch\text{-}y}$) was stored for each correlation in a 60-by-60 matrix relating every channel to each other and plotted as a heat map and a bar graph was used to plot the average. (n=3, mean ± std. dev, 2-tailed T-test).

2.2.8.5 RNA sequencing analysis

The RNA-seq libraries were prepared with Illumina's 'TruSeq Stranded mRNA-seq Sample Prep kit' (Illumina). The libraries were quantitated by qPCR and sequenced on one lane on a HiSeq 4000 for 101 cycles from one end of the fragments using a HiSeq 4000 sequencing kit version 1. Fastq files were generated and demultiplexed with the bcl2fastq v2.20 Conversion Software (Illumina). Adapters and low-quality bases were trimmed from reads using Trimmomatic(24) (v0.36) with parameters LEADING:28 TRAILING:28 MINLEN:30. The trimmed reads were quasi-mapped to Gencode's M19 transcriptome using Salmon(25) (v 0.8.2) with additional parameters –seqBias --gcBias --numBootstraps=30. Transcript expression value were summarized to the gene-level and corrected for average transcript length using the "lengthScaledTPM" method(26). TMM-normalized(27) log2 counts per million (cpm) values (prior.count = 3) were calculated and only genes with > log2(0.5 cpm) in at least 3 samples were analyzed using the limma-trend method(28). Three pairwise comparisons were made (C vs D2, S vs D2 and S vs C) and multiple testing correction was done separately for each comparison using the False Discovery Rate method(29); significant differential expression was indicated at FDR p-value < 0.05.

2.3 RESULTS

2.3.1 APPROACH TO MODULATION OF MESC DERIVED NEURAL CIRCUITS

Optogenetic stimulation was used on mESC-derived MEBs to implement training regimens during two important stages of neural development: neurogenesis (still in suspension) and synaptogenesis (seeded on functionalized glass or MEAs) (Figure 2-2a). Training regimens consisted of periodic stimulation with 5 ms pulses at 20 Hz for an hour (Figure 2-1). This regimen has been shown to enhance axonal growth (30), and thus would suggest that it could lead to a shift in structural potentiation in a neural network. The regimen was repeated every 24hrs as differentiation occurred within the EBs, with an expectation that consistent repetition would enhance the potentiation and cause long-term changes in the firing patterns of the network. Following established differentiation protocols of mESC towards mature motor neurons (31–33), the described training regimen was started at D2 of differentiation, at which point stem cells had been induced towards neuronal lineages, and specialization and maturation of motor neurons has been shown to take place in the subsequent 7 days (Figure 2-2b). Since the transcription factors that drove differentiation are light sensitive, media was changed every single day immediately after stimulation to ensure that stimulation effects on MEBs were not artifacts (i.e. false positives) caused by photodegradation of factors (Figure 2-3). Furthermore, since the differentiation was monitored with the expression of the motor neuronal marker Hb9 through a GFP reporter, the plateau of GFP expression between D8 and D9 (Figure 2-4), suggested that D9 was an appropriate time point for seeding the MEBs on glass. Thus, after these 7 days (D2-D9) of differentiation, stimulated (S) and non-stimulated (NS) cultures were seeded on MEA chips (Figure 2-2c). Careful seeding practices were applied to ensure that ~20 MEBs were seeded within the sensing area of the MEAs for a ~50% coverage by the MEBs (Figure 2-5). Seeding in this manner ensured empty

space between clusters for the extension of processes, even though some nearby clusters would start fusing into larger clusters. The resulting two groups of samples seeded on MEAs were further subdivided into two more experimental groups, referring to whether or not a training regimen was continued during network formation on chip for the consequent 15 days (D10-D25). For ease of discussion, S or NS prior to a colon (e.g. S:X or NS:X) will refer to the presence or lack thereof of stimulation, during neurogenesis, while S or NS written after a colon (e.g. X:S or X:NS), will indicate the presence or absence of stimulation during synaptogenesis (Figure 2-2a).

The electrical activity of the resulting neuronal cultures was measured with the MEA system and the raw data was filtered to remove low frequencies (<200Hz), to remove undesired voltage artifacts (e.g. stimulation artifacts), and extract action potentials recorded as spiking events (Figure 2-2d). A two-step procedure was used to remove false positives from the analyzed data: 1) the detection threshold was set so that it would not detect any spikes from the ground electrode, then 2) the recorded spikes at each electrode were inspected to ensure that the detected spikes had the appropriate voltage phases relating to action potentials: depolarization, depolarization and refractory period.

2.3.2 MEB CULTURES FORM ACTIVE NEURAL NETWORKS WITH EXCITATORY AND INHIBITORY POPULATIONS

In this work, neural networks were cultured from intact MEBs, in contrast to growing them as a monolayer after dissociation. The long-term goal of our study is the modulation of electrical activity of the MEBs with the goal of installing *in-vivo* or *in-vitro* experimental systems and modulating the functionality of the resulting interactions (Figure 2-4). When cultured in their intact form, MEBs tend to keep their spheroid shape, while extending membrane dense processes

which contain neurites that form networks as they undergo synaptogenesis (Figure 2-6a). Furthermore, dense web-like neurite structures form within the spheroid itself (Figure 2-6b) and positively stained for both excitatory (vGlut) and inhibitory (GAD65/67) receptors (Figure 2-6c).

Network formation was validated by exposing MEB cultures grown on MEAs (Figure 2-6d) to varying concentrations of commonly used exciting and inhibiting signaling molecules: L-glutamate, acetylcholine, cyclic AMP, cyclic GMP, GABA, norepinephrine etc. (Figure 2-6e). As expected, L-glutamate evoked an excitatory response to the point of cytotoxicity beyond 100 µM, while other excitatory neurotransmitters, acetylcholine and cyclic AMP, continued a gradual increase in firing rate with increasing concentrations. Cyclic GMP, another cyclic nucleotide similar in function as cAMP, failed to evoke any significant effect on firing rate. On the other hand, inhibitory neurotransmitters norepinephrine and GABA showed a gradual decrease in firing rates. The responses corroborated the development of endogenously active neural networks expressing different kinds of receptors. The observations that MEBs extend processes within the body itself while responding to both excitatory and inhibitory signaling molecules could led to the hypothesis that these MEBs could be forming intrabody circuits which could be “trained” during differentiation and have these changes last after network formation.

2.3.3 STIMULATION DURING NEUROGENESIS RESULTS IN MORPHOLOGICAL CHANGES IN MEB CULTURES

The effects of stimulation during differentiation were initially observed in neurite extension and presynaptic protein clustering. While it has been reported that neurite outgrowth would be enhanced if neural populations simultaneously underwent optogenetic stimulation (30), it was not clear if effects of the stimulation on MEBs done in suspension would still result in an increase in neurite extension when later seeded on chips, as this would indicate some stable long-

term changes in the neuronal system. To quantify this, S:NS and NS:NS MEBs were seeded at low confluence on gridded coverslips and imaged at 6 times every two hours on D10 (1 DIV) to quantify the number of extending neurites (Figure 2-7a). Observations showed a statistically relevant increase of number of neurites extended for S:NS samples, compared to NS:NS, which indicates an increased rate of neurite extension as a result of the stimulation during neurogenesis (Figure 2-7b). Next, we wanted to observe the effect of stimulation during differentiation on the propensity of the network to form synapses. To quantify this, the clustering of presynaptic synaptophysin stained with anti-SY38, was counted along individual neurites as well as per unit area between the groups NS:NS and S:S (Figure 2-7c). By D11 (2 DIV) S:S samples showed a ~2-fold increase of synaptophysin clusters per neurite than NS:NS samples (Figure 2-7d). This increase of pre-synaptic clusters per neurite combined with the increase in neurite extension, resulted in ~3-fold increase of synaptophysin clusters per unit area at D11 (Figure 2-7e). When monitoring the difference of pre-synaptic clusters per unit area at D13 and D15, the significant difference indicated that optogenetic stimulation during neurogenesis evoked physiological responses on two important aspects of neural network development: neurite extension and presynaptic clustering (Figure 2-7e).

2.3.4 MEB NETWORK SYNCHRONICITY IS AMPLIFIED BY STIMULATION DURING NEUROGENESIS AND SYNAPTOGENESIS

Network synchrony is a common parameter used to characterize a developing neural network, as it gives information on the network's plasticity and connectivity. Various studies have successfully shown that the presence of chronic stimulation results in improved network synchrony (34–36). In our study, we wanted to observe the long-term effects of stimulation

regimens on the network synchrony and determine if these effects were amplified or shifted when the training regimen during neurogenesis was extended during synaptogenesis. From the raster plots of the spontaneous activity recorded at D21, the increased level of synchronous activity was notable between NS:S and S:S samples versus S:NS and NS:NS (Figure 2-8a). This can be appreciated by the peaks above the raster plots, which correspond to a summation of the activity across all electrodes, where synchronous networks would result in discrete peaks whereas in samples that lacked coordinated firing, the resulting line plot seemed to lack any peaks.

Similarity between electrode recordings was characterized with cross-correlation in order to quantify synchronous behavior. Values for the similarity across the network were obtained by calculating cross-correlation for all electrode combinations (Figure 2-9). For this analysis, only spontaneous recording of active electrodes was used to quantify the long-term effects of the training regimen on steady state synchrony. When average correlation values per electrodes were mapped to their position on the chip, NS:S and S:S samples showed high synchrony level across the entire network for spontaneous recordings at D21 (Figure 2-8b). This showed that synchronous behavior extended across the entire network and was markedly higher for networks that were stimulated during synaptogenesis.

Interestingly, when the network wide mean synchronicity was calculated for each recording day, synchrony was higher for the samples that were stimulated during neurogenesis for the first two recordings at D11 and D13, yet for later recordings only the samples that continued with the training regimens during synaptogenesis (NS:S and S:S) maintained the observed increase of synchronicity (Figure 2-8c).

2.3.5 SPECTRAL DENSITY ELUCIDATES CHANGES IN STEADY STATE FIRING

Conventionally, electrophysiological behavior is characterized by firing rate during set epochs and burst parameters (Figure 2-10). However, when analyzing these parameters during spontaneous firing, there was no discernable trend in the change of long-term firing rate or burst parameters between experimental groups. However, when observing the high pass filtered recorded data during steady state on D25, there were deviations on how the firing is structured, despite the fact that no clear change in the amount of activity was observed (Figure 2-11a). We accredited this seeming conflict between the quantitative and qualitative data to the burst detection parameters. In order to avoid arbitrariness in the selection of these parameters, we decided to characterize the data in the frequency domain. For this reason, we focused on characterizing spontaneous firing recorded on MEAs by comparing changes in the power spectrums of recorded signals calculated through Fourier transforms (Figure 2-11b). To obtain spectral profiles, the recorded data was divided into 10-second-long contiguous windows and transformed to the frequency domain, thus representing the power spectrum as a function of time (Figure 2-11b). Focusing between 0.1-5 Hz, all samples except S:S, showed firing patterns that seemed to be more or less random. This spontaneous heterogeneous firing patterns can be expected from these cultures formed from MEBs, as they are a super-network composed of individual networks from within each MEB. On the other hand, S:S samples show a clear change in their frequency profile, where most of the spectral power fell within 0.1-1Hz.

An interesting point to note is that if the signal power is summed across the entire frequency range of interest, there is no difference between samples on any particular day (Figure 2-12). However, if the signal power is summed between the frequency range of 0.1-1Hz, there is a significant change between non stimulated during synaptogenesis (NS:NS, S:NS, NS:S) and

stimulated throughout development (S:S) (Figure 2-11c). Moreover, there is also a significant difference between NS:S, and S:S, which indicated that combined stimulation of both neurogenesis and synaptogenesis had an amplified effect than just stimulation during synaptogenesis.

2.3.6 NEUROGENETIC STIMULATION CHANGES THE OPTO-RESPONSE OF MEB NETWORKS

Another aspect of consideration on the effect of training MEBs during neurogenesis was whether the early stage perturbation has some effects on how the later-stage network would responds to the same perturbation. To study this, we recorded responses to optogenetic stimulation from sets of samples that had not undergone the training regimen during neurogenesis (Figure 2-13a), and compared them to those set that had undergone such regimen (Figure 2-13b). Initial observation showed a difference between how the networks responded when stimulated early in the network development (D11) versus more mature networks (D25). For example, when early networks, which had a low spontaneous firing rate (D11) were stimulated, there would be a very notable evoked response during stimulation followed by a quiescent state, where the network would barely fire before returning to the baseline spontaneous firing rate. In contrast, more mature networks (D25), would still show and evoked response during stimulation but would automatically return to baseline firing rate right after stimulation ceased. What was interesting was that the quiescent time after stimulation that early S:S networks would show, were notable shorter than those from the NS:S samples (Figure 2-13a-b). Moreover, at D25, while NS:S samples would return to the same baseline firing rate right after stimulation stopped, S:S samples showed a transient change in firing rate for several seconds after the stimulation stopped (Figure 2-13a-b). To quantify this behavior, the evoked firing rate

during stimulation (FR_{stim}) and the post-response firing rate (FR_{post}) was compared to the firing rate prior to stimulation (FR_{pre}) (Figure 2-13c). While the fold-change increase of firing rate FR_{pre} to FR_{stim} decreased with time, since more mature networks would have a higher baseline firing rate, when comparing the amount of evoked action potentials during stimulation (FR_{stim}/FR_{pre}), for all days of recording, S:S samples consistently responded more strongly to stimulation than NS:S samples (Figure 2-13d). Furthermore, the quiescent state response post-stimulation observed in early days (D11), reflected itself in FR_{post} being less than FR_{pre}. Nevertheless, this lag was shorter for the S:S samples than the NS:S, as evidenced by a significant increase in the S:S cohort's FR_{post}/FR_{pre} ratio (Figure 2-13e). Furthermore, at later days of network development, it was notable that FR_{post}/FR_{pre} was ~1 for NS:S, meaning that the steady state firing rate was indistinguishable from that immediately following the termination of stimulation. On the other hand, S:S samples showed FR_{post}/FR_{pre} values above 1 from D17 forwarding, indicating that the network would transiently increase in firing rate right after stimulation.

To further study how the training regimens affected network response, we also quantified the evoked response reflected in the network's synchronicity. For this purpose, raster-plots of the average values of cross-correlation (as calculated for the analysis in Figure 2-8) were calculated using 10 second bins across the entire 20 minutes of recording (Figure 2-13f). This showed that for NS:S samples, the network wide synchronicity did not respond consistently among the different days of recording, however for S:S samples (samples that underwent training regimen during neurogenesis as well) consistently showed transient increase in network synchronicity right after stimulation was implemented (Figure 2-13g).

2.3.7 CHANGES EVOKED BY STIMULATION DURING NEUROGENESIS RESULT IN GENETIC CHANGES

Given the effects on neurite extension, presynaptic clustering, frequency profiles and network response to stimulation that were observed as a result of the presence of training regimens on MEBs during neurogenesis, we proceeded to determine genetic changes that could provide possible mechanistic explanations. Total messenger RNA sequencing was performed and analyzed for stimulated (S) and non-stimulated (NS) MEBs at D9, as well as EBs at D2. The differentially expressed genes in MEBs that underwent training regimens during neurogenesis were compared to those that did not, both with respect to the genetic expression of MEBs sampled prior to differentiation (at D2). A total of 749 differentially expressed genes between S and NS with $p < 0.05$ were detected and clustered and color coded with respect to the differential expression of D2 (Figure 2-14a). There were 200 genes that were upregulated during control differentiation, but this upregulation was lessened for samples that underwent training regimen (black bar), while the upregulation of 172 genes was amplified for those same samples (red bar). On the other hand, there were 202 genes whose downregulation was stagnated for samples with training regimen (yellow bar). For 173 genes, the control downregulation was further amplified after stimulation (blue bar). Something important to note was that this observed differential expression did not include changes in phenotype populations, matching the immunostaining observations (Figure 2-15). This indicated that training regimen during differentiation did not seem to noticeably disrupt the rate of phenotype specification or generation of the neural populations that generally result from the differentiation protocol (Table 1). This suggests that training regimens affected other functional pathways rather than altering the differentiation of populations. For further analysis, a more stringent threshold ($p<0.0005$) was set to detect the

most promising genes as key factors for the behavioral changes seen in stimulated MEB cultures. This threshold resulted in 97 differentially expressed genes for the black cluster (Figure 2-14b), 63 differentially expressed genes for the red cluster (Figure 2-14c), 77 differentially expressed genes for the yellow cluster (Figure 2-14d) and 71 differentially expressed genes for the blue cluster (Figure 2-14e). From this pool, a thorough literature study was used to identify gene targets that had been reported to be related to known neural development and function (Table 2, Figure 2-16).

2.4 DISCUSSION

Engineering of neural circuits is a critical step for biomedicine as well as various neuroengineering efforts. This work aimed to expand upon previous findings on achieving long term modulation of a neural network's behavior.(10, 13, 16, 37–40). Here, we showed a direct relation between changes in network function and development and training regimens implemented during neurogenesis and synaptogenesis. To our knowledge there has been no electrophysiological characterization of mESC-derived neural networks' electrical response where a relationship between training during neurogenesis and synaptogenesis is examined. Furthermore, these effects were correlated and supported by RNA-seq studies, where we showed that the training regimen affected targets related to network development, rather than affecting the differentiation of neural populations. In mESC-derived embryoid bodies, stimulation during neurogenesis has shown that the system enters a heightened state for neurite extension, which could be correlated to enhanced network formation. Furthermore, our study suggests that the presence of stimulation during neurogenesis has caused the system to be more sensitive and responsive to external stimulation after network formation, which could have implications on research studies where MEBs are integrated in *in-vivo* nerve tissues that have suffered injury. By

implanting “trained” MEBs that have an enhanced responsiveness to stimulation, the therapeutic effects that have been observed could in turn be enhanced as well. (3)

Furthermore, spectral analysis proved to be a useful tool in order to quantify changes in network behavior that might be missed by simply comparing firing rates. While firing rate did not clearly reflect any alteration to the steady state, transforming the electrical signal to the frequency domain served as an informative descriptor of alterations in the network dynamics as a result of the training regimens. Using FFT to characterize the network’s firing patterns as a response to the training regimens during network formation complements various other network effects that have been observed in this study. Because consistent evoked firing will accelerate the potentiation of preferred synapses, it follows that the system will reach a higher level of synchrony which in turn suggest structured firing, as synchronous behavior would be more viable in a structured versus a sporadically firing network.

Another very notable observation was that training regimen during neurogenesis evoked changes in the way the system would respond to the same stimulation after the network had formed. During early culture on chip (D11-D15), stimulation would cause the system to enter a quiescent state following the forced state of rapid firing from the stimulation, yet this quiescent state was significantly shortened for samples that had been stimulated during neurogenesis. Moreover, these distinctions extended beyond early stages of network formation, which also manifested as prolonged transient increases of network synchrony. This is relevant because, while tetanic stimulation has been correlated to potentiation, no change in baseline firing rate was observed. Therefore, if no long-term changes had been caused by training regimen during neurogenesis, there should have been no reason for the optogenetically evoked firing rate on chip to have shown any differences to the NS:S counterparts. This enhancement of response in

samples that were subjected to a controlled perturbation during neurogenesis points to long-term systematic changes due to training regimen.

To further validate these observations, RNA sequencing was performed on MEBs showing that a large number of genes were found to have been differentially expressed as a result of the training regimen. To focus our findings, the search was narrowed to genes showing a fold change with $p<0.0005$ and key genes related to neural function were selected. Upon observation of this narrowed list, we found that following training regimen during neurogenesis the expression of key developmental genes Npdc1 and Crabp2 more closely resembles that of more mature tissue. Other differentially expressed genes implied an improved development of key neural aspects such as axonal and dendritic growth (Tuba1a) and nucleation of microtubules (Tubgcp4). Furthermore, stimulated MEBs seems to overexpress important factors related to vesicular signaling such as Snap47, Vamp2, Reep2, and more importantly Cacng7. More importantly, various genes are directly related to improved synaptic function and plasticity. For example, upregulation of Aplp1, Cnih2 and Insyn1 would be targets of interest that could account for the structured firing patterns and the changes in the network responses to evoked stimulation. Considering the change in expression of these genes related to vesicle transport, synaptic transmission and neural development, the observations of shorter quiescent times post-stimulation for samples that underwent training regimens could suggest that the training regimen enhanced the network for a quicker recovery from synaptic fatigue, which is an activity-dependent temporary inability of neurons to transmit signals(41). Moreover, it is worth noting that Cnih2 and Insyn1 are regulators of inhibitory signaling related to the slowing down of signal transmission to improve its reliability, yet a lot is unknown about how these targets affect larger scale pathways and neuronal function. While neuronal networks have gene expressions which

parametrize the range of functionality of a resulting circuit, little is understood about how a set point is determined and how to controllably shift that point. By continuing plasticity studies that target all stages of neural development and coupling them with genetic signatures, these questions might be better addressed. Moreover, expanding this study to obtain protocol-specific responses in gene expression would be crucial in understanding neural plasticity and learning mechanisms.

Nevertheless, the results presented in this study add a new dimension to neural circuit engineering, by taking advantage of the synergy between responses to stimulation during differentiation and the plasticity that emerges during network formation, and correlation to gene expression. This solidifies our initial hypothesis that implementing training regimens during early stages of neural circuit development should be considered as a critical factor for studying neural plastic phenomena. In order to further this study, improved training regimens and spatial stimulation patterns during neurogenesis and synaptogenesis could be used to further the characterization of the network response. Furthermore, this approach could be expanded to *in-vivo* systems in order to examine if these alterations in fact result in behavioral changes in a developing organism and if the enhancement of mESC-derived MEBs result in regeneration studies by enhancement recovery of nerve tissue injury.

2.5 FIGURES AND TABLES

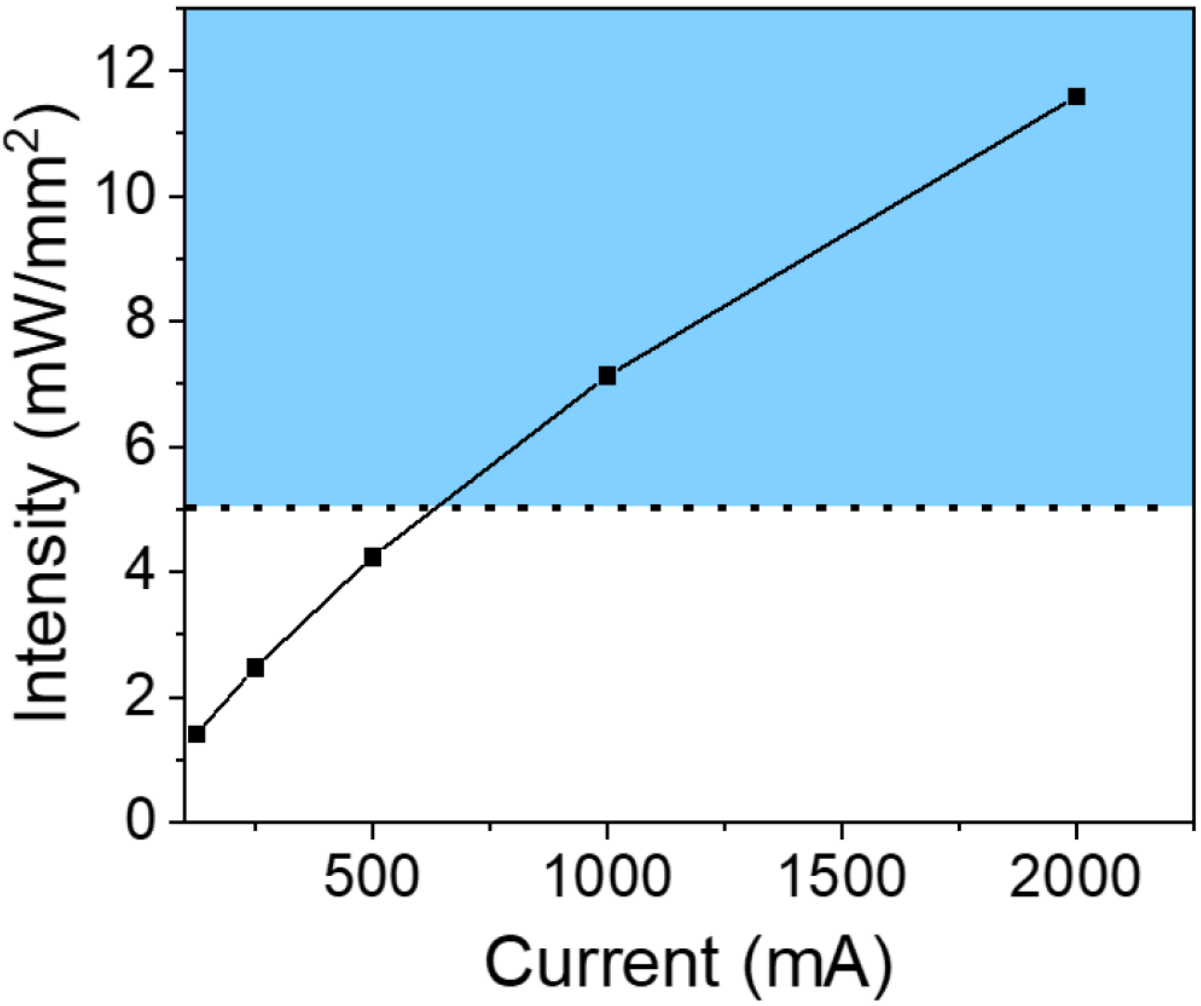

Figure 2-1. Light intensity measurements of the optogenetic 465nm laser as a function of the current. (blue region denotes adequate intensity to elicit a response from ChR2)

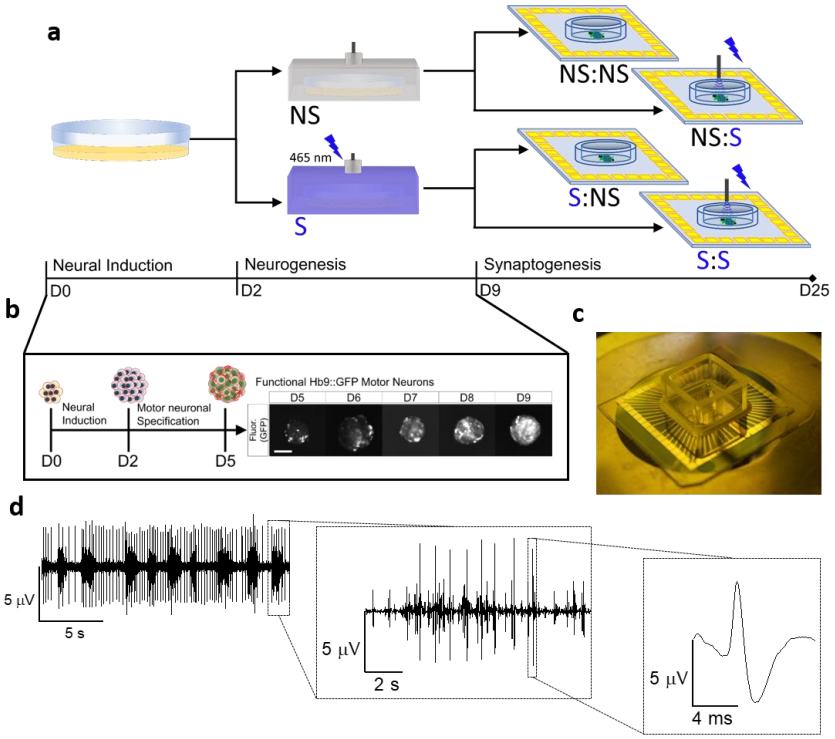

Figure 2-2 Approach to training mESC-derived motor neuronal embryoid body networks during neurogenesis and synaptogenesis. a Representative diagram of experimental setup combining differentiating ChR2 mESC's and MEAs. b Representative diagram of ChR2 mESC differentiation toward motor neuronal embryoid bodies monitored by the expression of GFP, guided by the motor neuronal specific Hb9 promoter (scale bar: 200 μm). c Representative image of fabricated MEA chip. d Representative spontaneous spike trains from MEA recordings of cultured embryoid body networks.

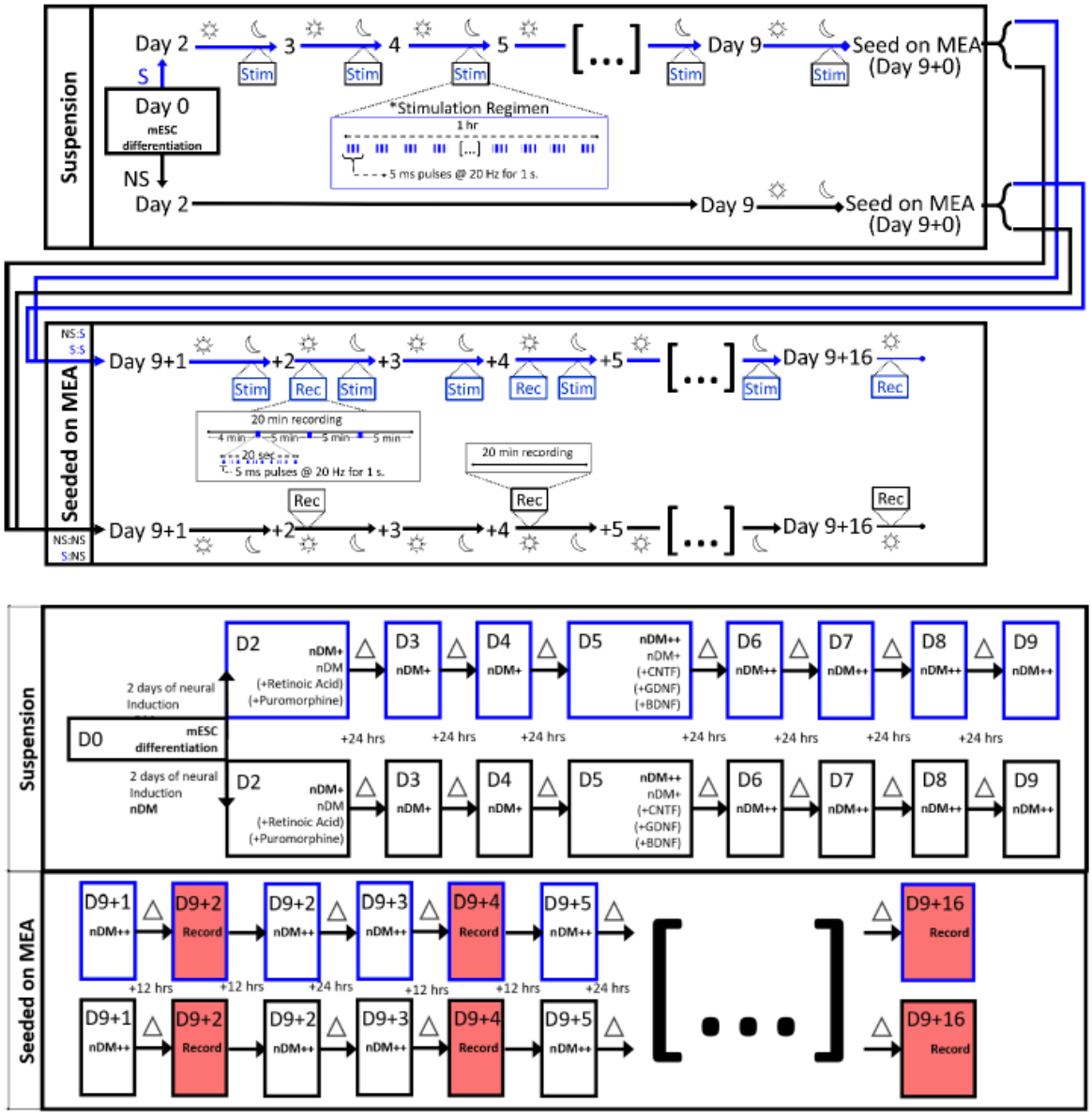

Figure 2-3. a Stimulation regimen for differentiating and on chip samples. b Feeding regimen for samples

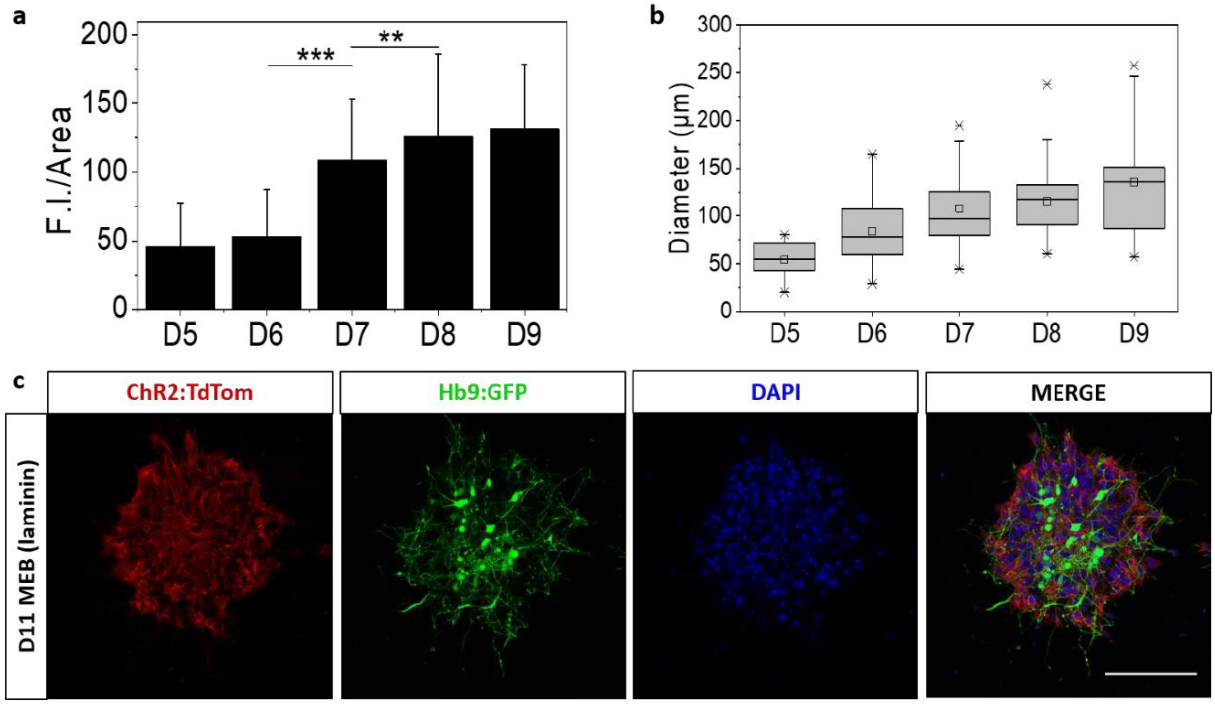

Figure 2-4. a Bar graph showing daily increase of HB9::GFP fluorescence during neurogenesis, normalized by the area of the embryoid bodies (n=20, mean ± std). **b** Box plots describing daily change in embryoid body diameter (n=20, perc. 25,75). **c** Representative image of MEB 2DIV seeded on laminin-coated glass. (Scale bar: 200 µm)

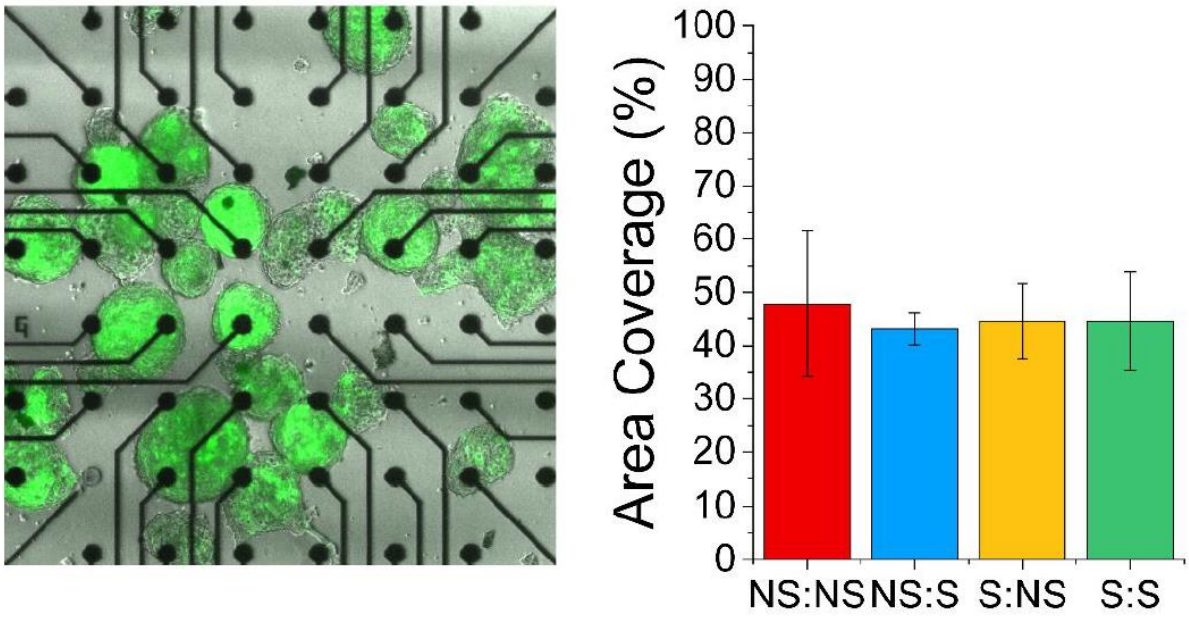

Figure 2-5 a. Average coverage of MEBs on the MEA sensing area between groups (n=3, mean± std).

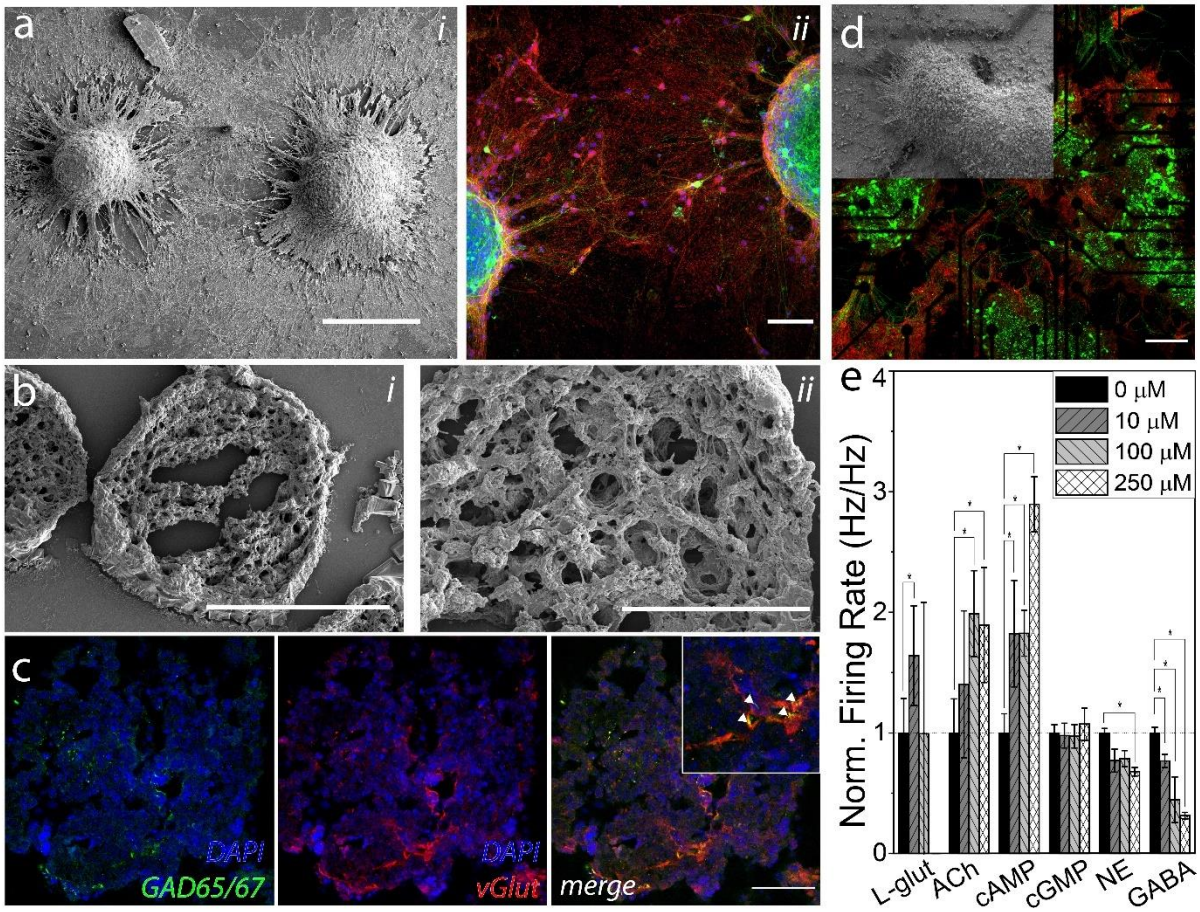

Figure 2-6. Intact MEBs indicate formation of internal networks and form active networks between them a i) Scanning electron micrograph of two embryoid bodies. (scale bar: 200 µm) and ii) confocal image showing dense clusters of synaptophysin between cultured embryoid bodies (scale bar: 50 µm). b i) MEB cryosections showing usual internal structure. (Scale bar: 50 µm) with ii) zoom in of internal structure of a sectioned embryoid body (scale bar: 15 µm). c Representative confocal image of MEB cryosection stained for GAD65/67 and vGlut. Triangles show GAD65/67 clusters d . Representative confocal image of entire field of view for neural culture grown on the MEA sensing area (scale bar: 200 µm) with scanning electron micrograph zoom in of embryoid bodies extending processes atop of sensing electrodes. e. Bar graph for average firing rate for consecutive 10 s windows for cultured embryoid body networks exposed to known neuronal signaling molecules at sequential addition of tonic baths of 10, 100 and 250 µM. (Glut: Glutamate; ACh: Acetylcholine; cAMP: cyclic AMP; cGMP: cyclic GMP; NE: norepinephrine; GABA: gamma-aminobutyric acid).(n=15, mean ± std). (* $p<0.05$; ANOVA with Tukey Post-hoc)

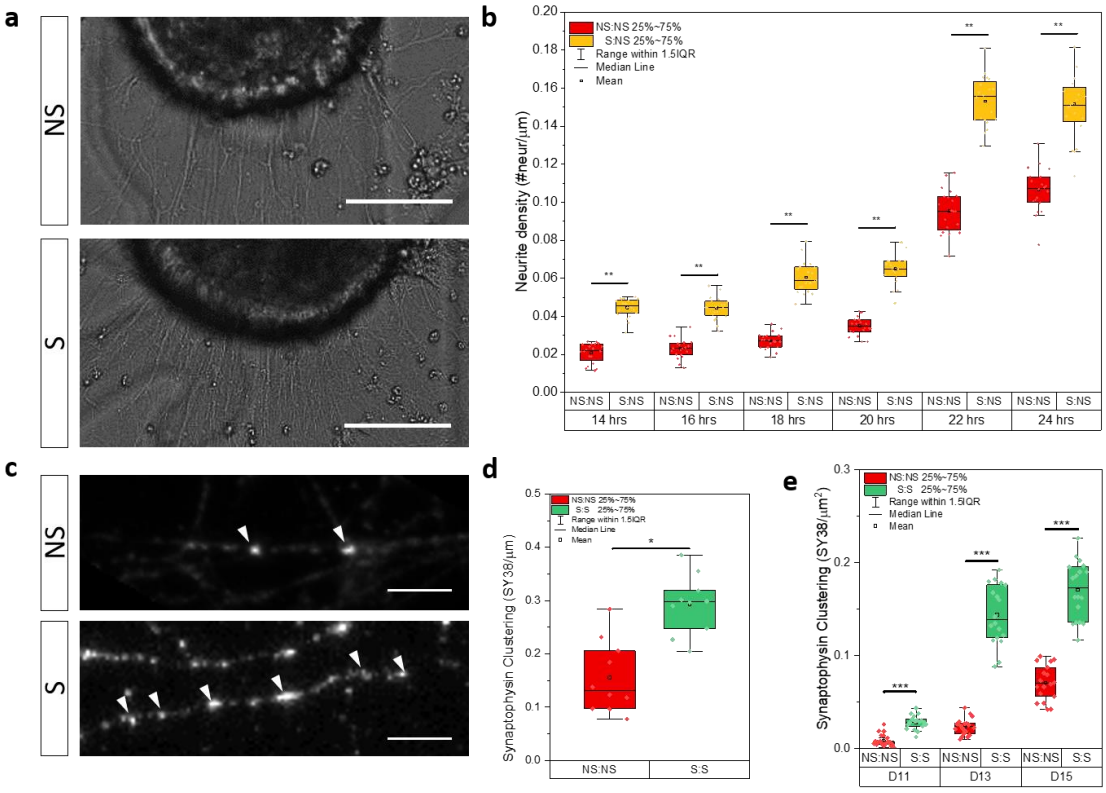

Figure 2-7. Stimulation during neurogenesis affects key morphological parameters of network formation. a. Representative phase contract images of neurite extension along the periphery of embryoid bodies between non-stimulated (NS) and stimulated during neurogenesis (S) samples (scale bar: 50 µm). b. Box plot quantifying the number of neurites protruding from the periphery of an embryoid body per length of the perimeter of the embryoid body for the second half of the first 24hrs after seeding (n=10). c. Representative fluorescence images of SY38 clustering at D11 along a neurite. Arrow denote SY38 clusters. (scale bar: 5 µm). d. Box plots of SY38 clusters along neurites for D11 (n=10). e. Box plots of SY38 clusters per unit area for D11-D15 (n=10) (*$p<0.05$, **$p<0.0005$, ***$p<10^{-5}$; two-tailed T-test).

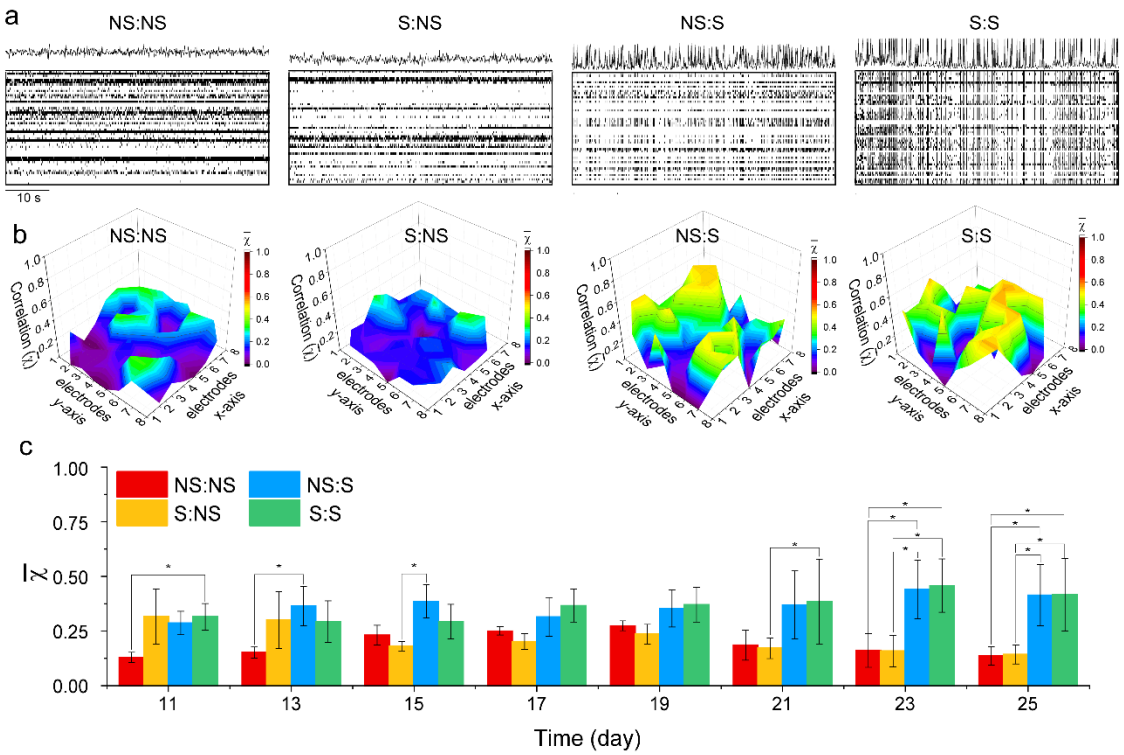

Figure 2-8. MEB network synchronicity is amplified by stimulation during neurogenesis and synaptogenesis. a. Representative rasterplots of MEB cultures at D25 showing network synchrony by line plots of the sum of active electrodes for each time point. b. The average correlation value (χ) was calculated for each electrode across time and active electrodes for a average value for each electrode, then mapped to their respective spatial position on the MEA array. d. The total average correlation value was calculated for active electrodes during spontaneous time of each culture for each day of recording. (n = 3, mean ± std). (*p<0.05; ANOVA with post-hoc Tukey)

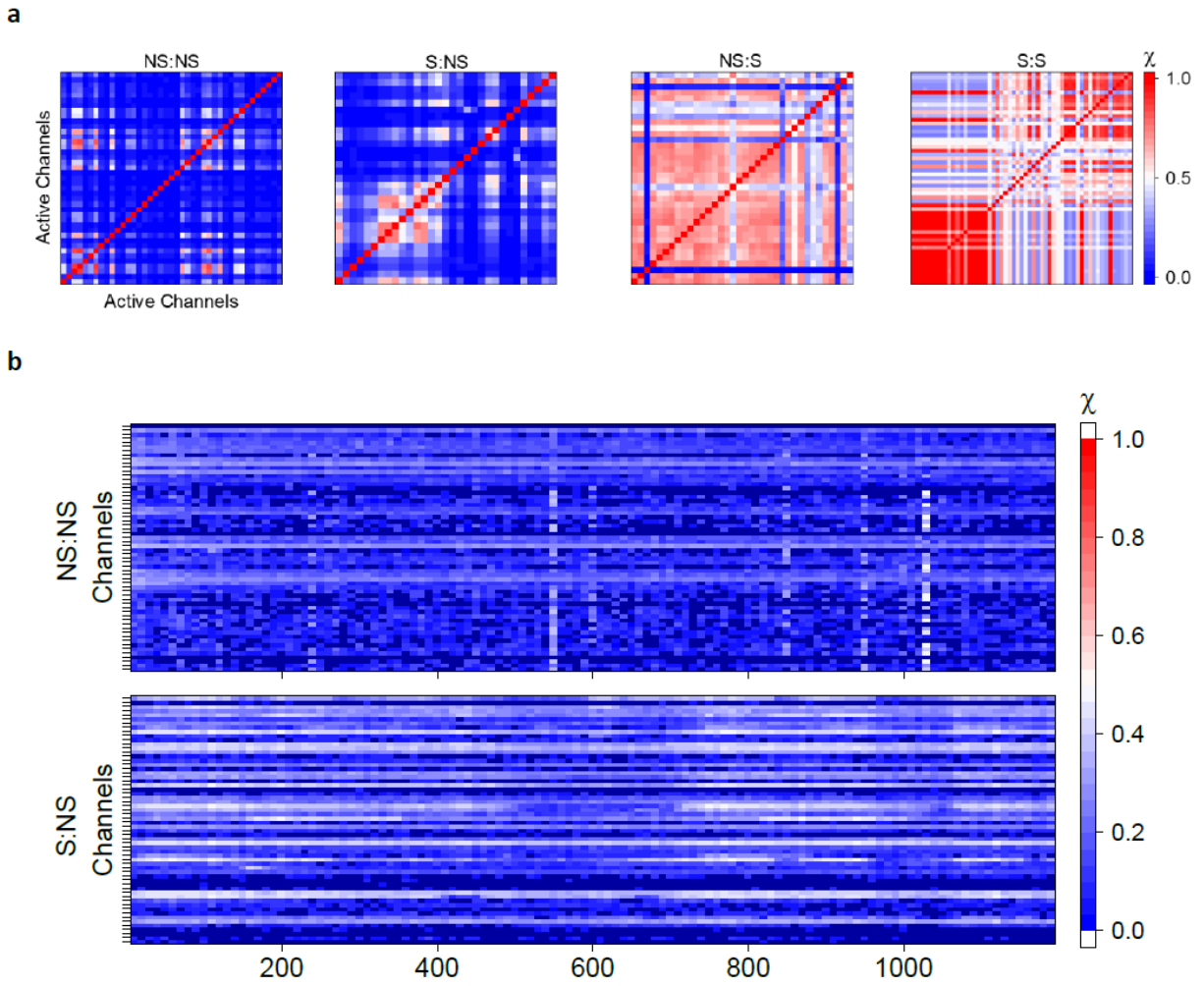

Figure 2-9 a Cross-correlation matrices of mean correlation value (χ) across for the entire time of spontaneous activity for each active electrode to every other active electrode. Matrices were normalized to singularity for auto-correlation. b Raster plot of average correlation value for each electrode during 10 s bins across the entire recording time.

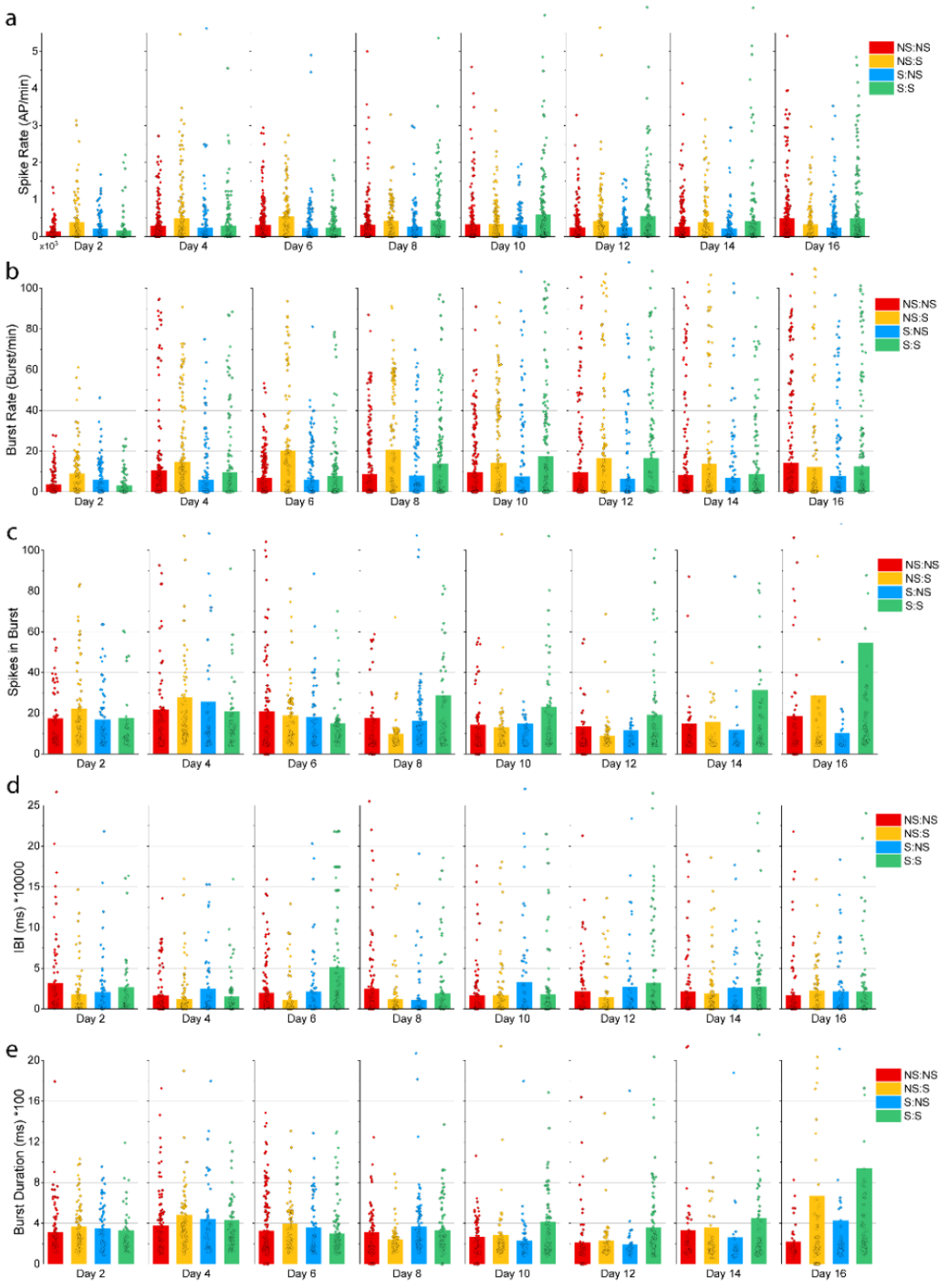

Figure 2-10. Burst parameters for all active electrodes at each recording day for the spontaneous activity: a spike rate b burst rate c number of spikes in burst d intraburst interval e burst duration and f percentage of spikes found in bursts.

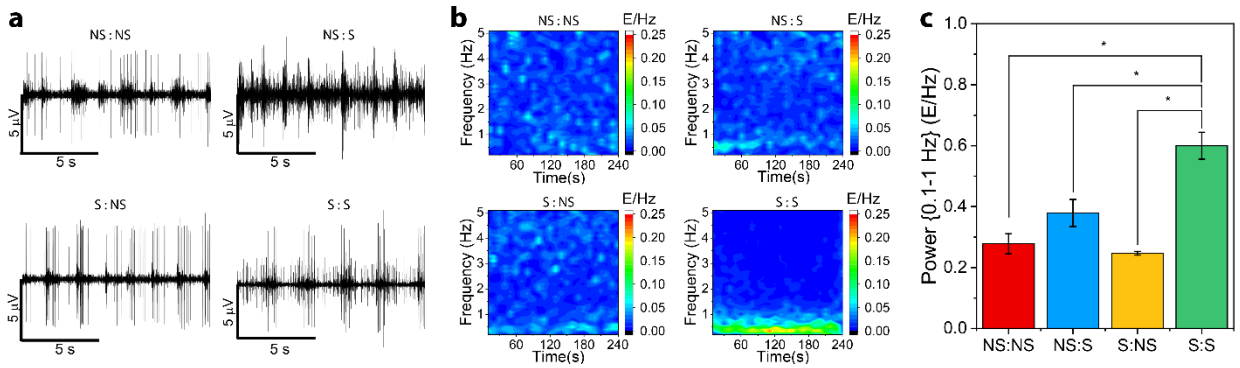

Figure 2-11. Stimulating training regimens modulates firing patterns in the frequency domain. a. Fifteen second representation of spontaneous voltage recording from NS:NS, NS:S, S:NS and S:S samples for D 25. b. Smoothened (3 point moving average) and normalized (AUC) power spectra was calculated for contiguous 10 s windows across the 4 mins of spontaneous recording NS:NS, NS:S, S:NS and S:S. Resulting matrices were averaged across samples. c. Bar graph for the sum of power spectral density magnitude from (b) across the spontaneous recording time between 0.1 Hz and 1 Hz. (n = 3, mean ± SEM). (*p<0.05; ANOVA with post-hoc Tukey)

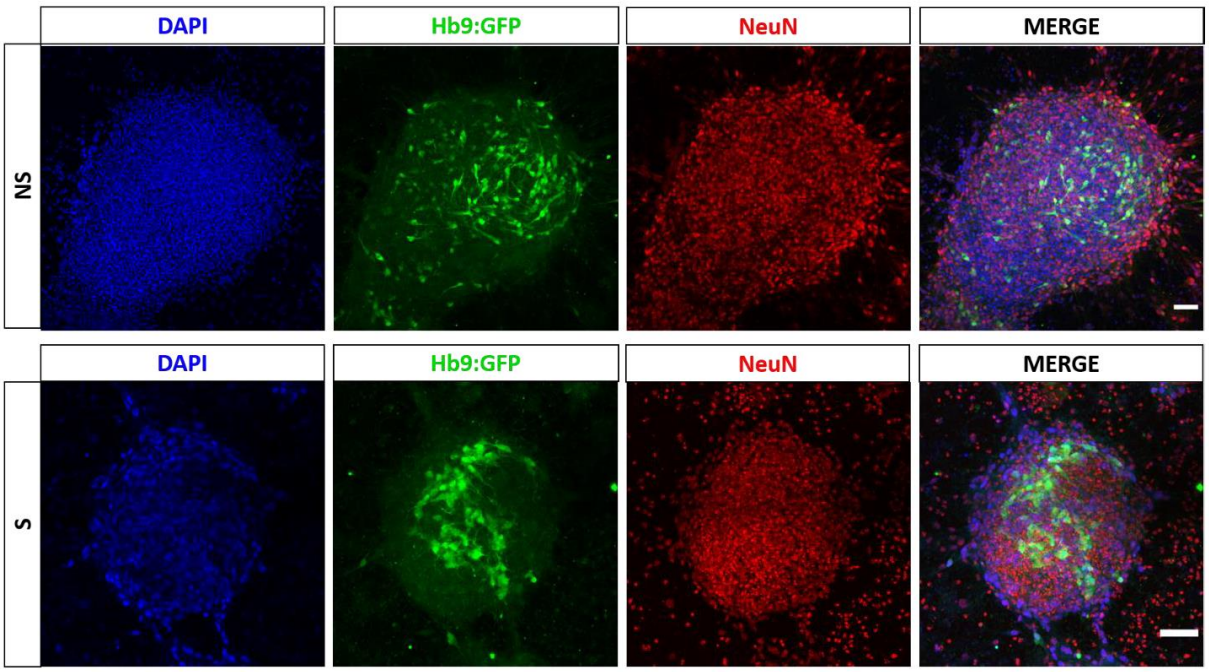

Figure 2-12 Confocal images of stains for motor neuron expression for non-stimulated (a) and stimulated (b) MEB at D9. (Scale bar: 50 µm)

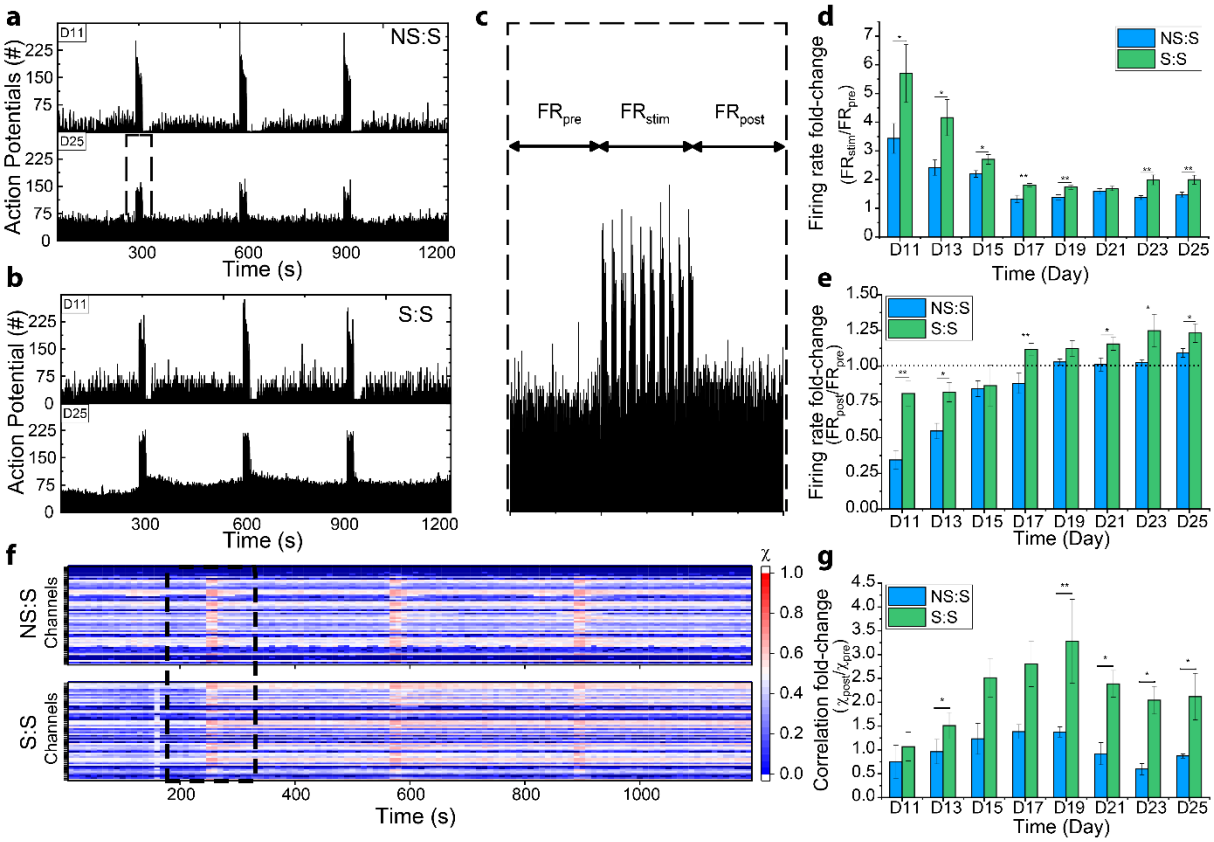

Figure 2-13. Stimulation during neurogenesis alters response to stimulation during network formation. Spike counts per each hundredth of a second across the 20 mins of recording was graphed for D11 and D25 for samples NS:S (a) and S:S (b). c. Zoom-in of A for 1min, centered around the 20 seconds of stimulation at D25 for sample NS:S, the arrows represent the firing rate prior to stimulation (FR_{pre}), the firing rate during stimulation (FR_{stim}) and the firing rate after stimulation (FR_{post}). d. Bar graph showing the firing rate increase between Fr_{stim}/Fr_{pre} for D11-D25. (n = 9, mean ± SEM). e. Bar graph showing the firing rate increase between Fr_{post}/Fr_{pre} for D11-D25. (n = 9, mean ± SEM). f. Raster plot of average correlation value for each electrode during 10 s bins across the entire recording time. g. Ratio of average correlation value prior to stimulation during recording and correlation value post stimulation (χ_{post}/χ_{pre}). (n = 3, mean ± SEM) (*$p<0.05$, **$p<0.005$; one-tailed T-test)

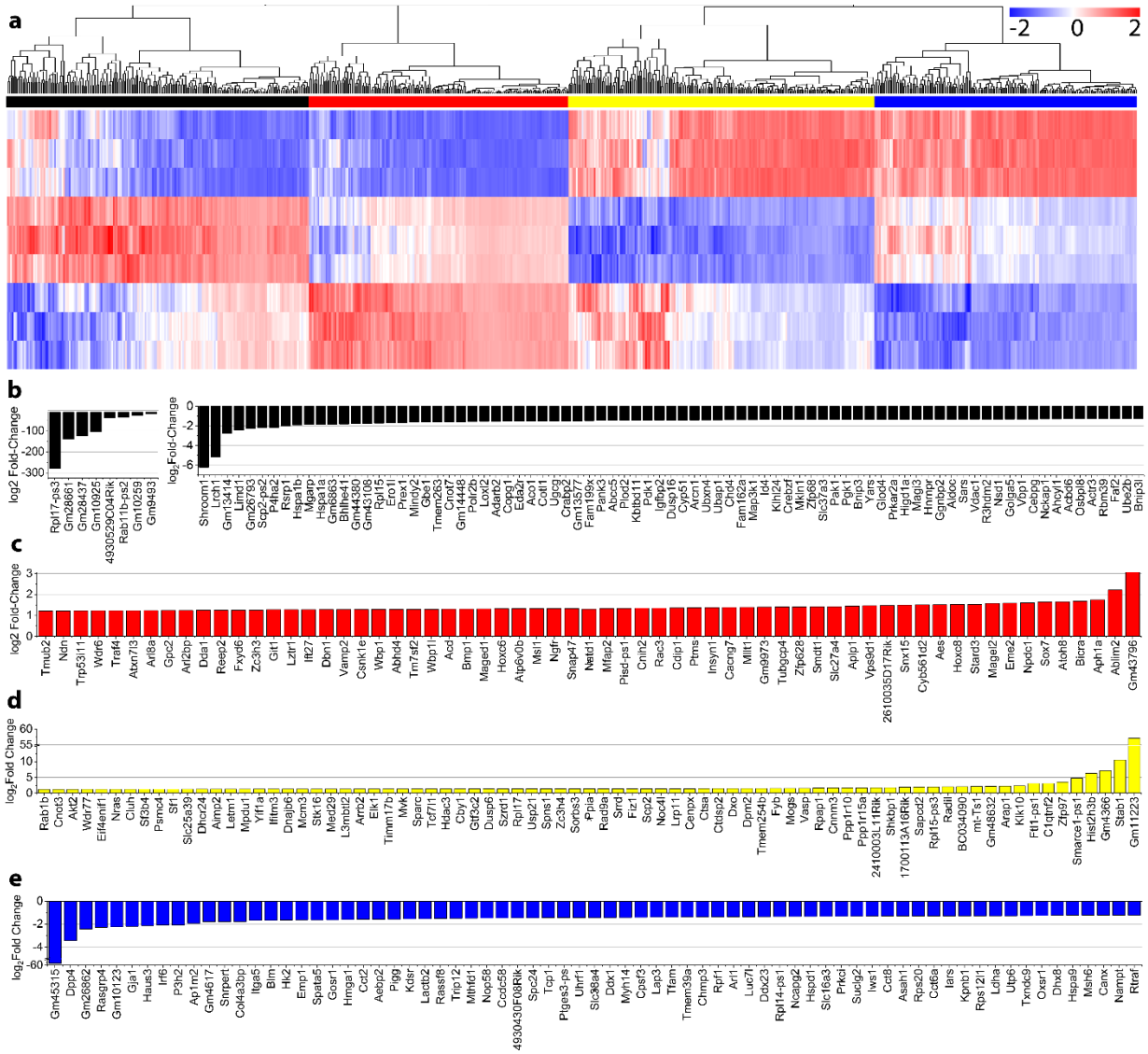

Figure 2-14. RNA Sequencing shows differential expression as a result of optical stimulation during neurogenesis. a. Heat map of standard deviation of differential expression for genes with $p<0.05$ (n=749). Genes were primarily clustered for: 1) genes that would overexpress during differentiation and underexpressed due to stimulation, 2) genes that would overexpress during control differentiation and overexpressed further due to stimulation, 3) genes that would underexpress during control differentiation and stimulation minimized that underexpression and 4) genes that would underexpress during control differentiation and stimulation amplified that underexpression. (first color column in order: black, red, yellow, blue). Significantly differentially regulated genes, with $p<0.0005$ (n=307) were extracted as column plots for: b. black, c. red, d. yellow and e. blue clusters.

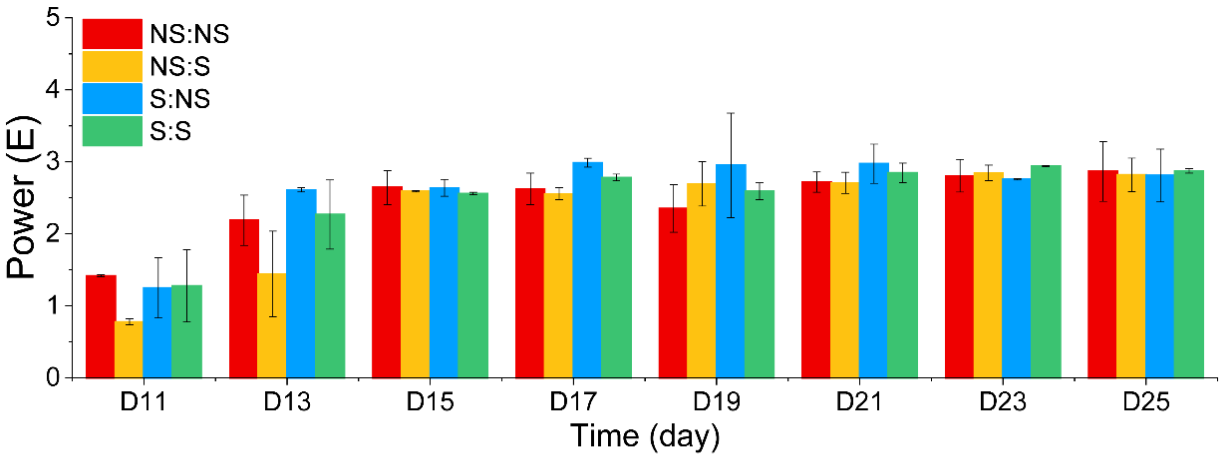

Figure 2-15 Sum of total power spectra between 0-5 Hz between all four experimental groups for all recording done during spontaneous activity. (n = 3, mean ± SEM).

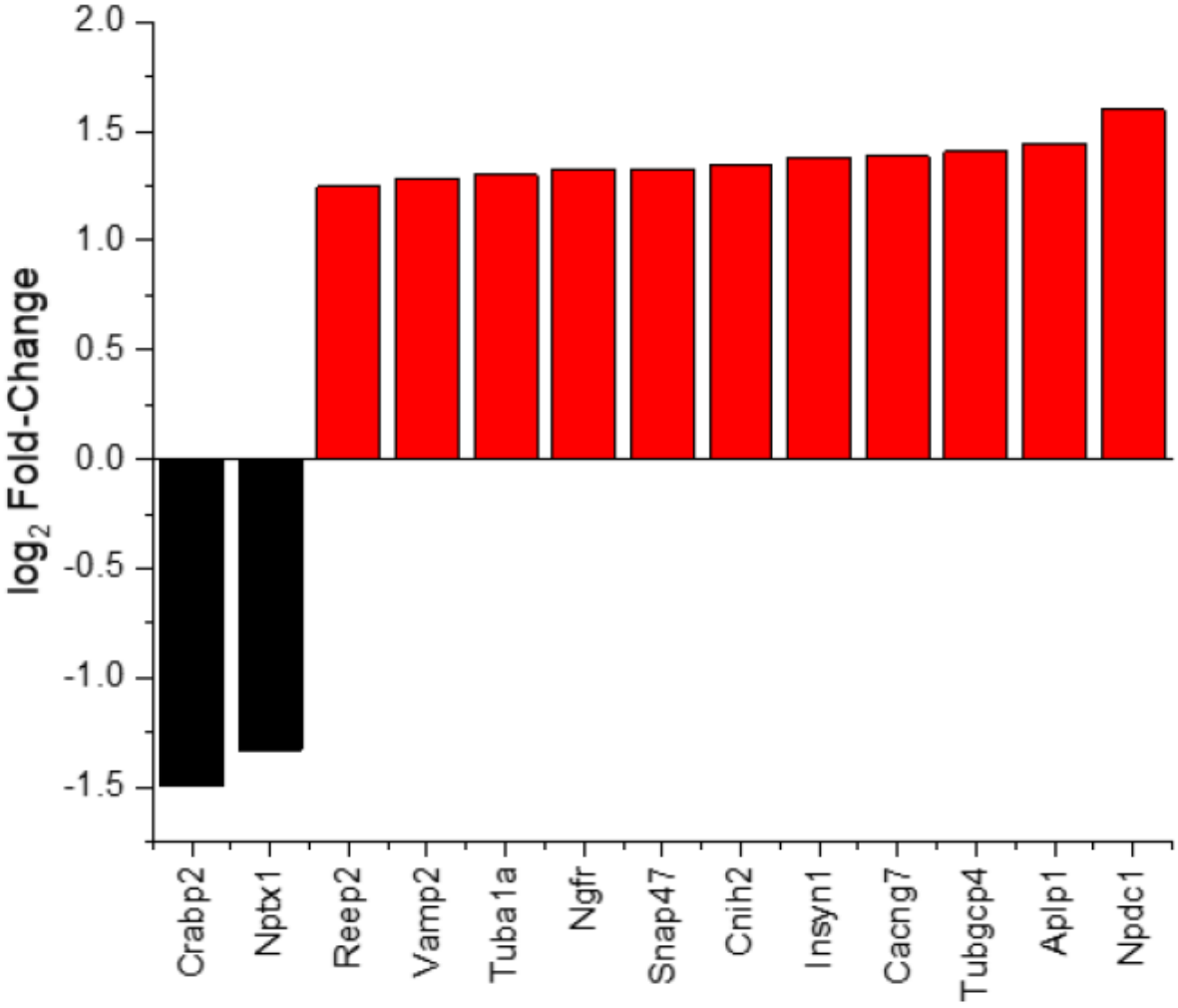

Figure 2-16. Bar graphs showing the differentially expressed genes that satisfied the significance threshold ($p<0.0005$) and have been reported to be related to neural development and function

Table 2-1. Expression comparisons for phenotypic gene targets

Gene	Description	log.FC D2 v NS	FDR p	log.FC NS v S	FDR p
	ESC - Pluripotency				
OCT ¾ - (POU5F1)	POU domain, class 5, transcription factor 1	-1335.2	1.32E-08	-1.01074	0.993303
NANOG	Nanog homeobox transcription factor SRY	-195.156	1.54E-08	1.291579	0.610174
SOX2	(sex determining region Y)-box 2	-1.1334	0.152156	-1.15112	0.32166
	Neuronal Population				
Neurod6	neurogenic differentiation 2	78.42929	2.04E-09	1.298647	0.378425
Fox-3	RNA binding protein, fox-1 homolog	77.39941	3.59E-10	-1.17408	0.501273
NEF	3 Neurofilament	92.5854	5.86E-13	-1.02714	0.762375
	Astrocytes				
Aqp4	Aquaporin 4	N/A	N/A	N/A	N/A
Gfap	glial fibrillary acidic protein	27.17674	1.39E-07	-1.14314	0.766754
Fgfr-3	fibroblast growth factor receptor 3	59.96818	2.87E-10	1.029678	0.917007
	Oligodendrocytes				
Mbp	myelin basic protein oligodendrocyte	10.7271	8.42E-09	-1.00645	0.984504
Olig2	transcription factor 2 myelin	-1.24175	0.006191	-1.21048	0.094616
Mog	oligodendrocyte glycoprotein	7.42182	5.11E-07	1.168882	0.60045
	Motor Neurons				
ChAT	choline acetyltransferase	46.15114	2.36E-06	1.55963	0.508302
MNX1	motor neuron and pancreas homeobox 1	21.12197	5.35E-11	1.15419	0.234447
PAX6	paired box 6	16.48545	2.91E-09	1.164541	0.454262
	Glutamatergic Neurons				
Slc17a6	solute carrier family 17 (sodium-dependent inorganic phosphate cotransporter), member 6	7.715048	4.04E-08	-1.07919	0.747595

Table 2-2. Significantly ($p<0.0005$) differentially expressed genes reported in literature as regulators of neural development

Gene	Description	Function	References
Npdc1	neural proliferation, differentiation and control 1	Responsible for regulating differentiation. Upregulated in adult brains compared to young brains	Qu, X. *et al.* [39], Evrard, C. *et al.*[40], Galiana, E. *et al.*[41], Sansal, I. *et al.*[42]
Crabp2	cellular retinoic acid binding protein II	Upregulated in differentiated Motor Neurons, and downregulated in mature motor neurons	Boucherie, C. *et al.,* Chaerkady, R. *et al.,* Zhang, Q. *et al.*
Snap47	synaptosomal-associated protein, 47	Involved in unique fusion machinery for postsynaptic and presynaptic function	Münster-Wandowski, A. *et al.* Holt, M. *et al.* Arora, S. *et al.*
Tubgcp4	tubulin, gamma complex associated protein 4	Important in the nucleation and polar orientation of microtubules	Scheidecker, S. *et al.* Sánchez-Huertas, C. *et al.*
Aplp1	amyloid beta (A4) precursor-like protein 1	Supports maintenance of dendritic spines and basal synaptic transmission. High impact on synapse formation and synaptic plasticity. Is upregulated during synaptogenesis and is essential for proper synapse formation.	Mayer, M. C. *et al.* [43], Schilling, S. *et al.*[44], Weyer, S. W. *et al.* [45], Klevanski, M. *et al.*[46], Kim, T.-W. *et al.*[47]
Cacng7	calcium channel, voltage-dependent, gamma subunit 7	Critical to Neural communication for Ca-dependent fusion of two secretory organelles: synaptic vesicles (SV) and neuropeptide-filled dense-core vesicles (DCV). Regulates the trafficking and gating properties of AMPA-selective glutamate receptors (AMPARs).	Yang, L. *et al.*, Kato, A. S. *et al.*
Cnih2	cornichon family AMPA receptor auxiliary protein 2	Influences the efficacy of excitatory synaptic transmission. Slows synaptic transmission for reliable and successful transmission of a sugnal accros the synapse	Boudkkazi, S. *et al.*, Boudkkazi, S. *et al.*, Shi, Y. *et al.* Gu, X. *et al.*
Insyn1	inhibitory synaptic factor 1	Regulates postsynaptic inhibition and contributes to brain development	Gamlin, C. R. *et al.*, Uezu, A. *et al.*
Vamp2	vesicle-associated membrane protein 2	Involved in the dockin and/or fusion of synaptic vesicles with the presynaptic membrane. It forms a distinct complex with synaptophysin.	Russell, C. L. *et al.* Schwarz, T. L. Winkle, C. C. & Gupton, S. L. Winkle, C. C. & Gupton, S. L. Koo, S. J. *et al.*
Reep2	receptor accessory protein 2	Expressed in neuronal exocytotic tissue	Sjöstedt, E. *et al.* Esteves, T. *et al.* Hübner, C. A. & Kurth, I. Hurt, C. M. *et al.*
Ngfr	nerve growth factor receptor (TNFR superfamily, member 16)	Receptor for member of signaling pathway activating neurothrophins, p75NTR	Huang, E. J. & Reichardt, L. F. Barrett, G. L. & Bartlett, P. F.
Nptx1	neuronal pentraxin 1	Key factor in synapse loss and neurite damage	Omeis, I. A. *et al.*, Abad, M. A. *et al.*, Dodds, D. C. *et al.*,

2.6 REFRENCES

1. J. P. Weick, *et al.*, Functional Control of Transplantable Human ESC-Derived Neurons Via Optogenetic Targeting. *STEM CELLS* **28**, 2008–2016 (2010).

2. M. M. Daadi, *et al.*, Optogenetic Stimulation of Neural Grafts Enhances Neurotransmission and Downregulates the Inflammatory Response in Experimental Stroke Model. *Cell Transplant.* **25**, 1371–1380 (2016).

3. J. B. Bryson, *et al.*, Optical control of muscle function by transplantation of stem cell-derived motor neurons in mice. *Science* **344**, 94–97 (2014).

4. J. C. Piña-Crespo, *et al.*, High-Frequency Hippocampal Oscillations Activated by Optogenetic Stimulation of Transplanted Human ESC-Derived Neurons. *J. Neurosci.* **32**, 15837–15842 (2012).

5. J. Tessadori, M. Bisio, S. Martinoia, M. Chiappalone, Modular Neuronal Assemblies Embodied in a Closed-Loop Environment: Toward Future Integration of Brains and Machines. *Front. Neural Circuits* **6** (2012).

6. T. B. DeMarse, D. A. Wagenaar, A. W. Blau, S. M. Potter, The neurally controlled animat: biological brains acting with simulated bodies. *Auton. Robots* **11**, 305–310 (2001).

7. A. Novellino, *et al.*, Connecting Neurons to a Mobile Robot: An In Vitro Bidirectional Neural Interface. *Comput. Intell. Neurosci.* **2007**, 1–13 (2007).

8. P. Massobrio, J. Tessadori, M. Chiappalone, M. Ghirardi, In Vitro Studies of Neuronal Networks and Synaptic Plasticity in Invertebrates and in Mammals Using Multielectrode Arrays. *Neural Plast.* (2015) https:/doi.org/10.1155/2015/196195 (February 22, 2018).

9. Y. Jimbo, T. Tateno, H. P. Robinson, Simultaneous induction of pathway-specific potentiation and depression in networks of cortical neurons. *Biophys. J.* **76**, 670–678 (1999).

10. C. P. Marder, D. V. Buonomano, Timing and balance of inhibition enhance the effect of long-term potentiation on cell firing. *J. Neurosci. Off. J. Soc. Neurosci.* **24**, 8873–8884 (2004).

11. P. Caroni, F. Donato, D. Muller, Structural plasticity upon learning: regulation and functions. *Nat. Rev. Neurosci.* **13**, 478–490 (2012).

12. J. le Feber, J. Stegenga, W. L. C. Rutten, The Effect of Slow Electrical Stimuli to Achieve Learning in Cultured Networks of Rat Cortical Neurons. *PLoS ONE* **5**, e8871 (2010).

13. S. Marom, G. Shahaf, Development, learning and memory in large random networks of cortical neurons: lessons beyond anatomy. *Q. Rev. Biophys.* **35** (2002).

14. B. C. Wheeler, G. J. Brewer, Designing Neural Networks in Culture. *Proc. IEEE* **98**, 398–406 (2010).

15. H. A. Johnson, A. Goel, D. V. Buonomano, Neural dynamics of *in vitro* cortical networks reflects experienced temporal patterns. *Nat. Neurosci.* **13**, 917–919 (2010).

16. D. A. Wagenaar, J. Pine, S. M. Potter, Searching for plasticity in dissociated cortical cultures on multi-electrode arrays. *J. Negat. Results Biomed.* **5**, 16 (2006).

17. A. N. Ide, A. Andruska, M. Boehler, B. C. Wheeler, G. J. Brewer, Chronic Network Stimulation Enhances Evoked Action Potentials. *J. Neural Eng.* **7**, 16008 (2010).

18. E. Maeda, Y. Kuroda, H. P. Robinson, A. Kawana, Modification of parallel activity elicited by propagating bursts in developing networks of rat cortical neurones. *Eur. J. Neurosci.* **10**, 488–496 (1998).

19. S. Joo, S. Y. Song, Y. S. Nam, Y. Nam, Stimuli-Responsive Neuronal Networking via Removable Alginate Masks. *Adv. Biosyst.* **2**, 1800030 (2018).

20. M. Mitchell, *Complexity: A Guided Tour* (Oxford University Press, 2009).

21. , Recording action potentials from cultured neurons with extracellular microcircuit electrodes. *J. Neurosci. Methods* **2**, 19–31 (1980).

22. I. C. Gomes, M. Acquarone, R. de M. Maciel, R. B. Erlich, S. K. Rehen, Analysis of Pluripotent Stem Cells by using Cryosections of Embryoid Bodies. *J. Vis. Exp. JoVE* (2010) https:/doi.org/10.3791/2344 (August 30, 2018).

23. L. R. Rabiner, B. Gold, *Theory and application of digital signal processing* (Englewood Cliffs, N.J. : Prentice-Hall, 1975) (November 11, 2019).

24. A. M. Bolger, M. Lohse, B. Usadel, Trimmomatic: a flexible trimmer for Illumina sequence data. *Bioinforma. Oxf. Engl.* **30**, 2114–2120 (2014).

25. R. Patro, G. Duggal, M. I. Love, R. A. Irizarry, C. Kingsford, Salmon provides fast and bias-aware quantification of transcript expression. *Nat. Methods* **14**, 417–419 (2017).

26. C. Soneson, M. I. Love, M. D. Robinson, Differential analyses for RNA-seq: transcript-level estimates improve gene-level inferences. *F1000Research* **4**, 1521 (2015).

27. M. D. Robinson, A. Oshlack, A scaling normalization method for differential expression analysis of RNA-seq data. *Genome Biol.* **11**, R25 (2010).

28. Y. Chen, A. T. L. Lun, G. K. Smyth, From reads to genes to pathways: differential expression analysis of RNA-Seq experiments using Rsubread and the edgeR quasi-likelihood pipeline. *F1000Research* **5**, 1438 (2016).

29. Y. Benjamini, Y. Hochberg, Controlling the False Discovery Rate: A Practical and Powerful Approach to Multiple Testing. *J. R. Stat. Soc. Ser. B Methodol.* **57**, 289–300 (1995).

30. S. Park, *et al.*, Optogenetic control of nerve growth. *Sci. Rep.* **5** (2015).

31. S. G. M. Uzel, *et al.*, Microfluidic device for the formation of optically excitable, three-dimensional, compartmentalized motor units. *Sci. Adv.* **2** (2016).

32. H. Wichterle, M. Peljto, "Differentiation of Mouse Embryonic Stem Cells to Spinal Motor Neurons" in *Current Protocols in Stem Cell Biology*, M. Bhatia, *et al.*, Eds. (John Wiley & Sons, Inc., 2008) https:/doi.org/10.1002/9780470151808.sc01h01s5 (March 8, 2017).

33. C. Cvetkovic, M. H. Rich, R. Raman, H. Kong, R. Bashir, A 3D-printed platform for modular neuromuscular motor units. *Microsyst. Nanoeng.* **3**, 17015 (2017).

34. S. Lobov, A. Simonov, I. Kastalskiy, V. Kazantsev, Network response synchronization enhanced by synaptic plasticity. *Eur. Phys. J. Spec. Top.* **225**, 29–39 (2016).

35. A. El Hady, *et al.*, Optogenetic stimulation effectively enhances intrinsically generated network synchrony. *Front. Neural Circuits* **7** (2013).

36. Y. Jimbo, H. P. C. Robinson, A. Kawana, Strengthening of synchronized activity by tetanic stimulation in cortical cultures: application of planar electrode arrays. *IEEE Trans. Biomed. Eng.* **45**, 1297–1304 (1998).

37. D. A. Wagenaar, R. Madhavan, J. Pine, S. M. Potter, Controlling Bursting in Cortical Cultures with Closed-Loop Multi-Electrode Stimulation. *J. Neurosci. Off. J. Soc. Neurosci.* **25**, 680–688 (2005).

38. R. Madhavan, Z. C. Chao, S. M. Potter, Plasticity of recurring spatiotemporal activity patterns in cortical networks. *Phys. Biol.* **4**, 181–193 (2007).

39. W. T. Dauer, Neurogenetic Disease: Genes, Mechanisms, and Future Promise. *Neurotherapeutics* **11**, 697–698 (2014).

40. S. Marom, *Science, Psychoanalysis, and the Brain: Space For Dialogue* (Cambridge University Press, 2015) https:/doi.org/10.1017/CBO9781316181706 (November 11, 2019).

41. T. Abrahamsson, B. Gustafsson, E. Hanse, Synaptic fatigue at the naive perforant path-dentate granule cell synapse in the rat. *J. Physiol.* **569**, 737–750 (2005).

CHAPTER 3: ENGINEERING GEOMETRICAL 3-DIMENSIONAL UNTETHERED IN-VITRO NEURAL TISSUE MIMIC[1]

3.1 INTRODUCTION

The design of living tissue to create specific shapes and forms is arguably one of the main obstacles in the forward-design of engineered tissues, cellular systems, and biological machines. Given the fact that three-dimensional structures are critical to recapitulate many physiologically relevant characteristics, a major goal of tissue engineering is to achieve customizable and viable 3D cell cultures. To an extent, this has been achieved by engrafting cells of interest on synthetic structures (1), or more recently providing cells with protein matrices such as Matrigel and fibrin which facilitate cell-cell and cell-extracellular matrix (ECM) interactions (2–5). This approach creates a liquid state of protein-rich solutions mixed with cells. After subsequent polymerization, 3D structures are formed and the cells are allowed to grow and function (Figure 3-1a).

Such an approach has been used to differentiate progenitor cells towards developing functional organoids that mimic physiological morphologies and functions. For example, muscle cells have been differentiated into actuating tissue for development of biohybrid actuators for soft robotics (6, 7), to develop models for drug discovery or therapeutic studies (2, 8), as well as studies on healing in 3D and tissue regeneration (9, 10). An interesting observation has been that by providing a mold during the culture, the cell-matrix solution can be compacted into stable

[1] This section is a reproduction of the following first authored journal article:
Gelson J. Pagan-Diaz, Karla P. Ramos-Cruz, Richard Sam, Mikhail E. Kandel, Onur Aydin, M. Taher A. Saif, Gabriel Popescu, Rashid Bashir. Engineering geometrical 3-dimensional untethered in vitro neural tissue mimic. Proceedings of the National Academy of Sciences Dec 2019, 116 (51) 25932-25940; DOI: 10.1073/pnas.1916138116.

Author Contributions: G.J.P.-D. and R.B. designed research; G.J.P.-D., K.P.R.-C., R.S., M.E.K., O.A., M.T.A.S., and G.P. performed research; M.E.K. and G.P. contributed new reagents/analytic tools; G.J.P.-D., M.E.K., and G.P. analyzed data; and G.J.P.-D. and R.B. wrote the paper.

geometries due to internal stresses generated by traction forces generated by the engrafted cells (11). In other words, the shape of the resulting construct can be determined by the 3D printed molds, which are fabricated using bio-printing approaches, such as a stereolithography apparatus (SLA) 3D printer (Figure 3-1b). Given the needs and interests in 3D neuroengineering, using this approach of cell-matrix compaction for the formation of controlled 3D neural architectures could be highly beneficial.

Currently, 3D neural tissue is often obtained from animal models or from spherical embryoid bodies spontaneously formed during stem cell differentiation (12–14). These embryoid bodies are currently unable to be scaled up due to diffusion limitations, placing limitations on their compatibility with specific experimental platforms. For example, fabrication of such untethered and mechanically strong neural tissue mimics could help in the assessment of new electrodes for neural functionality, neurotransmission and the assess biocompatibility and neural damage during implantation (15–17). On the other hand, efforts to develop free-standing 3D tissue models *in-vitro* that incorporate neuronal functionality, such as the formation of neuromuscular junctions in 3D muscle tissues, are limited when trying to adhere the neurons on the overall 3D constructs (12, 18). Having control of the size and geometry of a neural tissue mimic that can be handled and installed after neural development can facilitate the assembly of neuro-driven biological machines (19). Furthermore, continued advancements towards engineered *in-vitro* neural tissues of various shapes and sizes to develop better models are important to minimize the use of animal models (20)(Figure 3-1c).

In this work, we utilized fibrin as a scaffold to engraft differentiated ESC-derived neurons prior to their maturation in order to achieve untethered and geometrically stable neural tissue mimics (NTMs) that could be molded into desired shapes. We demonstrated and characterized

three shapes: a rod, a cube, and a toroid (Figure 3-1b, Figure 3-2). By using mouse embryonic stem cells, we compared seeding cell densities to determine a protocol for tissue formation of various shapes. We also characterized development and functionality, first using mouse-derived embryonic stem cells (mESC) due to their shorter differentiation times and reduced costs as compared to human stem cells. We then implemented the protocol with human stem cells to demonstrate the possibility for clinical and biomedical applications.

3.2 MATERIALS AND METHODS

3.2.1 MOUSE EMBRYONIC STEM CELLS (MESC) CULTURE AND DIFFERENTIATION

Myocin-C inactivated mouse embryonic fibroblast (MEF) were used as a feeder layer for mESC expansion. They were seeded at a cell density of ~3.5e4 cells/cm2 and cultured in DMEM (Dulbecco's modified Eagle's medium) supplemented with 1% fetal bovine serum, 1% L-glutamine and 1% penicillin-streptavidin in T-25 flasks. After 2 days of recovery, HB9::GFP transgenic mouse embryonic stem (mES) cells transfected with (Channelrhodopsin) ChR2-TdTomato were seeded at $4*10^4$ cells/cm^2 in mESC proliferation media consisting of: low glucose DMEM with 15% (v/v) FBS, 1% (v/v) each of penincillin-streptomycin, L-glutamine, EmbryoMax nucleosides and MEM non-essential amino acids and freshly supplemented with 0.1 mM β-mercaptoethanol (LifeTechnologies) and 0.1% (v/v) mLIF (MilliporeSigma) before every daily media change.

Differentiation was begun when mESC colonies were >70% confluency. At the appropriate time, we added neural differentiation media (nDM) consisting of 44% (v/v) advanced DMEM/F12 , 44% (v/v) Neurobasal, 10% (v/v) KnockOut serum replacement (LifeTechnologies) and 1% (v/v) penicillin–streptomycin , 1% (v/v) L-glutamine(Cellgro

Mediatech, Inc.), and freshly supplemented with 0.1 mM β-mercaptoethanol. Cultures were incubated for 1-2 hrs before TrypLE was added to each flask. After detachment, the cells were centrifuged, resuspended in nDM and seeded at a density of 2e6 cells/dish in 100 mm low adhesion dishes with 10 mL nDM supplemented with Noggin (50ng/mL), bFGF (20ng/mL) and FGF-8 (20ng/mL) (Invitrogen). The next day, floating cells were collected to remove adhered non-neuronal lineages from the culture. On the following day, neural embryoid bodies (EBs) were replated in nDM supplemented with 1μM of retinoic acid (RA) (MilliporeSigma) and 1μM smoothened agonist (SAG) (EMD Chemicals). Media was then changed daily, taking care to not disrupt the forming EBs.

3.2.2 HUMAN EMBRYONIC STEM CELL (HESC-H9) CULTURE AND DIFFERENTIATION

Differentiation of human embryonic stem cells (H9) (WiCell, WA09) into neurons was achieved by following established protocols. Briefly, H9 were dissociated, using Accutase, and seeded on Matrigel (Corning)-coated plates using mTeSR1 (Stem Cells Technology) and 10mM ROCK inhibitor (Stem Cells Technology). After 24 hours of seeding we started differentiation into Neural Epithelial Progenitors (NEP) by replacing the H9 media with neuronal medium which was composed of DMEM/F12 (Stem Cells Technology), Brainphys medium (Stem Cells Technology) at 1:1, 1 × N2 (Stem Cells Technology), 2 × NeuroCult™ SM1 Neuronal Supplement (Stem Cells Technology), 50 μg/mL ascorbic acid (Stem Cells Technology), and 1 × penicillin/streptomycin (Sigma). In order to promote neurogenesis, the neuronal medium was supplemented with 3 μM CHIR99021 (CHIR) (Stem Cells Technology), 2 μM DMH1 (Stem Cells Technology) and 2 μM SB431542 (SB) (Stem Cells Technology), and changed every other

day for 6 days. Then, neuronal medium was supplemented with 1 μM CHIR, 2 μM SB, 2 μM DMH1, 0.1 μM Retinoic Acid (RA) (Sigma) and 0.5 μM Purmorphamine (Pur) (Stem Cells Technology), and changed every other day for 6 days. Afterwards, neural progenitor cells were split 1:6 and plated in PLO (Sigma) /Laminin (Sigma) coated plate. To start differentiation into neurons, neuronal medium was supplemented with 0.5 μM RA and 0.1 μM Pur for 6 days. Then, for neuronal maturation, after formation of nerve tissue, we also added 0.1 μM Compound E, 1mM Dibutyryl-cAMP (Stem Cells Technology), 10 mg mL brain-derived neurotrophic factor (Stem Cells Technology) and 10 mg mL ciliary neurotrophic factor (Stem Cells Technology).

3.2.3 NEURAL TISSUE MIMIC FORMATION

On day 5 of differentiation, mouse-derived motor-neuronal embryoid bodies (MEBs) were dissociated in TypLE for 3mins, pipetting every minute. It was observed that dissociation had to occur prior to or at the very early stages of maturation of embryoid bodies (EBs), otherwise tissues would not compact due to excessive cell death.(8, 21) This is likely because of an elevated amount of innervation across the EB, which would be ruptured during dissociation(22).At the reported seeding densities, we observed that 0.5mL of TypLE per dish of EBs worked optimally, as too harsh trypsinization seemed to impede tissue compaction upon engrafting in fibrin hydrogels. Dissociated cells were then counted and aliquoted at the desired cell densities. They were then mixed with 30% Matrigel (Corning), 4 $mg/mL_{fibrinogen}$ (Sigma-Aldrich), and 2 U per $mg_{Fibrinogen}$ of thrombin (Sigma-Aldrich), for a total of 100 μL of solution per batch. Each cell-fibrin solution was dispensed in 25 μL aliquots to a PEGDA mold. (23–25) The fibrin hydrogel was permitted to cross-link for 2hrs before adding nDM supplemented with supplemented with 10 ng/mL each of GDNF and CNTF (Neuromics). Media was changed daily,

and tissues were permitted to compact for 4 days before releasing from molds. Human-derived tissues were formed analogously to mouse-derived tissues, doing the dissociation step at day 18 of differentiation.

3.2.4 DESIGN AND 3D PRINTING OF MOLD

Tissue molds were 3D printed using a SLA Asiga Pico 2 (Asiga). We used 18% (v/v) PEGDA M_W 700g/mol (SA) with 0.1% w/v LAP (Asiga) as a photoinitiator and 0.15% (v/v) Sudan I dye (Asiga) to minimize photo-scattering effects which affected geometric resolution. Washes with DI water between key layers was done to achieve concave structures. To remove dye prior to culturing, fabricated parts were bleached with 10% bleach for 2hrs, followed by 1hr wash in 70% EtOH and then washed with phosphate-buffered saline (PBS). If needed, molds were further sterilized with 30min exposure of UV light. Because of the low stiffness of the cell-hydrogel matrix, fabricating bridges was deemed necessary for the initial stage of compaction to ensure the tissue would stay inside, and later broken off in order to get access to the tissue.

3.2.5 MEA ELECTROPHYSIOLOGY

Microelectrode array chips were prepared for seeding by an initial precoating of poly-D-lysine (MilliporeSigma, MO) at 100 µg/mL in DI Water overnight. The chips were then washed and allowed to dry. Laminin (50 µg/mL) slowly thawed at 4^{o}C was added and the chip incubated for 20 minutes at 37^{o}C. Extra laminin was aspirated, and tissues were seeded before the chip dried. Tissues were then permitted to adhere for 1.5 hours before adding fully supplemented media. Recordings were performed on seeded 60-electrode chip using a MEA 2100-Lite Amplifier (Multi Channel Systems MCS GmbH, Germany) maintained at 37^{o}C using a TC02

temperature controller (Multichannel Systems). Recording was done at a gain of 1100 and a bandwidth of 1 to 10kHz. Data was acquired at a sampling frequency of 10kHz as well using a rack set in MultiChannel Experimenter. Recordings were analyzed post hoc after baseline fluctuations were removed with a high-pass filter (2^{nd} order Butterworth filter) with a highpass cut-off frequency of 200Hz, using MultiChannel Analyzer (Multichannel Systems). Temporal analysis of spike and burst events (instruments: Spike Analyzer and Burst Analyzer) was performed with the same software after a threshold of 5 standard-deviations of the mean noise was used to detect action potential events. Discreet sequences of timestamps of action potential events per electrode were used to calculate the cross-correlation at zero lag and normalized to unity for autocorrelation using MATLAB. This value was used to quantify synchronicity. Raw spike trains were extracted through MultiChannel Manager (MultiChannel Systems) for visualization.

3.2.6 OPTOGENETIC STIMULATION AND PHARMACOLOGIC TESTING

Optogenetic stimulation for the mouse-derived tissue was performed on 2 tissues of each shape (n=2*3 shapes). We used a Laser Diode with an integrated Driver set at 450nm (Doric Lenses, Quebec, Canada) attached to a 50 µm core multimode NA 0.22 Fiberoptic Patchcord and a collimator with 6mm focal length fitted to the optical fiber with FC receptacle and fitted into 12.7 mm cylinder, 20 mm long to generate a 2.5mm diameter beam. Stimulation patterns were designed with Doric Neuroscience Studio. During recording, stimulation was done in 5ms pulses at 20Hz radiated in 2 s cycle periods at 50% duty cycle for 20 sec every minute during the 5 mins recording sessions, for a total of 4 stimulations (n=4).

Pharmacologic substances were used for the human-derived tissue after 21 days of culturing in MEAs (n=6). The medium for each MEA sample was replaced with 2 mL of fresh medium mixed with the selected substance. After 1 min of incubation, recordings were performed for 5 minutes and the sample was washed 3 times with fresh warm media every 30 sec and later incubated for 5 minutes, before adding the subsequent substance. The post-synaptic response was pharmacologically modified with 6 cultures in the following order: spontaneous activity was first measured in fresh media, before adding DL-2-amino-5-phosphonopentanoic acid; D-AP5, 20 μM (MilliporeSigma, MO) (an NMDA antagonist) followed by a washout and an additional measurement in fresh media. Later, gamma-aminobutyric acid; GABA, 100 μm (MilliporeSigma, MO) was added, and followed by 1(S),9(R)-(-)-bicuculline methiodide; bicuculline, 10 μM (MilliporeSigma, MO) (a $GABA_A$ antagonist).

3.2.7 CRYOSECTIONING AND PARAFFIN-EMBEDDED SECTIONING

For confocal imaging, tissues were fixed for 20 min in 4% paraformaldehyde. After washing with PBS, buffer was sequentially substituted with sucrose solutions (10% w/v, 20% w/v and 30% w/v). After an overnight wash at 30% w/v sucrose solution in 4oC, tissues were embedded in OCT solution (Tissue-Tek, CA) and frozen on dry ice prior to storing in -20oC. Molds were sectioned in 20μm thick layers unto SuperFrost Plus slides (ThermoFisher Scientific, MA) and air dried at room temperature for 1hr. Phosphate buffered saline (PBS) was used to wash the OCT and slides were dried at 37oC for ~1 hr to improve adhesion while avoiding to overdry. Samples were then bordered with water repellent barrier using a PAP Pen (Abcam) and then blocked using antibody diluent (AD) (LifeTechnologies) in 4oC at least 12hr.

For H&E staining, tissues were fixed in 10% formalin for 1 day, washed 3 times with 70% ethanol and stored at 4oC until ready for the manual processing, as these tissues were still too delicate for standard automated paraffin processing. Samples were embedded in paraffin following Schedule II of Table I of Jali et al, JOMPF, 2015.(26) Embedded samples were sectioned in 5µm thick slices using a microtome mounted on glass slides and dried overnight.

3.2.8 IMMUNOSTAINING AND HISTOLOGY

Immunocytochemistry was performed on sample cryoslices after blocking. All staining was done the same for the different resulting cocktails: primary antibodies were diluted in AD, added to samples and incubated for 24hr at 4^{o}C in a water vapor saturated enclosure. Afterwards, samples were washed in PBS for 5 min at room temperature three times and the cocktail with the corresponding cocktails of secondary antibodies were added and incubated for 2hr at room temperature. The used staining cocktails are summarized in the following table:

Table 3-1 Antibodies used for immunostaining

Cocktail	*1^{ry}AB*	*Company*	*Cat#*	*Host*	*Dilution Factor*	*2ndAB*
1	CNPase	Millipore	MAB326	M	1:1000	AF647
2	GFAP	Millipore	MAB360	M	1:1000	AF647
3	GAD65/67	Santa Cruz Biotechnology	SC7513	G	1:100	AF488
	VGlut	Synaptic Systems	135 304	GP	1:500	AF647
4	ChAT	Abcam	Ab18736	S	1:1000	AF488
	NeuN	Millipore	MAB377	M	1:500	AF647

Table 3-1 (Cont.) Antibodies used for immunostaining

5	Tenascin-C	Abcam	Ab108930	R	1:500	AF647
	NeuN	Millipore	MAB377	M	1:500	AF488
6	Laminin	Abcam	Ab11575	R	1:500	AF647
	NeuN	Millipore	MAB377	M	1:500	AF488
7	Collagen IV	Abcam	Ab6586	R	1:500	AF647
	NeuN	Millipore	MAB377	M	1:500	AF488
8	Fibronectin	Abcam	Ab2413	R	1:500	AF647
	NeuN	Millipore	MAB377	M	1:500	AF488
9	Fibrinogen	Abcam	Ab34269	R	1:500	AF647
	NeuN	Millipore	MAB377	M	1:500	AF488

Nuclei were stained with DAPI (1:5000) during the two hours of secondary staining. After washing overnight at 4^{o}C in PBS, samples were mounted with Prolong Diamond antifade (ThermoFisher, MA) under a sealed coverslip and imaged using Zeiss 710 Confocal microscope (Carl Zeiss Microscopy).

Mounted paraffin samples were stained with hematoxylin and eosin (H&E). After 24 h, they were imaged with Nanozoomer, a digital pathology system. For quantification of cell distribution, images were processed with ImageJ. A threshold was applied to each image to detect nuclei and the ImageJ Particle Analyzer feature was used to determine X–Y coordinates of each nucleus on every image. Simple MATLAB code was used to map the location of each nuclei in the image as well as calculating the minimum distance of each nucleus to the perimeter.

3.2.9 QUANTITATIVE PHASE IMAGING

To investigate the change in cellular dry mass we turn to quantitative phase imaging (QPI)(27), a label-free imaging modality that provides interferometric contrast via tissue refractive index. Gradient Light Interference Microscopy (GLIM) is a QPI technique, which has recently extended this capability to strongly scattering specimens(28, 29) (also, Kandel et al, Nat. Comm., in press). To image the large volumes in this work, we acquire time lapse quantitative phase gradient tomograms consisting of a 3 x 3 x 3 mm^3 volume by performing a z-scan at each tile in a 2 x 2 mosaic. The data is then integrated to obtain the quantitative phase map, yielding the distribution of cellular dry mass density. We then take the change in percentage total dry mass for each of the four mosaic volumes, to estimate the change in total dry mass. Interestingly, we observe statistically insignificant differences between categories hinting that the mechanism for different behavior changes is a reorganization of the tissue rather than a change in growth behavior.

3.2.10 RNA EXTRACTION AND REAL-TIME QPCR

Samples of MEBs were carefully collected and centrifuged at 14000 rpm for 15 mins, while single tissue samples were divided in individual Eppendorf tubes. After aspirating supernatant, samples were flash frozen using liquid nitrogen and immediately stored at -80°C, until mRNA extraction. Total RNA was collected and purified using the RNeasy Mini Kit Part 1 (Qiagen). The total RNA concentration was quantified using a Nanodrop spectrophotometer. Only samples with absorption ratios ($A_{260/280}$) >2.0 were included in this study. Synthesis of cDNA was done with 100ng RNA per sample with SuperScript IV VILO EzDNase Kit (ThermoFisher Scientific). Triplicate assays were performed by QuantStudio 3 (ThermoFisher Scientific) in TaqMan

Universal Master Mix II (Applied Biosystem). The probes used for monitoring development of neuronal populations for this study were: Adenosine A2a (Excitatory neurons)[Assay ID: Mm00802075_m1], Tyrosine Hydroxylase (Dopaminergic Neurons))[Assay ID: Mm00447557_m1], Choline Acetyltransferase (Functional Motor Neurons))[Assay ID: Mm01221880_m1], Hb9 (Motor Neuron Transcription Factor))[Assay ID: Mm01222622_m1], NMDAR1 (Glutamanergic Neurons))[Assay ID: Mm00433790_m1], Paravalbumin (Interneurons))[Assay ID: Mm00443100_m1], GAD67 (GABAergic Neurons))[Assay ID: Mm04207432_g1], GFAP (Astrocytes))[Assay ID: Mm01253033_m1], CNPase (Myelinating Oligodendrocytes))[Assay ID: Mm01306641_m1]. Probes used to monitor expression levels of extra-cellular matrix were Collagen IV [Assay ID: Mm01210125_m1], Laminin)[Assay ID: Mm01222029_m1], Tenascin C)[Assay ID: Mm00495662_m1], Fibronectin)[Assay ID: Mm01256744_m1], and Fibrinogen)[Assay ID: Mm00513575_m1]. Glyceraldehyde3-phosphate dehydrogenase (GAPDH, assay ID: Mm99999915) was used as the endogenous reference gene. RT-PCR was run at 50 °C for 2min, 95 °C for 2min, and 40 cycles [Denaturing: 95 °C for 1 s, Extend/Annealing: 60 °C for 20 sec] with ROX, FAM and MGB as reference dye, reporter and quencher, respectively.

3.2.11 DATA ANALYSIS AND STATISTICS

All data was represented with box plots or bar graphs. Boxes showed the 25-75 percentile, whiskers represented ±1 standard deviation (SD), while bar graphs represented mean ± SD. OriginLab Software was used to perform all statistical calculation and plotting. Statistical difference was analyzed using Unpaired T-test for comparisons between tissue and MEB data,

while ANOVA with Tukey's Post-Hoc was used for the rest. The statistical significance level was set for p-values of <0.05.

3.2.12 ABSOLUTE AND RELATIVE QUANTIFICATION OF REAL-TIME PCR DATA

Serial dilutions for all 14 targets and our reference target GAPDH were done with triplicates of calibrator samples (MEBs at D0). Analysis of qPCR data was done following established protocols by Applied Biosystems by ThermoFisher Scientific. Standard curves were formed, and linear fits were used to determine the slope for each curve. Slope values were used to calculate the Efficiency (E) and Amplification Factor (AF) using the following equations:

$$E = 10^{(-1/slope)-1} * 100\%$$

$$AF = 10^{1/-slope}$$

Experimental C_T values were adjusted to account for efficiency variability using the equation:

$$C_{T_{adj}} = \log_2 AF^{C_{T_{exp}}}$$

Comparative C_T Method ($\Delta\Delta C_T$) was used to compare expression levels between the developing tissues and MEBs at days D4 and D7 with respect to MEBs at D0. The ΔC_T and $\Delta\Delta C_T$ values were calculated by:

$$\Delta C_T = C_T(target) - \overline{C_T(\text{reference})}$$

$$\Delta\Delta C_T = \Delta C_T(sample) - \Delta C_T(callibrator)$$

Finally, values were reported as $log(2^{-\Delta\Delta C_T})$, to account for biases caused by exponential functions.

To compare across population targets within same samples, adjusted C_T values were converted into "quantity" values by calculating $2^{-C_{T_{adj}}}$. The "quantity" ratio ($Q_{target}/\overline{Q_{reference}}$) were calculated for each replicate value.

3.3 RESULTS

3.3.1 SEEDING CELL DENSITY AFFECTS THE STRUCTURE OF THE NEURAL TISSUE MIMIC

Previous works have studied the effects of changing the stiffness of the fibrin matrix on the resulting viability of tethered NTMs by changing the concentration of fibrinogen with respect to the added thrombin (30–32). We build upon those studies but due to our desire to obtain mechanically stable and untethered functional 3D *in-vitro* constructs, we studied the effect of varying the seeding cell concentration. For the purpose of our study, the day in which seeding took place was labeled as D0 (Figure 3-3). Prior work on developing untethered muscle tissue has reported 5e6 myoblasts/mL as the optimal cell seeding concentration (7, 25). Due to the lower traction force per neurons as compared to myoblasts (32), we considered higher seeding cell concentrations.(33) The goal was to find a cell concentration that would result in a mechanically strong structure while being low enough to lower costs and have high sample throughput. For this purpose, we studied 5e6 cells/mL (1X), 12.5e6 cells/mL (2.5X), 25e6 cells/mL (5X) and 50e6 cells/mL (10X) and observed them for the first 4 days of compaction. (Figure 3-4) It was noticed that by D1 for all four concentrations, neurites were extending across the fibrin hydrogel. However, for higher concentrations (5X and 10X) dark clusters started to form by D4 (Figure 3-5a). This spontaneous re-aggregation towards neural clumps could lead to heterogeneity across the tissue mimic, and if the clusters become too large could also lead to necrosis due to diffusion limitation (34). To investigate the difference in NTM architecture, we

measured high-resolution confocal z-stacks of the resulting constructs at the four seeding densities stained for beta-tubulin III, a general neural microtubule marker (Figure 3-5b). These images showed that higher seeding cell densities caused the cells to re-cluster as EBs and extend processes in clumps rather than homogenous neurite extensions, as also seen clearly in the frequency domain (Figure 3-5c). Due to the desire to achieve an homogenous internal environment to avoid the risks of clustering and optimize the consistency across the construct, we further quantified these trends in heterogeneity. For this purpose, the randomness of the images were measured using the MATLAB function for entropy, e, defined as, $e = -\sum p(z_i) * log_2 p(z_i)$ where p contains the normalized histogram counts of the field of view, z_i (35) (Figure 3-5c). We observed that the randomness of the neurite structures was higher for lower concentrations and decreased significantly for 10X cell concentration. To further understand these observations, we performed continuous live quantitative phase imaging using Gradient Light Interference Microscopy (GLIM) which allows for a label free method to estimate the dry cell mass, i.e. the protein content of the cells (28). The rates were statistically insignificant across the groups (Figure 3-5d), hinting that the possible mechanisms for the difference are due to the reorganization of the NTM rather than the cellular growth itself.

3.3.2 SEEDING CELL DENSITY AFFECTS THE COMPACTION AND NEURITE EXTENSION OF THE NEURAL TISSUE MIMIC

We first utilized the rod shape NTM and observed the effects of cell density on the compaction of the construct when seeded in the PEGDA molds, and later, the neurite extension from the compacted NTM when cultured after compaction. Upon seeding, we measured the dimensions of the compacted NTM for the four concentrations being tested with respect to the

size of the mold, to which the cell-hydrogel solution mimic initially conformed during the stage prior to cross-linking (Figure 3-6a, Figure 3-7). We observed that for the lower 1X concentration, the percent decrease as compared to the original dimension was below 10% by D4 for both the width and the length of the rod (Figure 3-6b). This translated in difficulty of handling the 1X NTMs as they would rupture very easily. When the cell concentrations were increased to 2.5X and 5X concentrations, the width decreased approximately by 30% and 40% respectively, and the length decreased by approximately 50% for both. Interestingly, the highest seeding density showed the least compaction, which could possibly indicate reaching a saturation of cells within the mold volume. NTMs from each group were placed at D4 on functionalized substrates in order to observe the neurite extension, as it was important to ensure that these neural constructs were able to innervate and communicate with downstream biological structures. For this reason, we measured length and number of neurites extending across the periphery of the neural construct. (Figure 3-6c) After two days of the NTM being adhered, we observed numerous processes extending from the NTM beyond an initial sheet of membrane layer directly connected to the NTM. We observed that for lower seeding concentrations, the neurite length reached around 2mm, and significantly decreased for constructs of larger cell concentrations (Figure 3-6d).

Next, the number for neurites extending from the NTM were measured by plotting the cross-sectional profile and counting the peaks (Figure 3-6e). The neurite numbers significantly increased between 1X and 2.5X, and then stayed constant for the subsequent concentrations. The fact that the three highest concentrations seemed to have similar neurite counts, while having such differences in neurite length, could be related to the observed internal clustering of cells (Figure 3-5c). While observing the neurite extension over a longer period of time, beyond the 2nd

day of adhesion (D6+), would have been even more useful, we did observe neurons migrating from the NTM and into the substrate, extending their own processes, and making it hard to distinguish from processes directly extending from the NTM. Nevertheless, these observations led us to select 12.5e6 cells/mL (2.5X) as an appropriate concentration for the rest of the study.

3.3.3 NEURAL TISSUE MIMICS CAN BE MOLDED INTO VARIOUS SHAPES

Upon establishing a reproducible cell culture protocol, we then fabricated molds of different shapes to confirm that mechanical stability observed in the rods would be preserved in other shapes. First, a cube was designed by adjusting the dimensions of the mold to keep the seeding volume constant as the rod design earlier (Figure 3-8a). A similar compaction trend was observed for these cubes, where original volume decreased by approximately 60-70% (Figure 3-8b). To show a possible applicability of cube shaped NTMs for developing 3D neural circuits, we fabricated a holding mold with slits between the enclosures in which to place the compacted cubes. The goal was to add ECM around the cubes and observe if the cubes would extend processes across it (Figure 3-8c). After 4 days of "installation", the cubes were observed to localize towards the center, which would be explained by remodeling of the ECM as neurites extend across and pull on each other. We confirmed by confocal imaging the presence of dense extension of processes between the slits.

In parallel, a mold for a toroid was fabricated in order to obtain a neural ring (Figure 3-8d). The compaction process here was different, as a solid structure held the inner diameter constant, while the outer diameter decreased due to the cell-driven hydrogel compaction, resulting in the thickness decrease by approximately 60% (Figure 3-8e). This shape was especially significant as it proved that the formation of NTMs by these protocols resulted in stable geometries, even if the

NTM was cut in half (Figure 3-9). Furthermore, because the compaction occurred while an external structure kept the cell-matrix liquid, we hypothesized that the structures could be removed and installed onto a cylindrical structure, and (because of the built-in tension), would fit 'tightly'. Using Lightsheet microscopy, we observed that installed rings not only fitted tightly around the cylindrical substrate but also extended a dense mesh of processes (Figure 3-8f).

3.3.4 MATURATION WITHIN THE EXOGENOUS ECM SUPPORTS DEVELOPMENT OF NEURAL POPULATIONS

When presenting this tissue model as a substitute for intact EBs for neural studies, we wanted to determine the effect of disrupting EB cells and then reconstructing them in an exogenous matrix. For this purpose, we focused on common neural populations such as excitatory and inhibitory phenotypes, as well as motor neurons and supporting populations such as astrocytes and oligodendrocytes. Initially, we performed confocal imaging of NTM slices and observed that between D4 and D7, neural populations seemed to be developing as expected (36–38) (Figure 3-10a). The staining for vesicles of the excitatory neurotransmitter, glutamate, showed a wider propagation of these markers across the slice, while markers that stained for the enzymes responsible for synthesis of GABA, a primary inhibitory neurotransmitter, did not show any significant signal. Motor neurons were monitored through the ChAT stain and showed an increase in ChAT+ neurons across the slice between D4 and D7, observation which was similar for the astrocytes and oligodendrocytes stained for GFAP and CNPase, respectively. These observations were confirmed and quantified by qPCR and normalized for comparison across targets with respect to the housekeeping gene GAPDH using standard curves (Figure 3-11). We compared three known targets for excitatory populations: ADORA2a (AD), Grin1 (GR) and TH;

two targets for inhibitory populations: PVALB (PA) and GAD1 (GA); two targets for motor neurons: MNX1 (MN) and ChAT (CH); and two targets for supporting cells: GFAP (GF) and CNPase (CN) (Figure 3-10b). At D0, as expected, MN is expressed various fold higher than most other markers as it is the transcription factor for the differentiation of motor neurons. By D4, MN still expressed highly (with respect to other markers) while CH also expressed highly, indicating maturation of the motor neurons, as CH is critical in the synthesis of the motor neuronal neurotransmitter, acetylcholine. Furthermore, GR, a gene that encodes for the receptor for excitatory neurotransmitter glutamate, became highly expressed while the high expression from D0 of TH, which encodes for dopamine synthesizing enzymes in dopaminergic neurons, showed to be only transient. Prior studies have shown this to be a common occurrence in many developing neurons from the central nervous system (39, 40). More importantly, expression of astrocytes and myelinated oligodendrocytes also increased, almost as much as that of functional motor neurons. On D7, the same trends from D4 were observed, however the expression of the supporting cells surpassed the expression of other markers. Since both astrocytes and oligodendrocytes are mitotic while neurons are generally considered to be amitotic, it would be worth considering how would a large neuron to glial ratio affect 3D culture viability and how this would affect the lifetime of these NTMs. Nevertheless, we also observed the same expression of markers during development in intact EBs that were grown in parallel. (Figure 3-12). We then compared these observations between NTM and EBs for the targets that reported cycle threshold (Ct) values above 35 by D7 (Figure 3-13). When both NTM and EBs were compared at D4 and D7 with respect to pre-dissociation EBs at D0, no significant differences were found for almost any of the markers at both days of study (Figure 3-10c). This served as an indication that the initial disruption and reconstruction of a foreign ECM did not affect the

differentiation and development of general neuronal populations. While this initially was surprising, given the constructs' millimeter-scale sizes which greatly surpassed the EB size and were past the diffusion limit for most tissues, upon imaging the tissues through a scanning electron micrograph (SEM), we observed that the ECM on the outside had pores that were much larger than macromolecules in the media. This would indicate that nutrients were able to diffuse in and out of the tissue (Figure 3-14).

Finally, H&E stains were performed in histology slices to determine the distribution of cells within the NTM (Figure 3-10d). After processing the images, they were segmented in 200µm*200µm sized bins and cells were counted within each bin to have a spatial notion of local cell concentrations (Figure 3-10e). Upon observation, it was apparent that cells, while still alive and distributed across the NTM (which was clear by close inspection of the histology slices), would concentrate closer to the edges and 75% of all cells seemed to be distributed within the first 150µm from the edge. Furthermore, quantifying the expression of the principal ECM proteins in primary neural tissue and comparing between the intact EBs and the *in-vitro* NTM showed again no significant disruption of expression during development (41–44) (Figure 3-15). These observations would suggest that the fabrication of *in-vitro* NTM as demonstrated by this work could serve as a model to study various developmental phenomena despite the disruption of EB development during the formation of the 3D neural constructs.

3.3.5 IN-VITRO NEURAL TISSUE MIMIC DEVELOPS SPONTANEOUS ELECTRICAL ACTIVITY AND SHOWS SPATIAL CONNECTIVITY

While we are able to control the form and shape of the NTM, the electrical functionality must also be validated. Multiple studies of embryoid bodies differentiated to various neuronal

phenotypes have shown the development of spontaneous electrical activity (45–47). To assess the electrical activity, the NTMs were placed on functionalized Micro Electrode Arrays (MEAs). The electrodes that recorded the most activity were directly under the NTM compared to electrodes away from the construct (Figure 3-16a). This activity was quantified primarily by the spike rate and was shown to gradually increase with time, as expected for maturing neural networks (Figure 3-16b, Figure 3-17). Synchronized bursting can be appreciated by the spike raster plots, which showed some random firing from various outside electrodes from migrating neurons but showed structured firing for the electrodes that were under the NTM (Figure 3-16c). Furthermore, quantifying synchronicity of the firing by calculating the average cross-correlation values per electrode with respect to the rest of the electrodes showed synchronous behavior across the length of the construct (Figure 3-16d, Figure 3-18).

Given the conventional perspective that ‘neurons that fire together, wire together’, we inferred that the synchronous bursting observed in the spontaneous activity should indicate a strong connectivity across the tissue. To prove this, we formed NTMs from optogenetic mESC, placed the construct on the MEA after compaction, and used a focused light with a small spot size (~2.5 mm) to stimulate the section of the NTM that was not on the MEA sensing area. This experiment was performed for the rod and the toroid, as the cube dimensions did not allow for the stimulation to be done only on sections that were removed from the recording electrodes (Figure 3-16e). The average firing rates of the 20 s intervals corresponding to before, during, and after stimulation were mapped to their respective electrodes (Figure 3-16f, Figure 3-19). During stimulation away from the measuring electrodes, an increase in firing rate clearly indicates that the processes are electrical connected across the entire NTM. As expected, there would be some variation in the response as the interface between the construct and the measuring electrodes

might not be identical and hence result in a difference in the magnitude of the measured signal. This stimulation was repeated 4 times for two samples of each shape, and the average firing rate for all the electrodes showed a consistent increase in activity from electrodes away from the stimulation (Figure 3-16g). By using a small spot size and stimulating the rod and the toroid on a section of the neural construct away from the electrodes and still detect the evoked response at the electrodes proved that these NTMs were not only spontaneously active but also forming connected networks that extended across the NTM geometry.

3.3.6 NEURAL TISSUE MIMIC FORMATION WITH HUMAN ESC

While utilization of mouse derived embryonic stem cells can still provide an experimental platform for many studies within tissue engineering research, the demonstration of new biofabrication methods in human derived stem cells is highly attractive for the development of translational research models. Using the protocol described earlier in this paper, hESC-derived neural cubes were fabricated (48–50) (Figure 3-20a). For these NTMs, the same cell seeding concentration used for the mouse NTM were mixed with the protein solution used previously and poured into the mold. These NTMs proceeded to compact, showing similar percent volume decrease as the mouse derived NTMs (Figure 3-20b). Furthermore, histology sections showed again similar cell distribution patterns as seen for the mouse-derived NTMs and effective differentiation of excitatory neuronal populations as shown by positive staining of vGlut (51) (Figure 3-20c, Figure 3-21). Moreover, we placed and seeded hESC-derived NTMs on MEAs to validate spontaneous activity from the neural constructs (Figure 3-20d, Figure 3-22). These human-derived constructs showed spontaneous bursting along the action potential firing (Figure 3-20e). More importantly, we measured the response to known neural antagonists from the

seeded NTMs. Following MEA studies with hESC-derived neuronal cultures, spontaneous activity was measured followed by the addition of D-AP5 (30μM), an NMDA receptor antagonist, followed by a washout to determine if the samples would return to baseline firing (47). Afterwards, the inhibitory neurotransmitter GABA was added (100μM), followed by the GABA receptor antagonist bicuculine (30μM). The firing rate responded as expected: addition of D-AP5 decreased the firing rate with respect to the spontaneous activity and returned back when washed away (Figure 3-20f). When GABA was added, a more acute inhibitory response was observed, only to reverse upon the addition of bicuculine. Furthermore, effects to these drugs were also observed in the bursting (Figure 3-20g). Several electrodes had been recording spontaneous bursting, and dissipated when adding the NMDA receptor antagonist, D-AP5, and the inhibitory neurotransmitter GABA. Both washing away the D-AP5 and blocking GABA receptors with bicuculine, resulted in the return of this bursting phenomena, with the latter increasing the number of bursts being recorded. However, while bicuculine did cause more than a two-fold increase of the number of bursts recorded, observing the structure of the burst themselves, there seemed to be no significant difference between the burst duration (Figure 3-20h) or the spike frequency within the burst (Figure 3-20i). These observations led us to conclude that these NTMs could be utilized in translational studies while also taking advantage of the capability of molding the neural constructs in the desired shapes for optimized bottom-up experimental design.

3.4 DISCUSSION

This work demonstrated the fabrication of untethered functional NTMs that can be molded into a variety of 3-dimensional shapes and sizes. Mouse embryonic stem cell-derived neurons, when

mixed with fibrin and ECM and allowed to differentiate in a 3D printed mold, resulted in a compaction of the cells and matrix. This ultimately resulted in a NTM that did not perturb the development of the neural populations when compared with the standard environment of the embryoid body while overcoming geometrical limitations of the spherical EB which at many times restricts experimental design and applications. By providing this reproducible protocol to obtain dense and modular neuronal tissue models, development of novel platforms to assess neural function in 3D can be advanced, since electrophysiological activity and connectivity that extended across the NTM were demonstrated. Finally, we validated our protocol with human stem cell-derived neurons to achieve these functional NTMs. These findings could be enhanced by expanding control of the biofabrication protocol to include higher precision of neuronal population ratios as well as patterning these populations in three dimensions in order to achieve phenotype-specific spatial arrangements and functionality as found in *in-vivo* tissues. The ability to recapitulate neural morphology, both internally and externally, could improve translational applicability as well as present a better model for the study of emergence of neurological phenomena. Overall, these NTMs can have profound applications in drug discovery and screening, as biomedical neural implants, and use in biological robotics and engineering applications

3.5 FIGURES

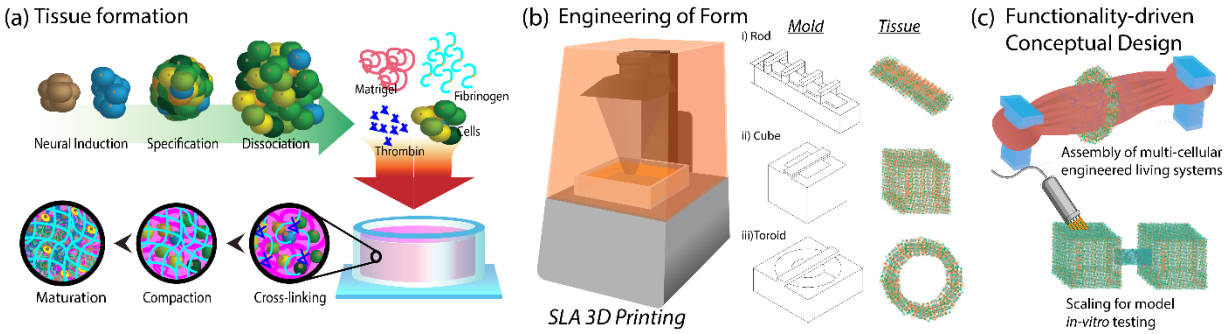

Figure 3-1. Development of 3D neural tissue mimic (NTM) for biomedical engineering applications. (a) Representative schematic of the NTM formation, consisting of differentiation, dissociation and engrafting of differentiated neurons in fibrin hydrogel prior to maturation. (b) Diagram of SLA 3D Printer used for the fabrication of the three molds used to form different neural constructs: rod, cube and toroid. (c) Representation of possible biomedical applications which could benefit from control of the shape and size of neural tissue models.

(a)

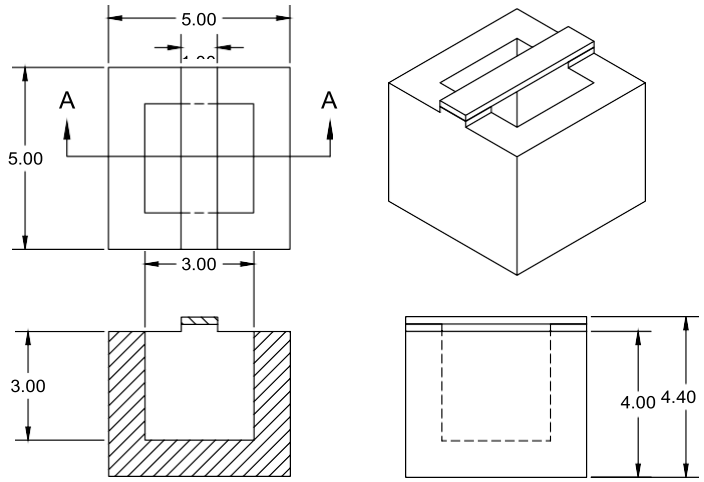

(b)

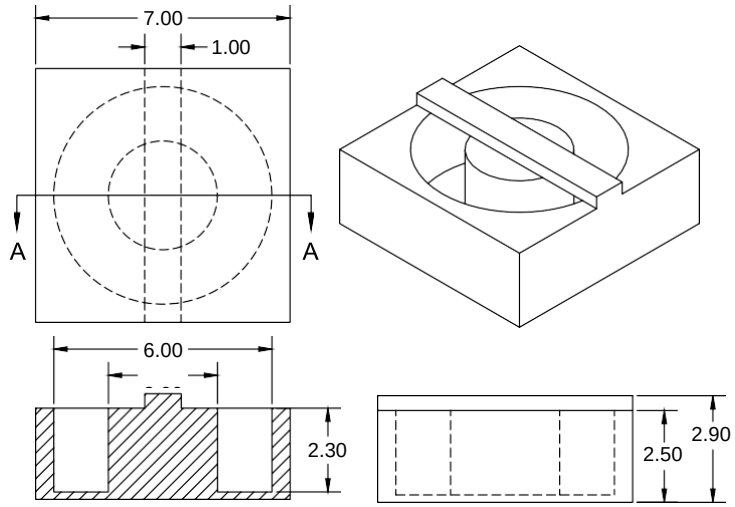

(c)

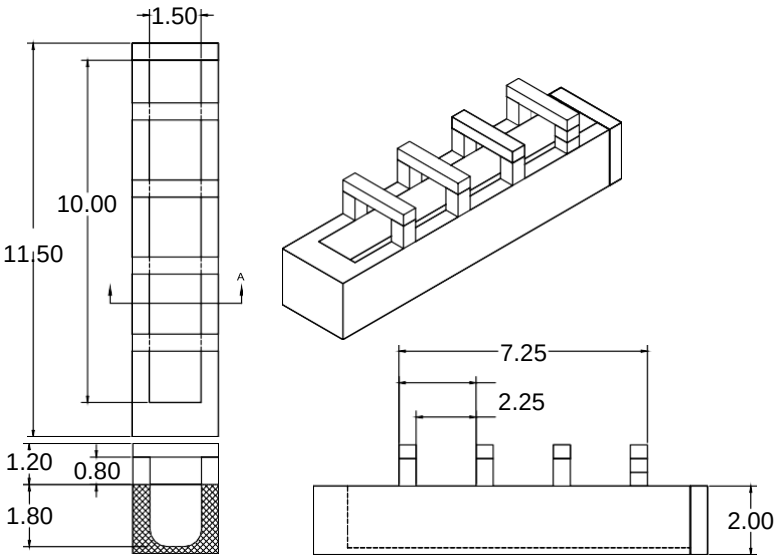

Figure 3-2. Dimensions for molds to form the **(a)** cube tissue, **(b)** toroid tissue and **(c)** rod tissue

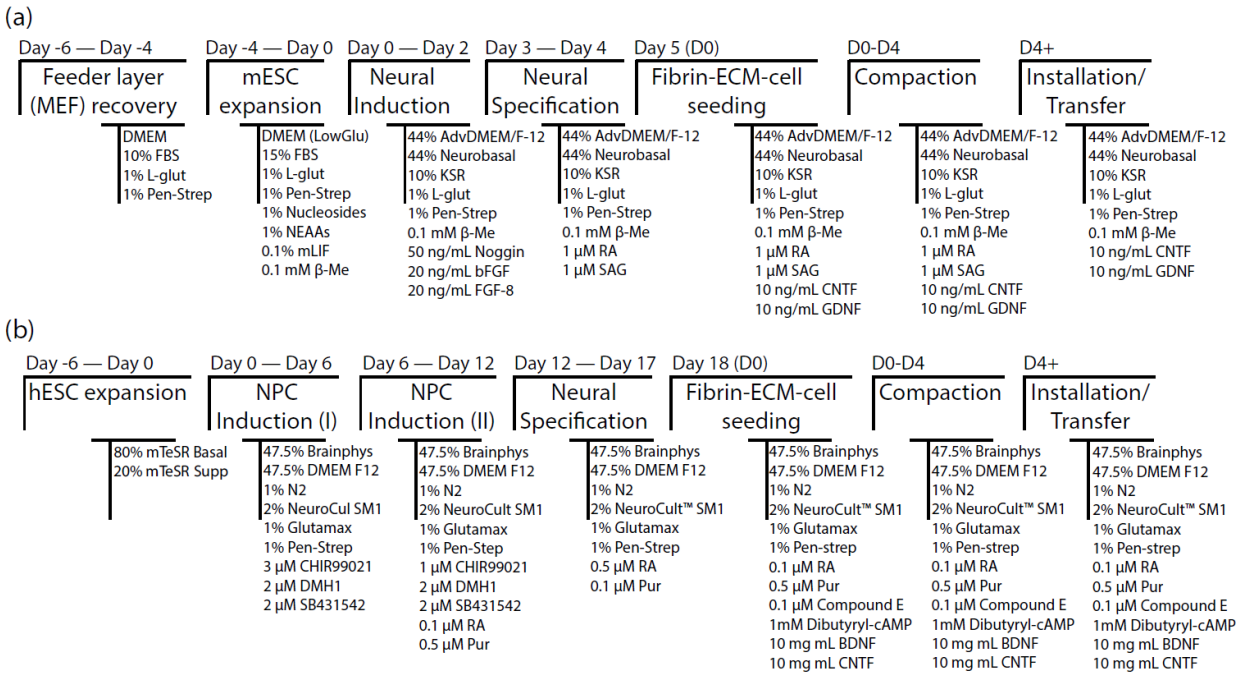

Figure 3-3. Diagrams for culture and differentiation of **(a)** mESCs and **(b)** hESCs.

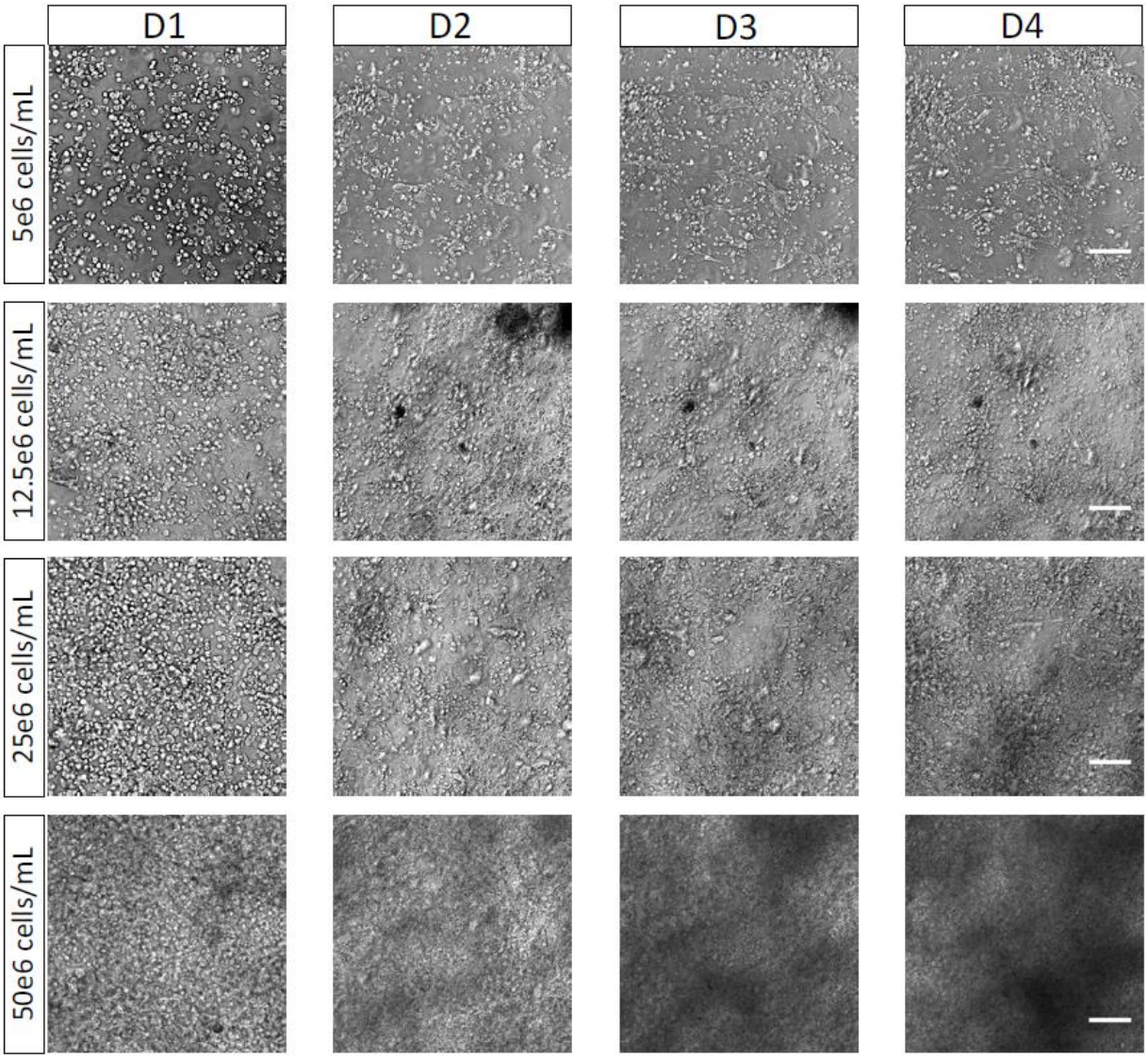

Figure 3-4. Representative images of the development of engrafted neu-rons within the tissue, at D1, D2, D3 and D4, for the 4 seeding cell concentrations studied. (Scale bar: 50 µm)

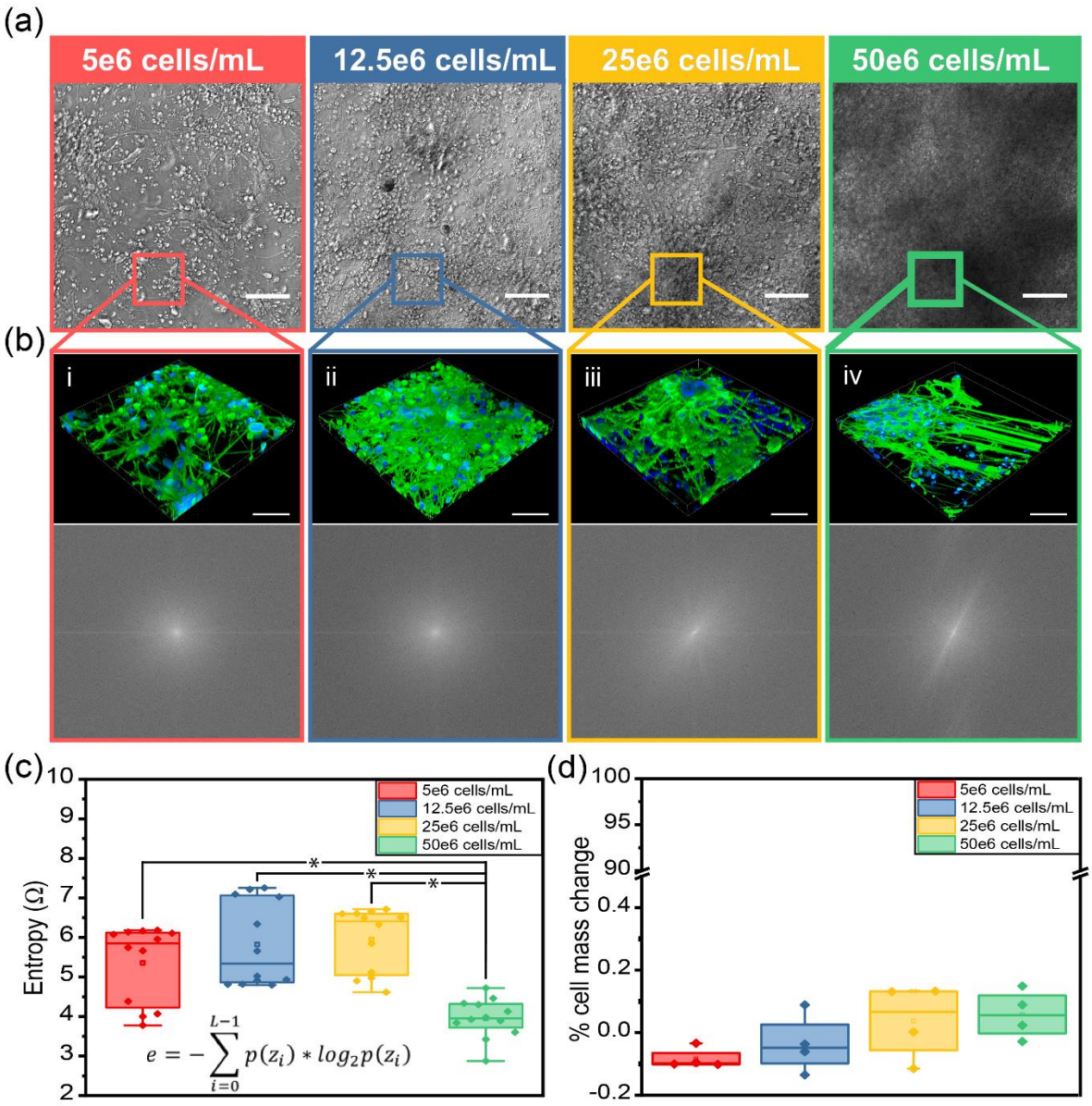

Figure 3-5. Cell seeding density affects homogeneity internal neuronal architecture of NTM. (a) Phase contrast image of the neurons engrafted in fibrin hydrogel at D4 of compaction after neural construct formation for the different seeding cell densities from D0: 5e6 cells/mL, 12.5e6 cells/mL, 25e6 cells/mL and 50e6 cells/mL (scale bar: 50 µm). (b) 3D rendering of confocal z-stacks across 15 µm of neurites (β-TubIII: green) and nuclei (DAPI: blue), with the corresponding representation in the frequency domain obtained through fast Fourier transform for the four cell seeding densities (Scale bar: 20 µm). (c) Entropy of neurite alignment for four seeding densities at D4 (n=12, *p<0.05 ANOVA with Tukey Post Hoc). (d) Cell dry mass change for the four seeding densities between D0 and D4 (n=4).

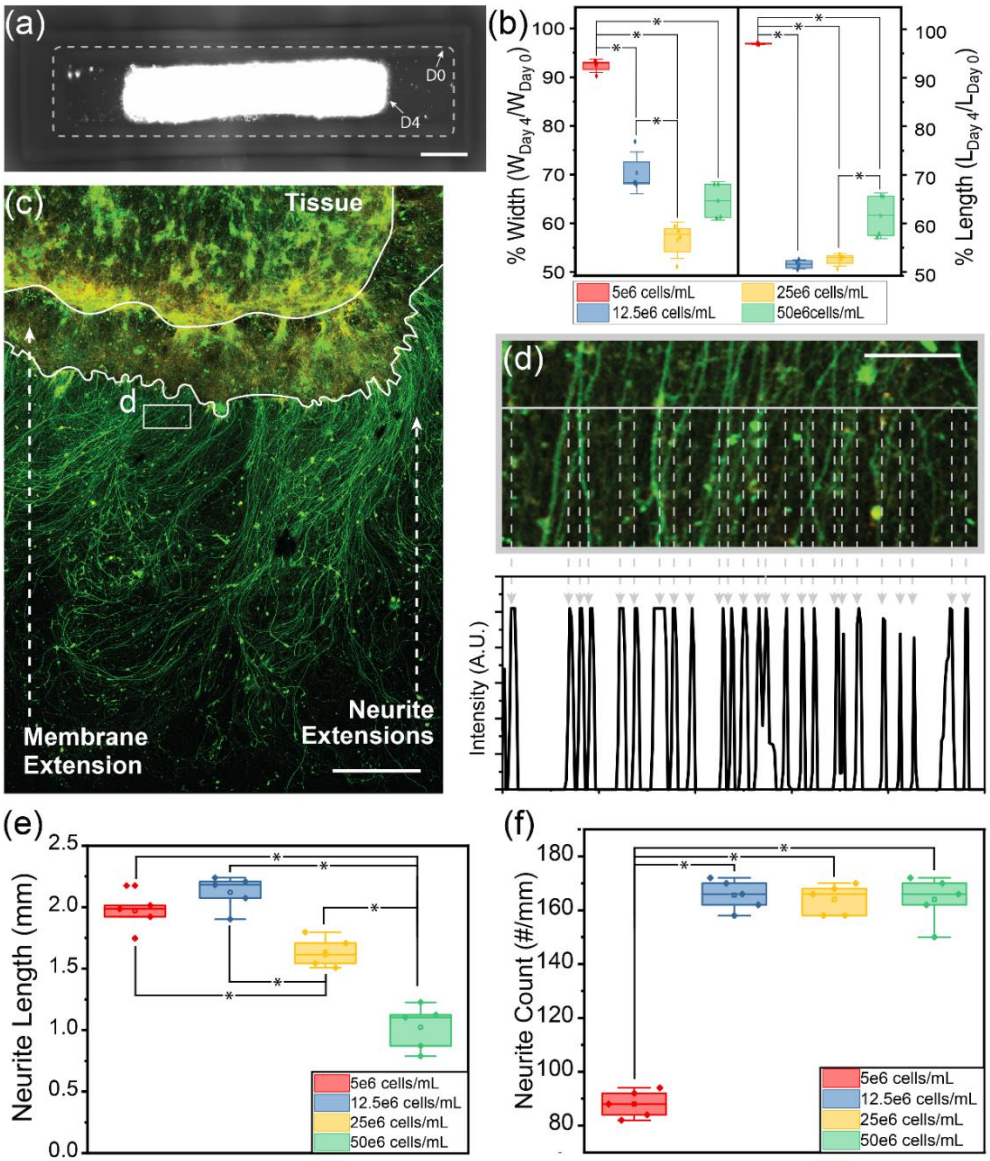

Figure 3-6. Cell seeding density affects compaction and neurite extension from the neural tissue mimic. (a) Representative fluorescent image of a compacting NTM (rod) in the mold at D4 (Scale bar: 1mm). (b) Percent change of the width ($Width_{D4}/Width_{D0}$ *100) and length ($Length_{D4}/Length_{D0}$ *100) of NTMs (rods) resulting from the four cell seeding densities (n=5; *p<0.05 ANOVA with Tukey Post Hoc). (c) Representative confocal image of tissue seeded on functionalized substrate showing neurite extension from the NTM (β-TubIII: green and F-actin: red; Scale bar: 500 µm). (d) Zoom of neurites from (c) across the perimeter of the NTM. Fluorescent intensity profile was used to detect and count neurites (Scale bar: 50 µm). (e) Length of neurites extending from the membrane extension from the NTM for the four cell seeding densities (n=5; *p<0.05 ANOVA with Tukey Post Hoc). (f) Number of neurites per millimeter of NTM perimeter for the different cell seeding densities (n=5; *p<0.05 ANOVA with Tukey Post Hoc).

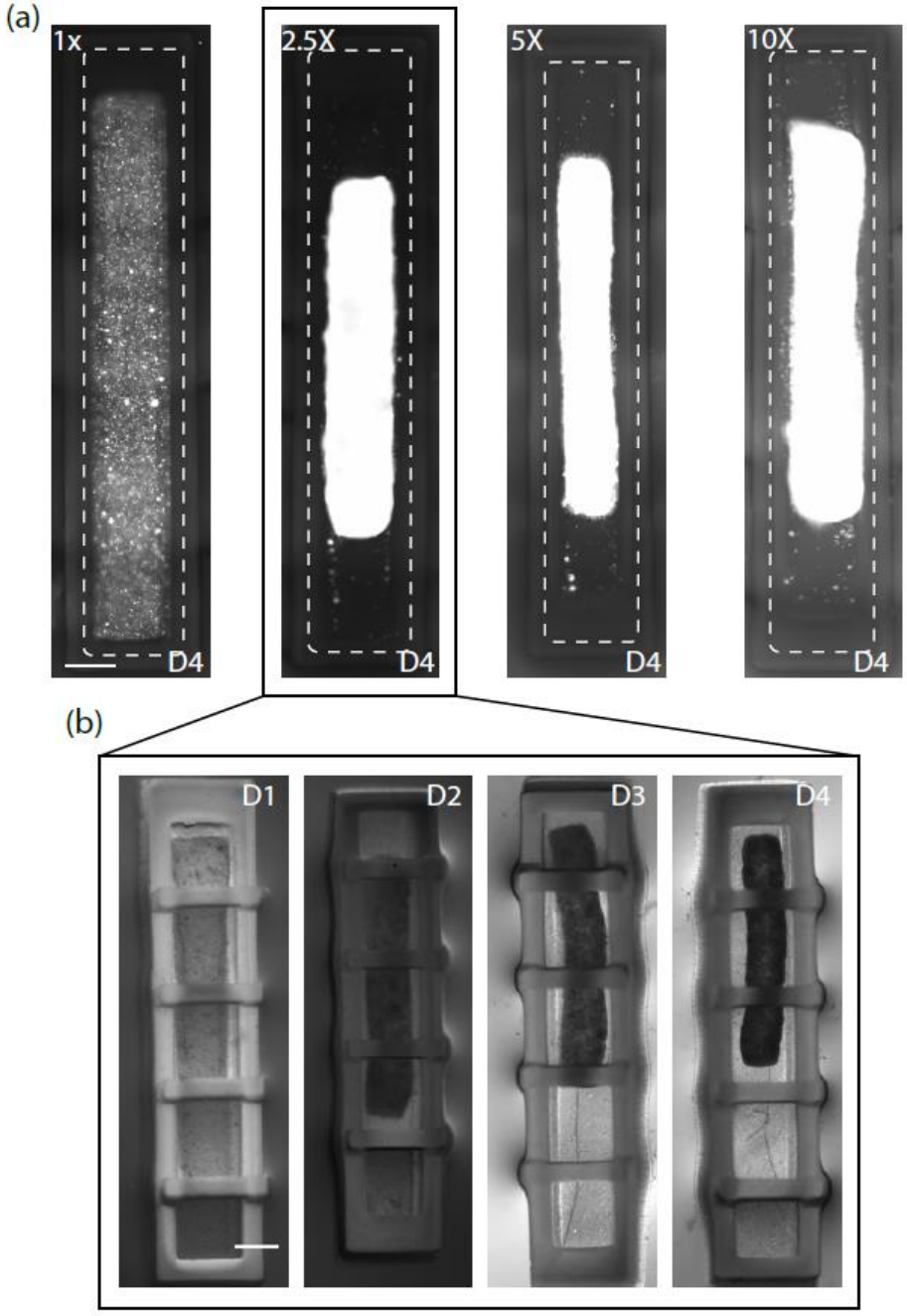

Figure 3-7. Compaction of Rod Tissue. (a) Representative image at D4 of rod tissues seeded at different cell densities. The dashed line shows the mold boundary and the tissue's size at D0 (1X: 5e6 cells/mL; 2.5X: 12.5e6 cells/mL; 5X: 25e6 cells/mL; 10X: 50e6 cells/mL). (b) Representative images of compaction of the rod tissue, seeded at the 2.5X concentration, for D1, D2, D3 and D4. (Scale bar: 1mm)

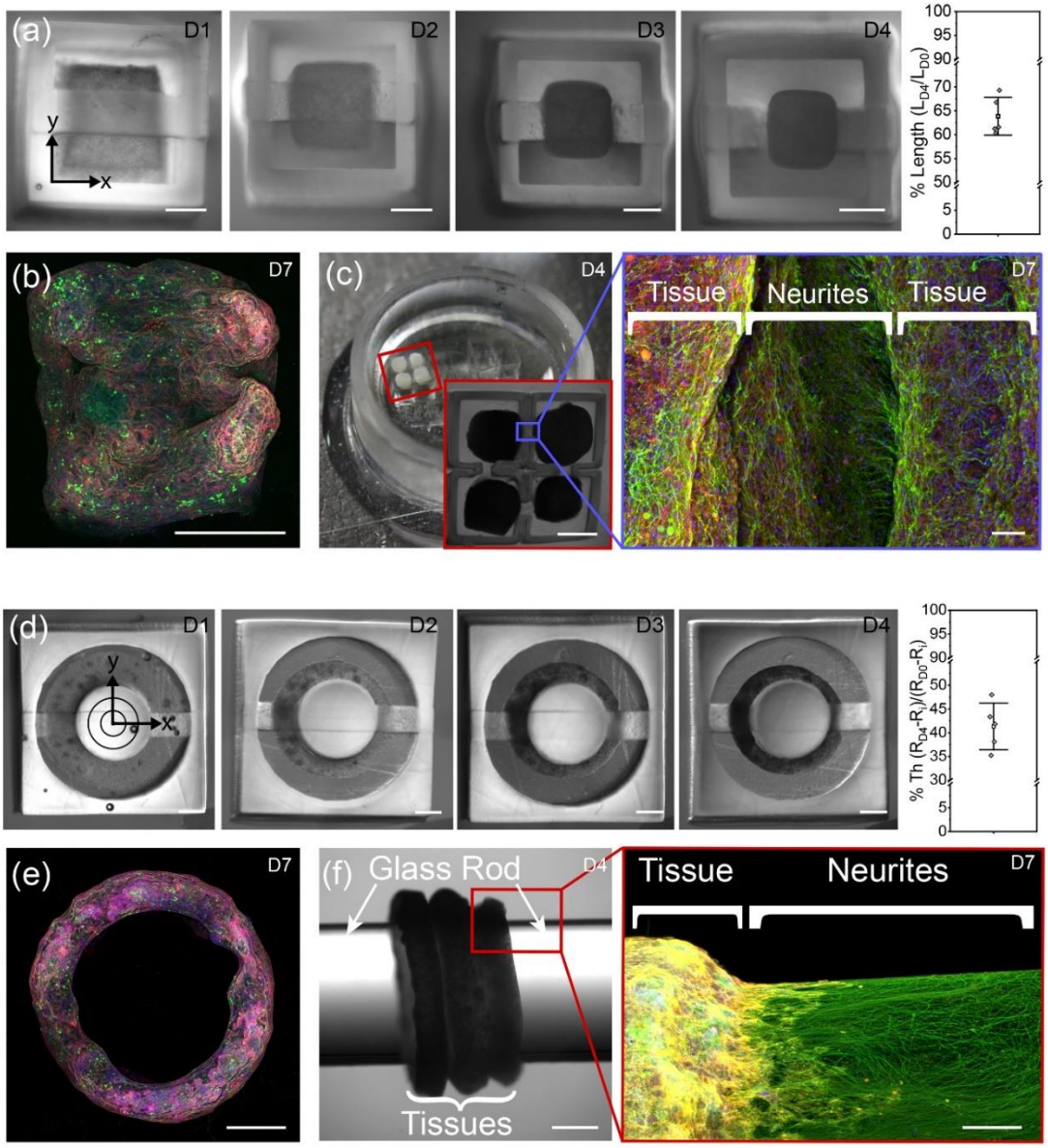

Figure 3-8. Formation of neural tissue mimics of different shapes. (a) Compaction of cube shaped construct during the first 4 days, and percent change of side length [(Average Length at D4)/(Average Length at D0)*100] (Scale bar: 1mm). (b) Confocal of compacted cube NTM (Scale bar: 500 µm). (c) Installation of cube NTMs (D4) on 3D printed holders embedded in Matrigel solution after compaction in the molds. To the right, confocal image of neurites extending between two installed cube NTMs (Scale bar: 1mm; 50 µm). (d) Compaction of toroid shaped NTM during the first 4 days, and percent change of thickness [(Outer Radius at D4 – Inner Radius)/(Outer Radius at D0 – Inner Radius)*100] (Scale bar: 1mm). (e) Confocal of compacted toroid NTM (Scale bar: 1mm). (f) Installation of toroid NTMs (D4) on functionalized glass cylinders after compaction in the mold. To the right, a LightSheet image of neurites extending throughout the glass rod (β-TubIII: green and F-actin: yellow; Scale bar: 1 mm; 500 µm).

Figure 3-9. Section of a Toroid Tissue after being cut, keeping its original curvature. (Scale bar: 1 mm)

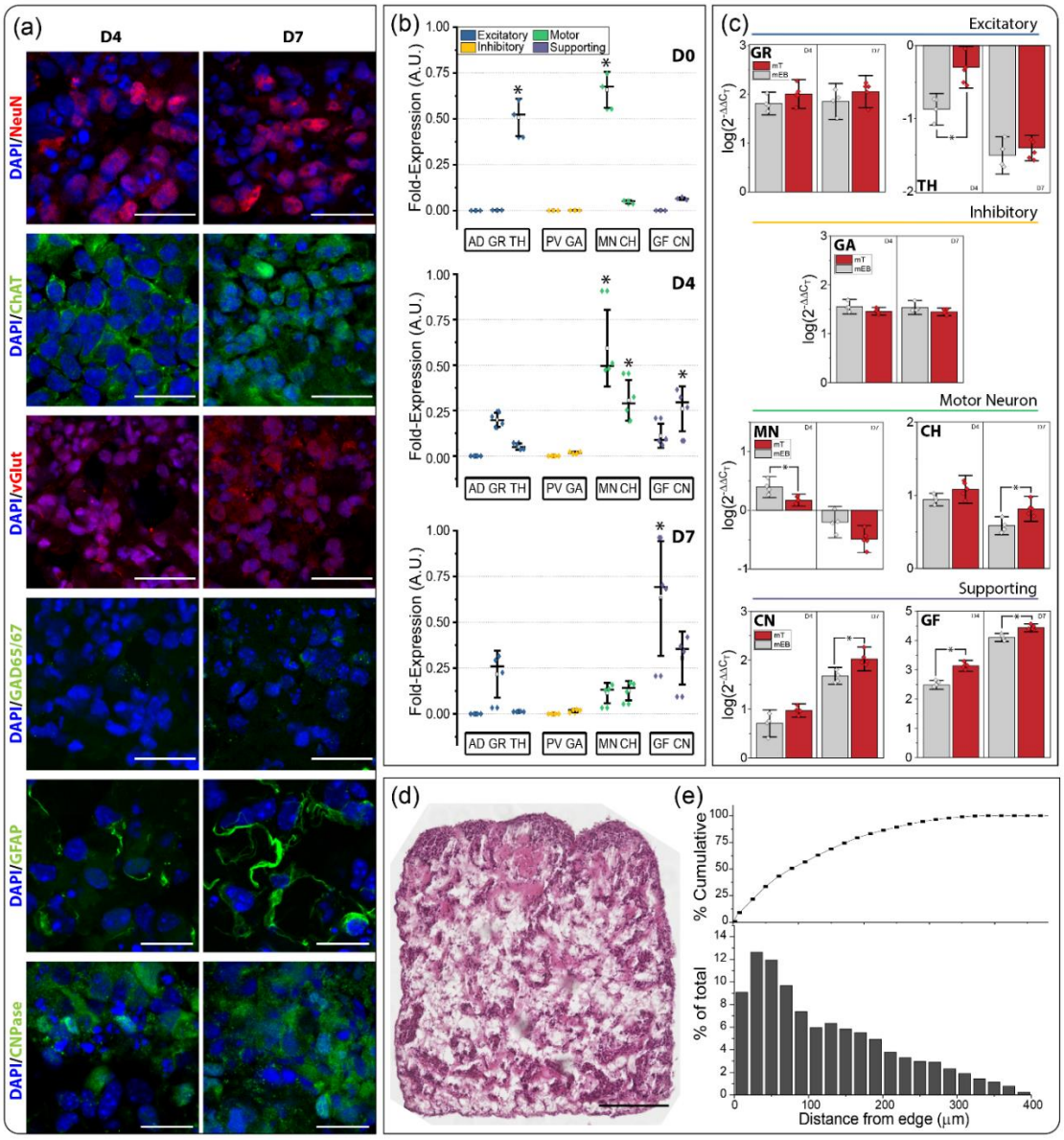

Figure 3-10. Engrafting neuronal populations within fibrin hydrogen did not disrupt phenotypical maturation. (a) Confocal images of 5 µm thick cryosections for key neural populations at D4 and D7 (Scale bar: 25 µm). (b) Fold-expression of RNA expression across normalized population targets with respect to house-keeping gene, GAPDH for D0, D4 and D7 (n=5) [Targets for excitatory neurons (blue): AD-Adora2a, GR-Grin1, TH-Tyrosine Hydroxylase/ Targets for inhibitory neurons (yellow): PV-Parvalbumin, GA-Gad1/ Targets for Motor neurons (green): MN-Mnx1, CH-ChAT/ Targets for supporting cells (purple): GF-GFAP, CN-CNPase]. (c) Comparison between mouse EBs (gray) and NTMs (red) of RNA expression for the population targets with Ct_{adj}<35 @ D7 and with respect to GAPDH, normalized to D0 (n_{MEB}=4, n_{mT}=5; *p<0.05 T-test). (d) Histology of NTM slices at D7 (Scale bar: 200 µm). (e) Histograms of cell position from the nearest edge of the slice, shown in cumulative percentage (top) and percent of total per 20 µm bins (bottom).

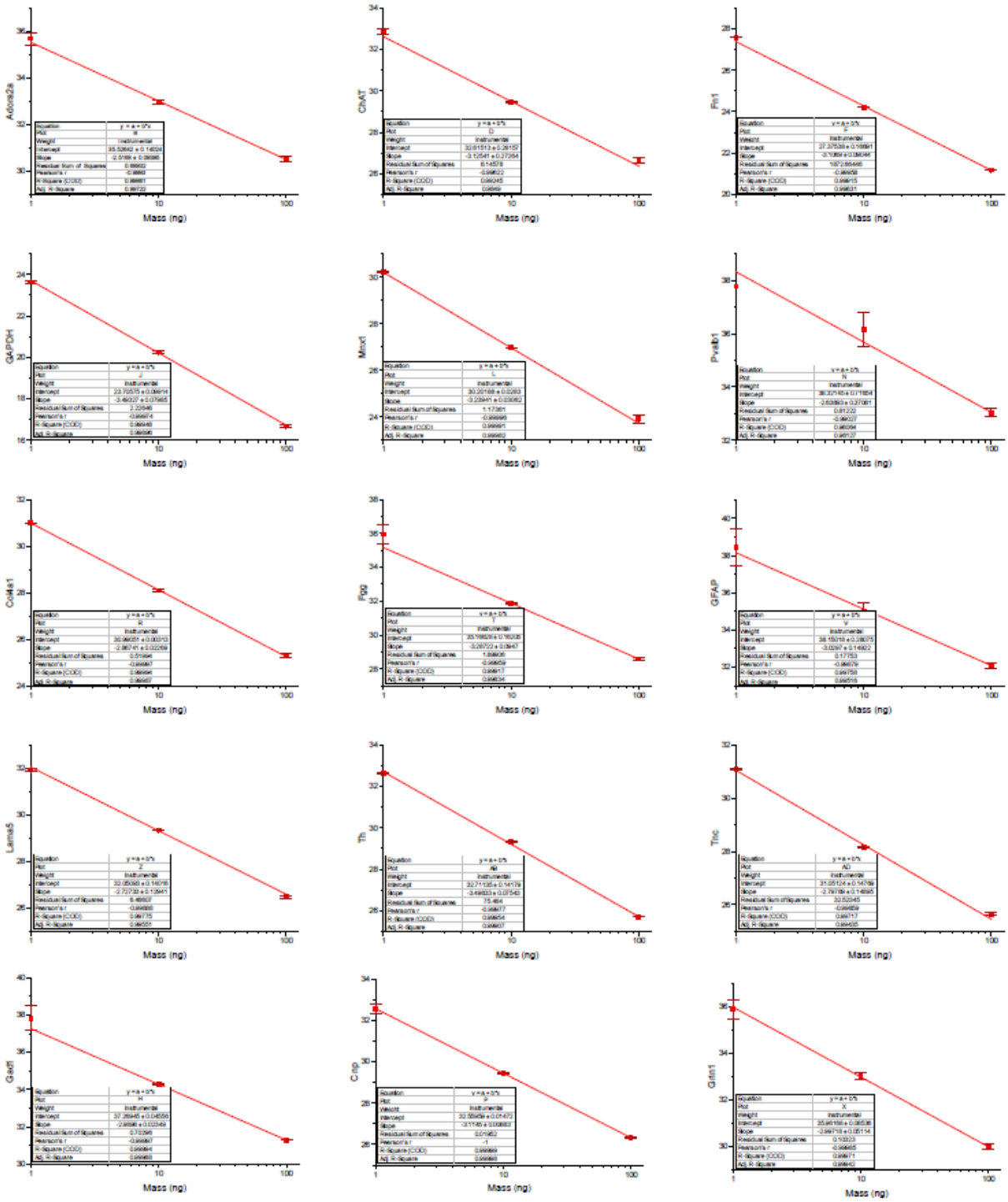

Figure 3-11. Linear fitting of standard curves of PCR targets.

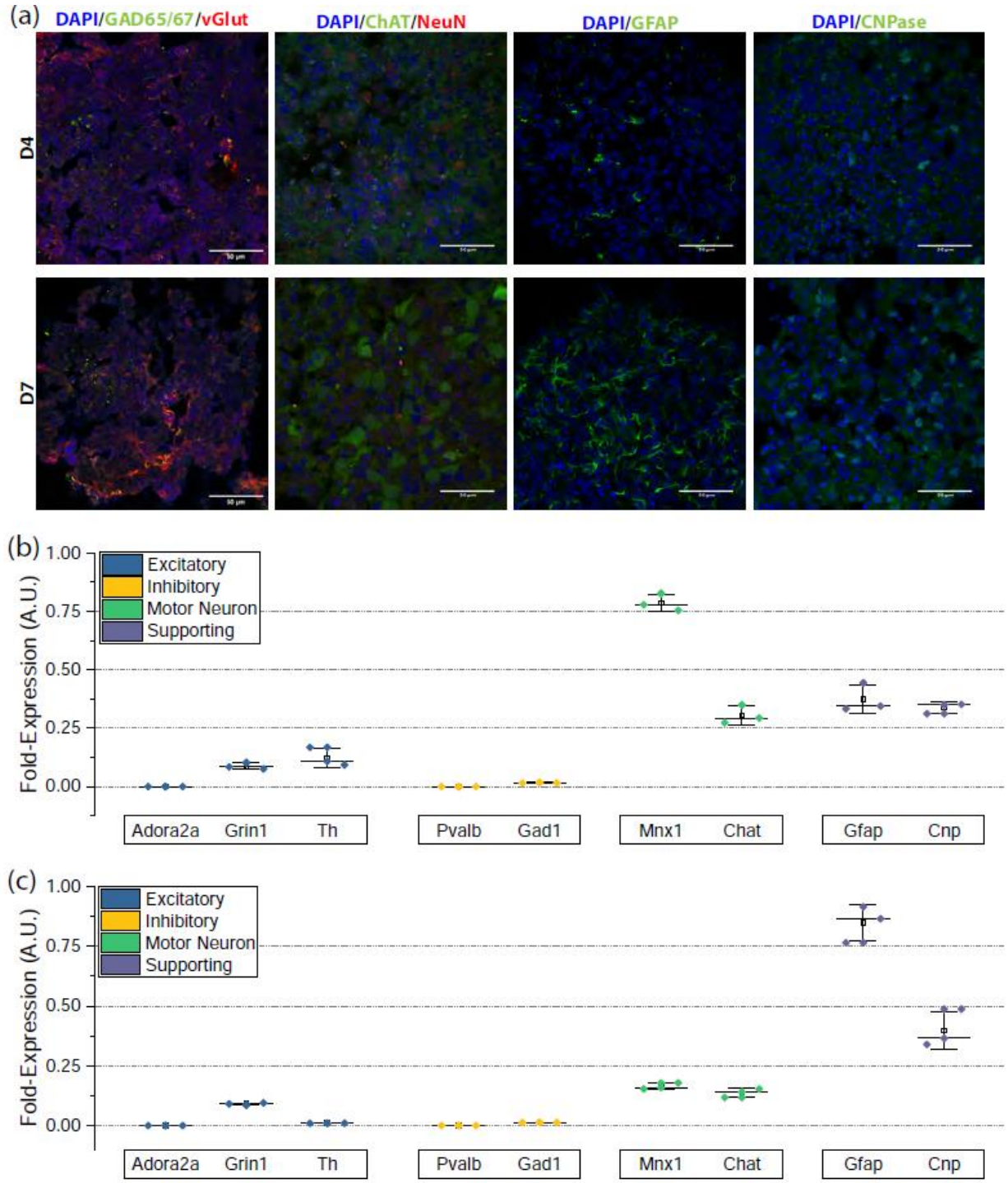

Figure 3-12. Development of neural populations in embryoid bodies. (a) Confocal images of 5 µm thick cryosections for key neural popula-tions at D4 and D7 in mEBs. (Scale bar: 50 µm) Fold-expression of RNA expres-sion was shown across normalized population targets with respect to house-keeping gene, GAPDH for (b) D4 and (c) D7. (n=4)

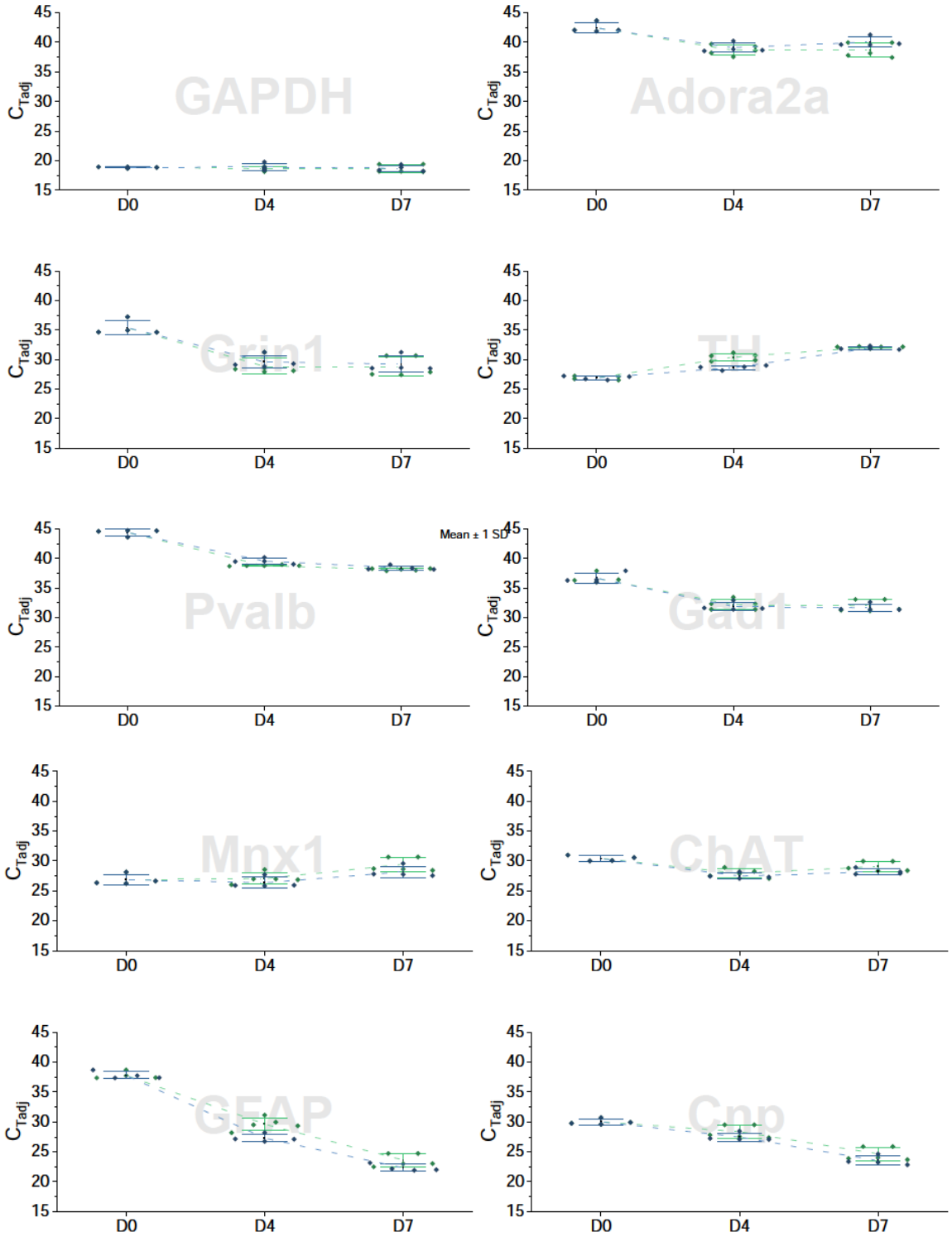

Figure 3-13. Cycle threshold values for population targets for D0, D4 and D7, for mEB (green) and tissue (blue) samples. (whiskers represent SD, $n_{mEB}=4$; $n_{mT}=5$)

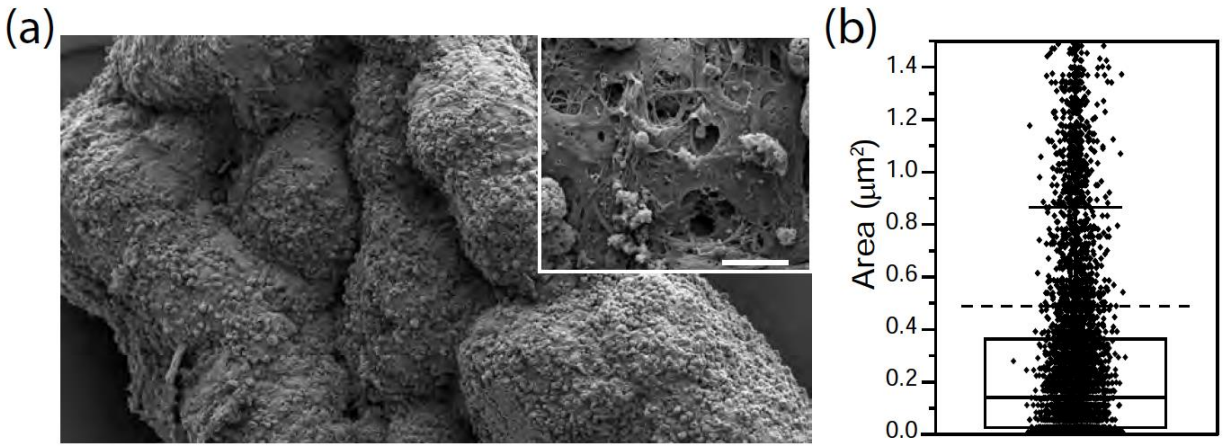

Figure 3-14. Porosity on 3D nerve tissue. (a) Scanning electron micrograph of 3D nerve tissue with zoom in. (Scale bar: 10 μm) (b) Pore area. Box assigns 25-75 percentile, solid line represents the median, dashed line represents the mean.

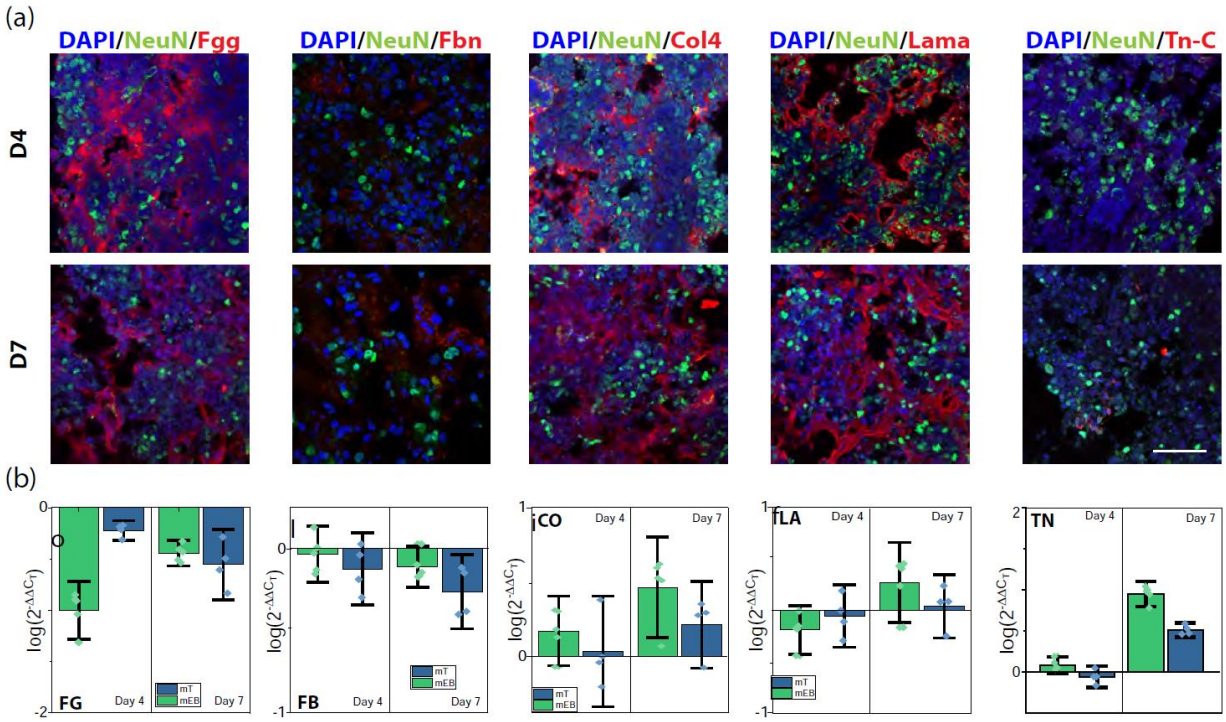

Figure 3-15. ECM secretion within 3D nerve tissue. (a) Confocal images for fibrinogen (to stain the fibrin hydrogel), and four ECMs related to CNS development at D4 and D7. (Scale bar: 50 µm). (b) Comparison between mouse EBs (green) and tissues (blue) of RNA expression for the ECM targets from (a) with Ctadj<35 @ D7 and with respect to GAPDH, normalized to D0. (n_{MEB}=4, n_{mT}=5)

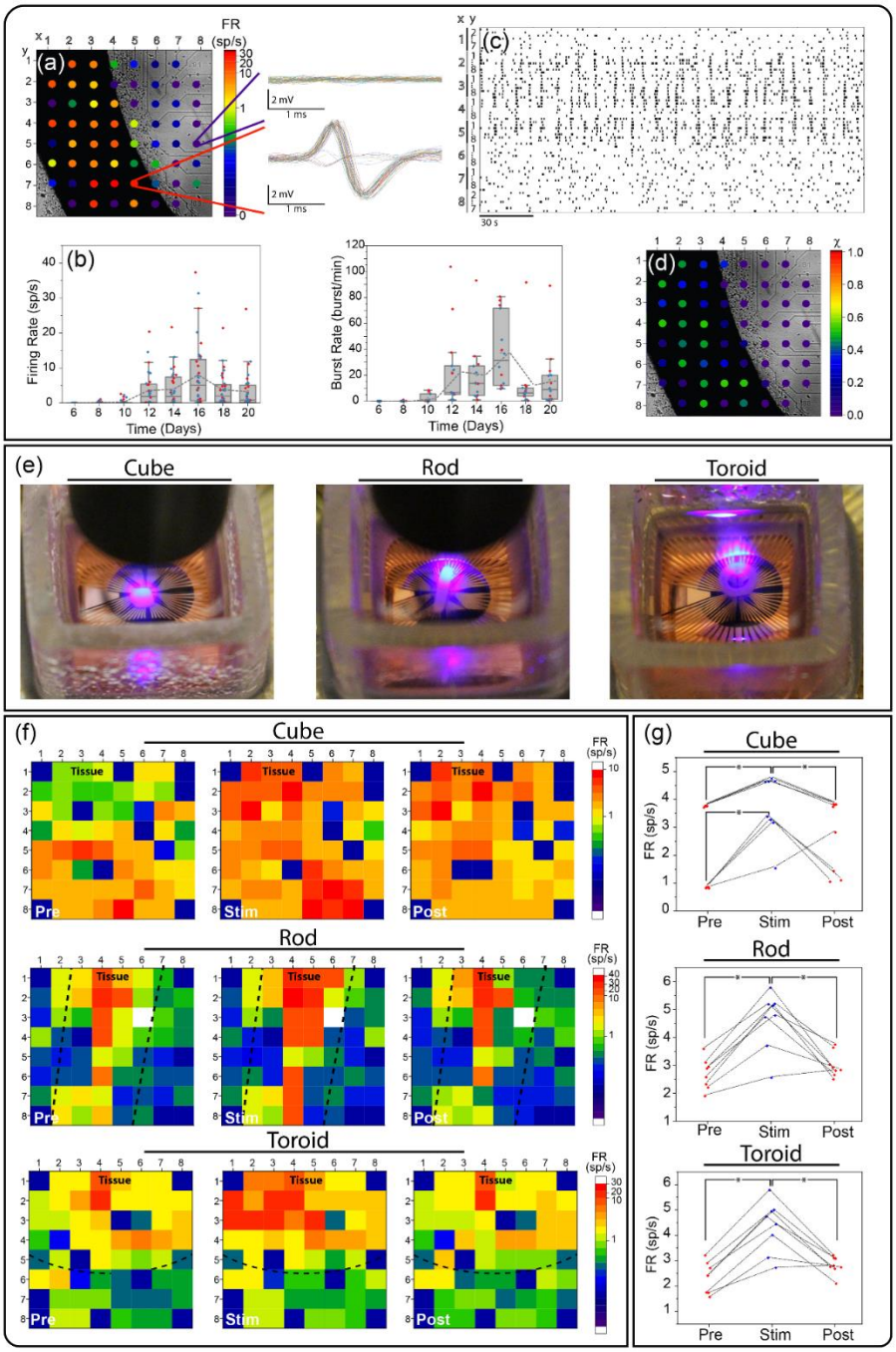

Figure 3-16. Optogenetic neural tissue mimics are spontaneously active and also develop connectivity across the construct. (a) Phase contrast image of a rod NTM on an MEA with electrodes colored for the corresponding averaged measured firing rate (FR) (Spike (SP)/s) for D16. Expansions show overlay of all action potentials recorded in 2 seconds for an electrode far from the NTM (top) and an electrode directly under the NTM (bottom). (b) Firing Spike and Burst Rate for 20 highest recording electrodes for two NTM samples (red and blue) across 16 days (Installed on MEA at D4, started recording 2 days later) (c) Raster plot showing active seconds (seconds where electrodes recorded activity) across all electrode channels for rod NTM for D16. Left legend corresponds to electrode position. (d) Phase contrast image of a rod NTM on an MEA with electrodes colored for the corresponding averaged cross-correlation value normalized to unity for D16. (e) Representative image of focused stimulating incident beam size on the NTM with respect to the section of the structure that is over the recording electrodes for the cube (top), rod (middle) and toroid (bottom). (f) Matrix showing firing rate per electrode, where each element corresponds to each electrode on the MEA for the cube (top), rod (middle) and toroid (bottom). Matrix on the left corresponds to the average firing rate during 20 seconds prior to stimulation, matrix in the center corresponds to the firing rate during 20 seconds of pulsed stimulation illuminated the section of the NTM farthest from the sensing electrodes (for rod and ring), and matrix in the right corresponds to the average firing rate during 20 seconds after stimulation. (g) Firing rate prior (Pre; red), during (Stim; blue) and after (Post; red) stimulation for four stimulation repetitions done on two separate NTMs for the three shapes: cube (top), rod (middle) and toroid (bottom) (n_{Cube}=4, $n_{Rod\ \&\ Toroid}$=8; *p<0.05 ANOVA with Tukey Post Hoc).

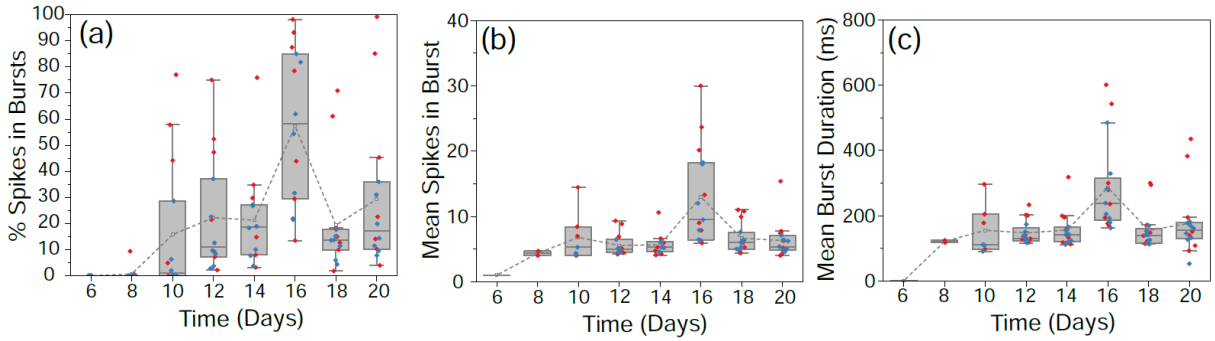

Figure 3-17. Burst Parameters. Bursting was measured and quantified for two tissue samples (red and blue) across 16 days through 4 parameters: (a) percent of spikes fired during bursts versus all fired spikes, (b) average number of spikes per burst and (c) average duration of bursts.

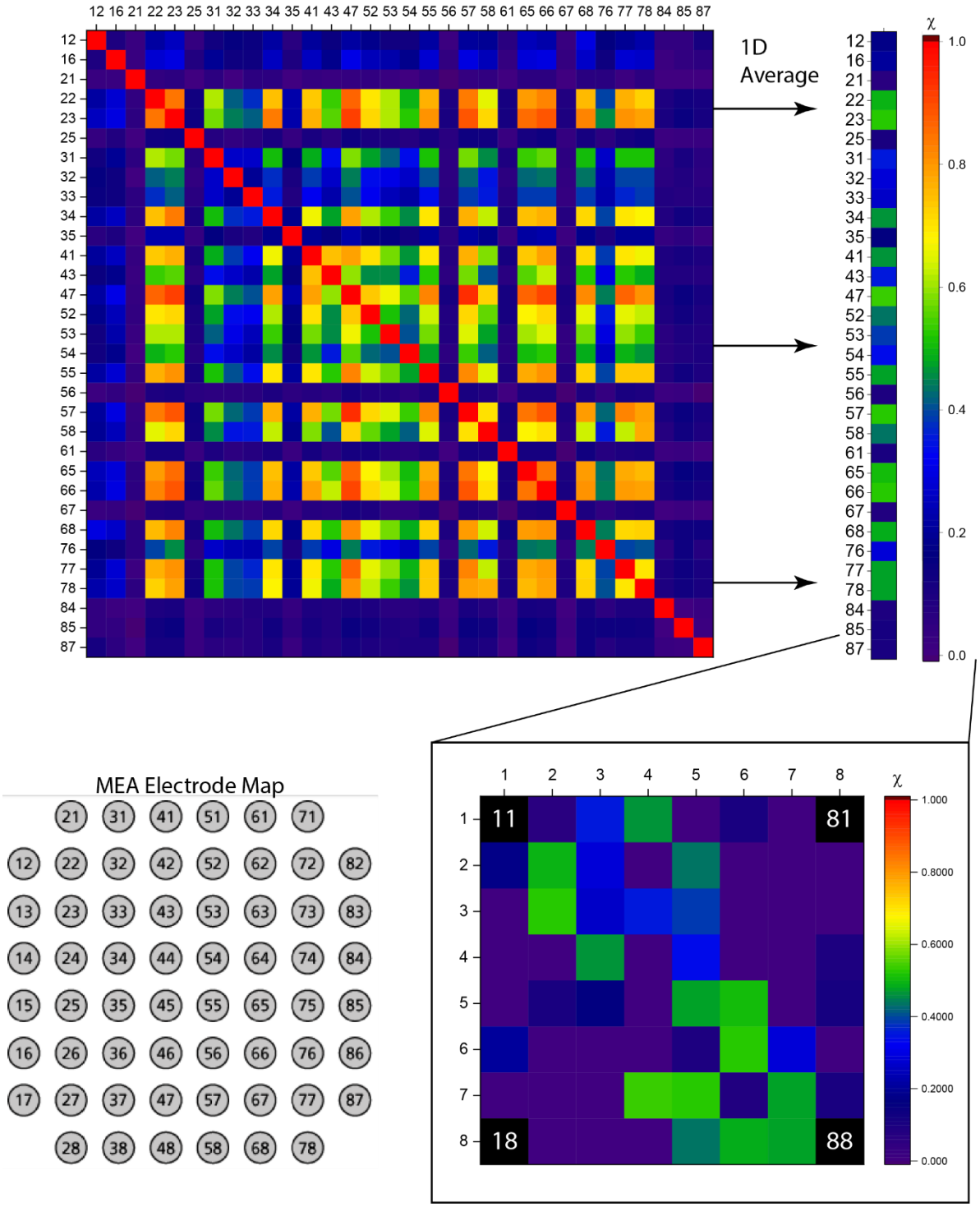

Figure 3-18. Cross-correlation matrix across all active electrodes and mapping to the respective MEA position for the quantification of synchronous activity.

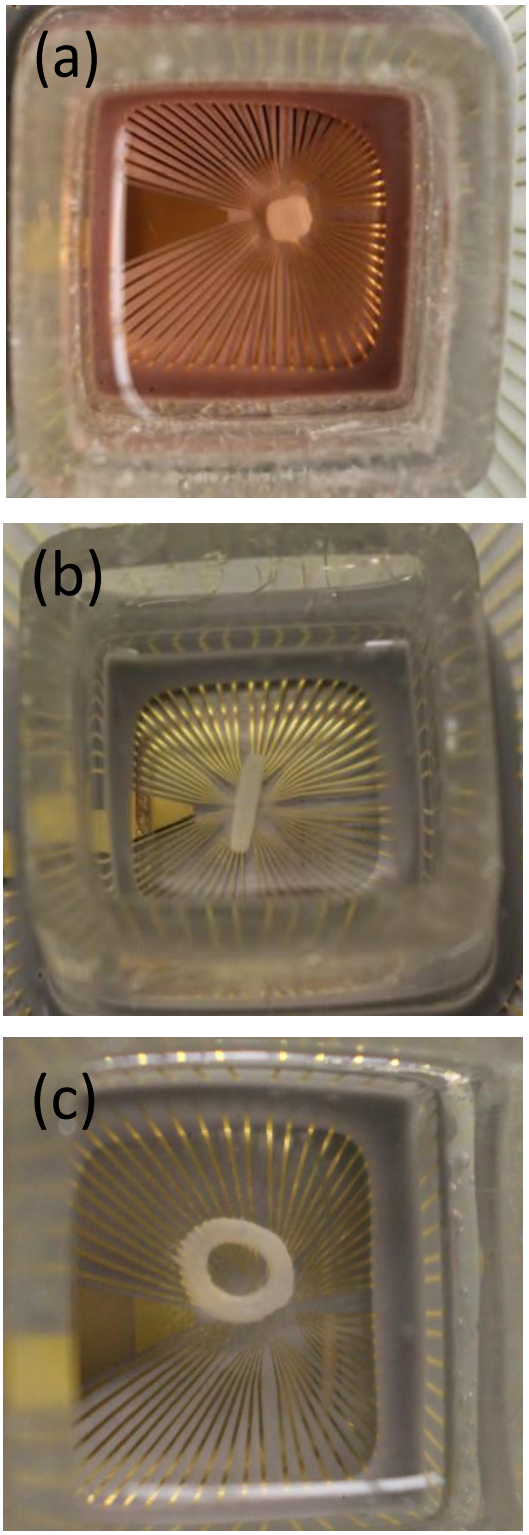

Figure 3-19. Bird's eye image of the placement of the tissues on the MEA of Figure 6 i-k for the (a) cube, (b) rod and (c) toroid.

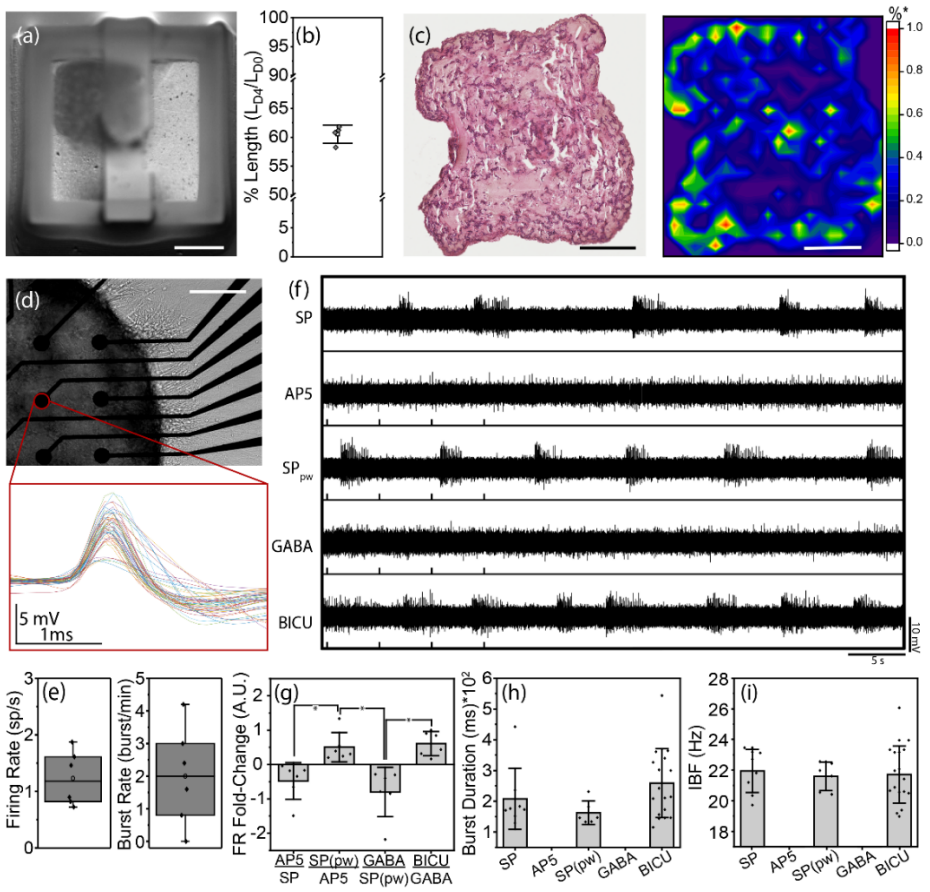

Figure 3-20. hESC-derived neural tissue mimics compact similar to mESC-derived and respond to drugs. (a) Compacted cube NTM formed from hESC at D4. (b) Percent of compaction of the sides [(Average Length at D4)/(Average Length at D0)*100] (n=4; Scale bar: 1mm) (c) Histology of hESC-derived NTM slices at D10 alongside percent of cell count in 100 µm bins to total cell count from histology slices, normalized to 1 [$\%_i = \frac{\text{Cell Count in Bin}_i}{\text{Total Cell Count}}$; $\%^* = \frac{\%_i}{max(\%_i)}$] (Scale bar: 200 µm). (d) hESC-derived cube NTM on MEA, extending processes with representative action potentials recorded from spontaneously firing (Scale bar: 200 µm). (e) Average spike and burst rate during recording of spontaneous activity at D10 (f) Fold-change of average firing rates across active electrodes ($log[FR_{post}/FR_{pre}]$) for six samples between post and pre states corresponding to either addition of drug or washes (AP5:SP → Firing rate after adding D-AP5 with respect to the spontaneous firing rate; SP_{pw}:AP5 →Firing rate after washout with respect to the firing rate during the presence of D-AP5; GABA:SP_{pw} →Firing rate after adding GABA, with respect to the firing rate post washout; BICU:GABA → Firing rate after washing out GABA and adding bicuculline, with respect to firing rate during the presence of GABA) (n=6; *p<0.05, T-test). (g) Representative electrode recording for (from top to bottom): spontaneous, D-AP5, spontaneous post-washout, GABA and bicuculline. Effect of drugs on bursting was evaluated for the recorded bursts through (h) burst duration and (i) spike frequency within each burst.

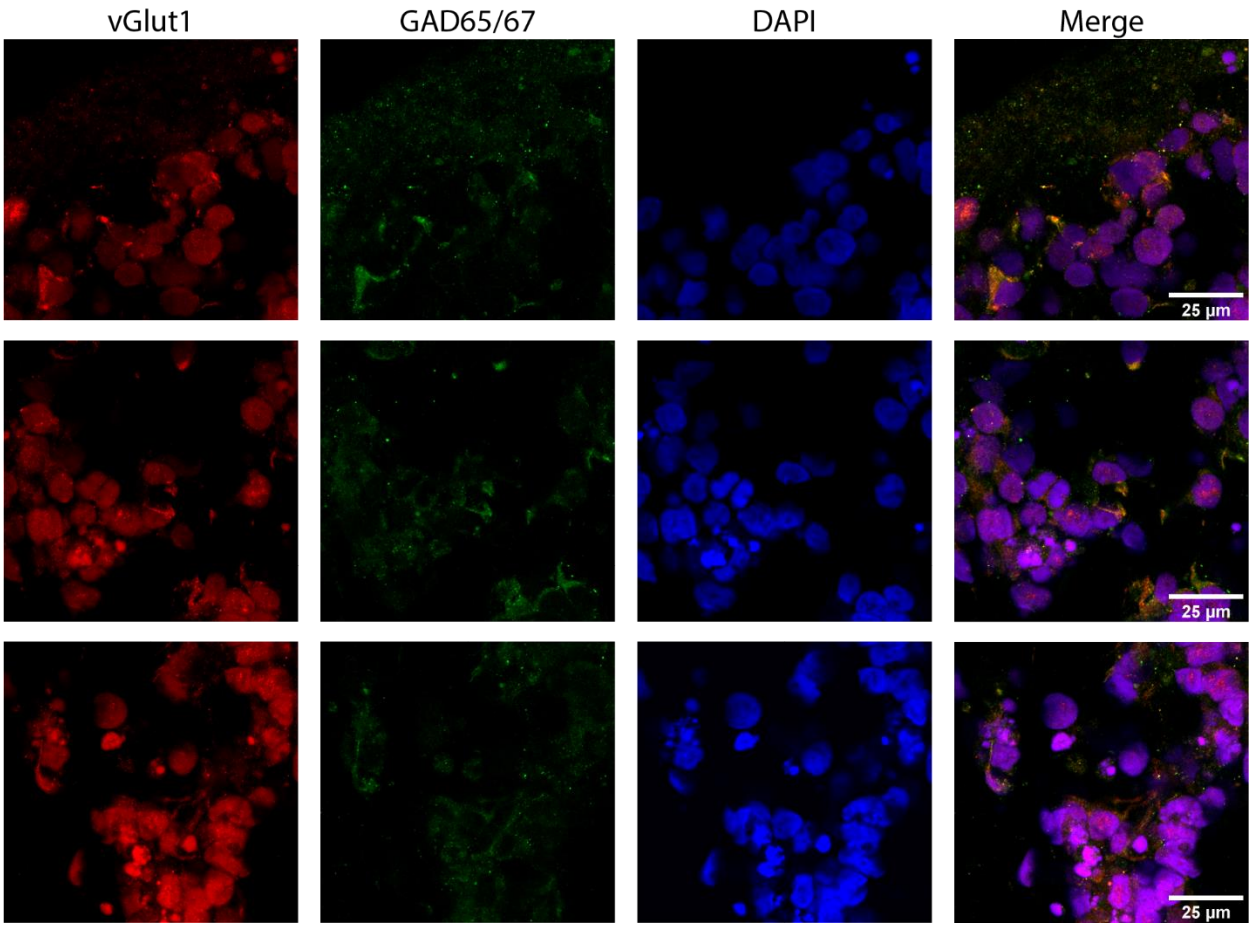

Figure 3-21. Stains for neuronal populations after differentiation from hESCs

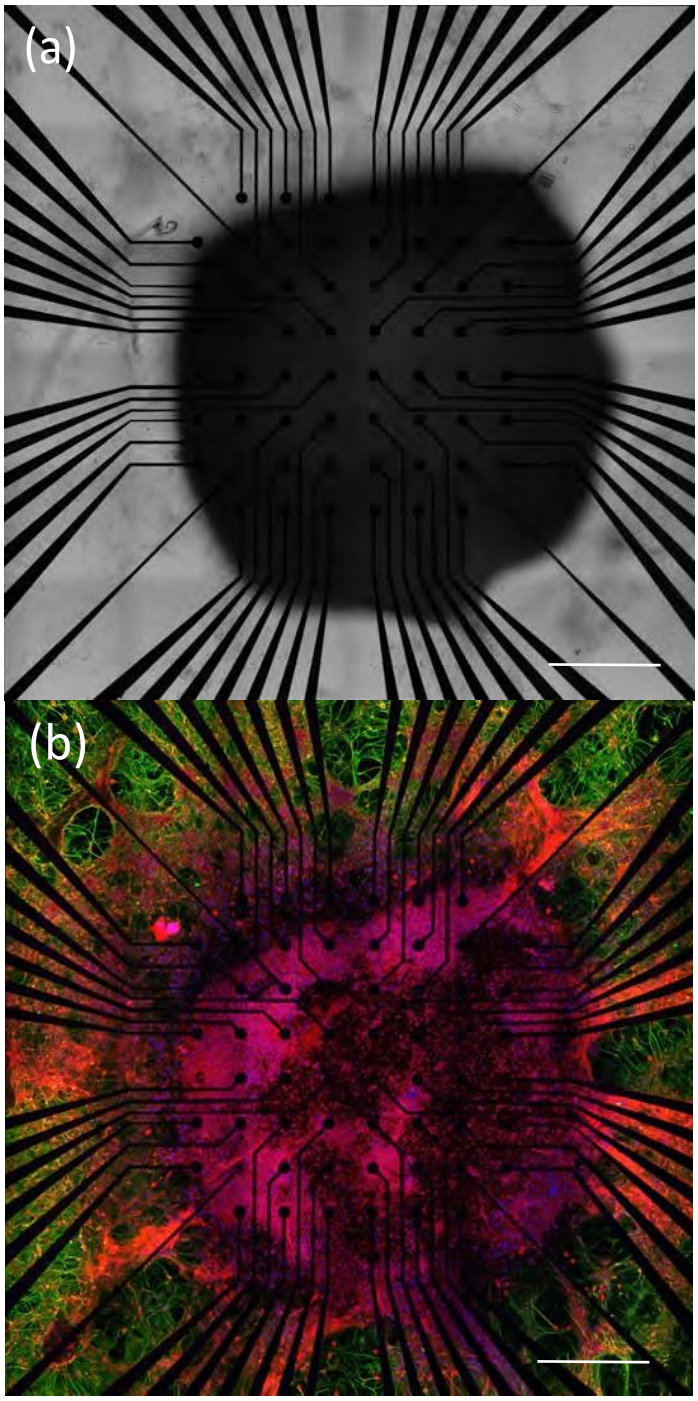

Figure 3-22. Representative confocal images of hESC-derived cube tissues seeded on MEA in (a) brightfield and (b) fluorescence. (Scale bar: 500 μm)

3.6 REFERENCES

1. B. Tian, *et al.*, Macroporous nanowire nanoelectronic scaffolds for synthetic tissues. *Nat. Mater.* **11**, 986–994 (2012).

2. P. Bajaj, R. M. Schweller, A. Khademhosseini, J. L. West, R. Bashir, 3D biofabrication strategies for tissue engineering and regenerative medicine. *Annu. Rev. Biomed. Eng.* **16**, 247–276 (2014).

3. R. D. Kamm, R. Bashir, Creating living cellular machines. *Ann. Biomed. Eng.* **42**, 445–459 (2014).

4. R. M. Duffy, A. W. Feinberg, Engineered skeletal muscle tissue for soft robotics: fabrication strategies, current applications, and future challenges: Engineered skeletal muscle tissue for soft robotics. *Wiley Interdiscip. Rev. Nanomed. Nanobiotechnol.* **6**, 178–195 (2014).

5. M. Thomas, S. M. Willerth, 3-D Bioprinting of Neural Tissue for Applications in Cell Therapy and Drug Screening. *Front. Bioeng. Biotechnol.* **5** (2017).

6. L. Ricotti, *et al.*, Biohybrid actuators for robotics: A review of devices actuated by living cells. *Sci. Robot.* **2**, eaaq0495 (2017).

7. C. Cvetkovic, *et al.*, Three-dimensionally printed biological machines powered by skeletal muscle. *Proc. Natl. Acad. Sci.* **111**, 10125–10130 (2014).

8. S. G. M. Uzel, *et al.*, Microfluidic device for the formation of optically excitable, three-dimensional, compartmentalized motor units. *Sci. Adv.* **2** (2016).

9. R. Raman, *et al.*, Damage, Healing, and Remodeling in Optogenetic Skeletal Muscle Bioactuators. *Adv. Healthc. Mater.* **6** (2017).

10. J. B. Black, P. Perez-Pinera, C. A. Gersbach, Mammalian Synthetic Biology: Engineering Biological Systems. *Annu. Rev. Biomed. Eng.* **19**, 249–277 (2017).

11. W. J. Polacheck, C. S. Chen, Measuring cell-generated forces: a guide to the available tools. *Nat. Methods* **13**, 415–423 (2016).

12. Y. Morimoto, M. Kato-Negishi, H. Onoe, S. Takeuchi, Three-dimensional neuron–muscle constructs with neuromuscular junctions. *Biomaterials* **34**, 9413–9419 (2013).

13. J. A. Umbach, K. L. Adams, C. B. Gundersen, B. G. Novitch, Functional Neuromuscular Junctions Formed by Embryonic Stem Cell-Derived Motor Neurons. *PLOS ONE* **7**, e36049 (2012).

14. J. C. Piña-Crespo, *et al.*, High-Frequency Hippocampal Oscillations Activated by Optogenetic Stimulation of Transplanted Human ESC-Derived Neurons. *J. Neurosci.* **32**, 15837–15842 (2012).

15. M. K. Zachek, P. Takmakov, B. Moody, R. M. Wightman, G. S. McCarty, Simultaneous decoupled detection of dopamine and oxygen using pyrolyzed carbon microarrays and fast-scan cyclic voltammetry. *Anal. Chem.* **81**, 6258–6265 (2009).

16. N. T. Rodeberg, S. G. Sandberg, J. A. Johnson, P. E. M. Phillips, R. M. Wightman, Hitchhiker's Guide to Voltammetry: Acute and Chronic Electrodes for in Vivo Fast-Scan Cyclic Voltammetry. *ACS Chem. Neurosci.* **8**, 221–234 (2017).

17. D. Khodagholy, *et al.*, *In vivo* recordings of brain activity using organic transistors. *Nat. Commun.* **4**, 1575 (2013).

18. C. Cvetkovic, M. H. Rich, R. Raman, H. Kong, R. Bashir, A 3D-printed platform for modular neuromuscular motor units. *Microsyst. Nanoeng.* **3**, 17015 (2017).

19. R. D. Kamm, *et al.*, Perspective: The promise of multi-cellular engineered living systems. *APL Bioeng.* **2**, 040901 (2018).

20. H. B. Baker, J. P. McQuilling, N. M. P. King, Ethical Considerations in Tissue Engineering Research: Case Studies in Translation. *Methods San Diego Calif* **99**, 135–144 (2016).

21. H. Wichterle, M. Peljto, "Differentiation of Mouse Embryonic Stem Cells to Spinal Motor Neurons" in *Current Protocols in Stem Cell Biology*, M. Bhatia, *et al.*, Eds. (John Wiley & Sons, Inc., 2008) https:/doi.org/10.1002/9780470151808.sc01h01s5 (March 8, 2017).

22. R. Z. Hussain, *et al.*, Defining standard enzymatic dissociation methods for individual brains and spinal cords in EAE. *Neurol. Neuroimmunol. Neuroinflammation* **5** (2018).

23. C. L. Chiu, V. Hecht, H. Duong, B. Wu, B. Tawil, Permeability of Three-Dimensional Fibrin Constructs Corresponds to Fibrinogen and Thrombin Concentrations. *BioResearch Open Access* **1**, 34–40 (2012).

24. E. A. Sander, V. H. Barocas, R. T. Tranquillo, Initial Fiber Alignment Pattern Alters Extracellular Matrix Synthesis in Fibroblast Populated Fibrin Gel Cruciforms and Correlates with Predicted Tension. *Ann. Biomed. Eng.* **39**, 714–729 (2011).

25. R. Raman, C. Cvetkovic, R. Bashir, A modular approach to the design, fabrication, and characterization of muscle-powered biological machines. *Nat. Protoc.* **12**, 519–533 (2017).

26. P. K. Jali, M. Donoghue, M. Gadiwan, A rapid manual processing technique for resource-limited small laboratories. *J. Oral Maxillofac. Pathol. JOMFP* **19**, 306–314 (2015).

27. G. Popescu, *Quantitative Phase Imaging of Cells and Tissues* (McGraw-Hill: New York, Chicago, San Francisco, Lisbon, London, Madrid, Mexico City, Milan, New Delhi, San Juan, Seoul, Singapore, Sydney, Toronto, 2011) (September 15, 2019).

28. T. H. Nguyen, M. E. Kandel, M. Rubessa, M. B. Wheeler, G. Popescu, Gradient light interference microscopy for 3D imaging of unlabeled specimens. *Nat. Commun.* **8**, 1–9 (2017).

29. Z. Yan, *et al.*, Three-dimensional mesostructures as high-temperature growth templates, electronic cellular scaffolds, and self-propelled microrobots. *Proc. Natl. Acad. Sci.* **114**, E9455–E9464 (2017).

30. S. M. Willerth, K. J. Arendas, D. I. Gottlieb, S. E. Sakiyama-Elbert, Optimization of Fibrin Scaffolds for Differentiation of Murine Embryonic Stem Cells into Neural Lineage Cells. *Biomaterials* **27**, 5990–6003 (2006).

31. A. R. Bento, P. Quelhas, M. J. Oliveira, A. P. Pêgo, I. F. Amaral, Three-dimensional culture of single embryonic stem-derived neural/stem progenitor cells in fibrin hydrogels: neuronal network formation and matrix remodelling. *J. Tissue Eng. Regen. Med.* **11**, 3494–3507 (2017).

32. A. R. Wufsus, *et al.*, Elastic Behavior and Platelet Retraction in Low- and High-Density Fibrin Gels. *Biophys. J.* **108**, 173–183 (2015).

33. K. A. Jansen, P. Atherton, C. Ballestrem, Mechanotransduction at the cell-matrix interface. *Semin. Cell Dev. Biol.* **71**, 75–83 (2017).

34. A. P. V. Winkle, I. D. Gates, M. S. Kallos, Mass Transfer Limitations in Embryoid Bodies during Human Embryonic Stem Cell Differentiation. *Cells Tissues Organs* **196**, 34–47 (2012).

35. R. C. Gonzalez, R. E. Woods, S. L. Eddins, *Digital Image Processing Using MATLAB* (Prentiss Hall, 2003).

36. P. Tanapat, Neuronal Cell Markers. *Mater. Methods* (2016) (November 25, 2017).

37. A. Czechanski, *et al.*, Derivation and characterization of mouse embryonic stem cells (mESCs) from permissive and non-permissive strains. *Nat. Protoc.* **9**, 559–574 (2014).

38. T. Kodama, *et al.*, Neuronal classification and marker gene identification via single-cell expression profiling of brainstem vestibular neurons subserving cerebellar learning. *J. Neurosci. Off. J. Soc. Neurosci.* **32**, 7819–7831 (2012).

39. N. Matsushita, *et al.*, Dynamics of tyrosine hydroxylase promoter activity during midbrain dopaminergic neuron development. *J. Neurochem.* **82**, 295–304 (2002).

40. E. Weihe, C. Depboylu, B. Schütz, M. K.-H. Schäfer, L. E. Eiden, Three Types of Tyrosine Hydroxylase-Positive CNS Neurons Distinguished by Dopa Decarboxylase and VMAT2 Co-Expression. *Cell. Mol. Neurobiol.* **26**, 659–678 (2006).

41. E. V. Jones, D. S. Bouvier, Astrocyte-Secreted Matricellular Proteins in CNS Remodelling during Development and Disease. *Neural Plast.* **2014** (2014).

42. C. S. Barros, S. J. Franco, U. Müller, Extracellular Matrix: Functions in the nervous system. *Cold Spring Harb. Perspect. Biol.* **3**, 1–24 (2011).

43. K. S. Midwood, M. Chiquet, R. P. Tucker, G. Orend, Tenascin-C at a glance. *J Cell Sci* **129**, 4321–4327 (2016).

44. J. Chen, *et al.*, The Extracellular Matrix Glycoprotein Tenascin-C Is Beneficial for Spinal Cord Regeneration. *Mol. Ther.* **18**, 1769–1777 (2010).

45. M. M. Daadi, *et al.*, Optogenetic Stimulation of Neural Grafts Enhances Neurotransmission and Downregulates the Inflammatory Response in Experimental Stroke Model. *Cell Transplant.* **25**, 1371–1380 (2016).

46. P. Soundararajan, Motoneurons Derived from Embryonic Stem Cells Express Transcription Factors and Develop Phenotypes Characteristic of Medial Motor Column Neurons. *J. Neurosci.* **26**, 3256–3268 (2006).

47. T. J. Heikkilä, *et al.*, Human embryonic stem cell-derived neuronal cells form spontaneously active neuronal networks in vitro. *Exp. Neurol.* **218**, 109–116 (2009).

48. M. D. Neely, *et al.*, DMH1, a Highly Selective Small Molecule BMP Inhibitor Promotes Neurogenesis of hiPSCs: Comparison of PAX6 and SOX1 Expression during Neural Induction. *ACS Chem. Neurosci.* **3**, 482–491 (2012).

49. S. M. Chambers, *et al.*, Combined small molecule inhibition accelerates developmental timing and converts human pluripotent stem cells into nociceptors. *Nat. Biotechnol.* **30**, 715–720 (2012).

50. W. Li, *et al.*, Rapid induction and long-term self-renewal of primitive neural precursors from human embryonic stem cells by small molecule inhibitors. *Proc. Natl. Acad. Sci. U. S. A.* **108**, 8299–8304 (2011).

51. J. C. Butts, *et al.*, Differentiation of V2a interneurons from human pluripotent stem cells. *Proc. Natl. Acad. Sci. U. S. A.* **114**, 4969–4974 (2017).

CHAPTER 4: SIMULATION AND FABRICATION OF STRONGER, LARGER AND FASTER WALKING BIOHYBRID MACHINES[1]

4.1 INTRODUCTION

While engineering biohybrid robots that utilize hydrogels as biomaterials and biocompatible scaffolds has become a growing field in the last decade, the design approaches have been mostly by trial and error.(1–7) This can be particularly disadvantageous considering the large amount of time and resources required to perform design troubleshooting. This points to a necessity of improving upon the method of designing function-specific biological machines. These soft robots primarily consist of actuating cells, such as cardiac or skeletal muscle cells, within or around a hydrogel which permits the differentiation and maturation of these cells while providing structural and physical cues for the formation of functional (i.e. contracting) tissue. (3, 8–11) The scaffolds provide the 'form' and are used to convert the 'function' from the tissue into a controlled output, for example some manner of locomotion such as swimming or walking.(1, 4–6, 12) These scaffolds can be highly customizable through development of 3D printing techniques such as stereolithography, which permit these biological machines to have multiple shapes, and applicable to numerous muscle tissue geometries and functional outputs.(8, 10, 11, 13, 14) Despite this design flexibility, in order to achieve effective forward engineering of biological machines with targeted performance, a critical necessity is the ability to model the

[1] This section is a reproduction of the following first authored journal article:
Pagan-Diaz, G. J., Zhang, X., Grant, L., Kim, Y., Aydin, O., Cvetkovic, C., Ko, E., Solomon, E., Hollis, J., Kong, H. J., Saif, T., Gazzola, M., Bashir, R. Simulation and Fabrication of Stronger, Larger, and Faster Walking Biohybrid Machines. *Adv. Funct. Mater.* 2018, 28, 1801145. https://doi.org/10.1002/adfm.201801145

Author Contributions: G.J.P.-D. designed research, performed research, analyzed data; X.Z. and M.G. contributed the computational models and analysis of data and also provided the Appendix 1, L.G., Y.K., O.A., C.C., C.K., E.S., J.H., J.K. and T.S. performed experiments and contributed with analysis; R.B. led project and designed research, G.J.P.-D., X.Z., M.G. and R.B. wrote and edited the paper.

interaction between the contractile tissue and its interaction with the actuating scaffold to predict its functional output.

One key factor in order to achieve ground up engineering of new biohybrid systems is to analytically characterize new design parameters in order to expand the breadth of possible applications. The goal is to design these biological machines with a high degree of control, tissue-to-scaffold dynamics, and longevity, among other parameters. Such advances include the use of light to temporally control muscle contractions, micro-patterning to achieve spatial coordination of contraction, and incorporation of biomolecules to control the degradation of the structural matrix.(15–17)

Force generation to drive actuation is one of the most critical parameters in engineering of skeletal muscle tissue constructs. Being able to scale up the force would enable the formation of larger or more complex systems, as well as adding new levels of functionality. Currently, the largest force achieved in biohybrid tissues has been reported to be 1.18 mN, with a structure of four stacks of cardiac 1.16 ± 0.08 cm^2 2D sheets of thickness of 45 ± 8 μm.(18) However, this was achieved on a fixed scaffold. While untethered biological machines have been designed to walk, their current force per stroke during external stimulation was 200 μN for a design with a largest dimension of 6 mm.(19) There are many biological factors that affect force generation in myogenic tissue, such as the cell source or biomolecular pathways that regulate the metabolism, or differentiation of the myofiber type.(20) However, these are hard to control and often require a complex regulation of gene expression.(21, 22) Another approach would be to have the biohybrid material respond to environmental cues that can be directly engineered. A number of studies have employed exercising the muscle during maturation through a series of mechanical

stretches or electrical stimulations and have shown >2-fold increase in force generation post-exercising regimens.(23–25)

In the present work, we expand upon our prior walker bio-robot (bio-bot) design by developing a new tissue fabrication protocol that increases the force per single actuator by generating longer myotubes and proposing a mathematical model to develop a predictive computer simulation based on empirically calculated force parameters characteristic to the biohybrid tissue (Figure 4-1). Our model is based on assemblies of Casserat rods, i.e. slender, soft and shearable elements.(26) By varying mechanical properties and by enabling contractile stresses, we can model both scaffold and living tissue as well as their dynamic interactions. Once calibrated with experimental data, we employed these simulations to effectively modify the tissue morphology and contractile characteristics of these biological machines to pointedly scale the force to a higher range than has been previously reported, in order to power the actuation centimeter-scale skeleton structure (2 times larger than prior design). Specifically, a larger number of single actuators was achieved by increasing the tissue volume while controlling tissue thickness to avoid limitations of nutrient-diffusion and a larger, stiffer scaffold was designed to maintain functionality of the bio-bot driven by a higher-force generating muscle tissue, as previous designs would collapse under the larger force. Finally, critical factors are further quantified to revise computational models. By implementing this new modeling approach, we could predict and validate designs, thus enhancing the efficiency of forward engineering these biohybrid systems and serve as new design tools to successfully develop the next generation of biohybrid robots from the ground up.

4.2 MATERIALS AND METHODS

4.2.1 SIMULATION AND MODELING

Muscles are considered as bundles of quasi one-dimensional filaments, which can have large deformations in multiple directions. To capture this physics, a numerical method(26) based on Cosserat rod theory(27) is implemented for the muscle simulation, which solves the dynamic and deformative problems of soft rods with large deflections. For the sake of modeling the entire system with one set of equations, same theory is leveraged for modeling the skeleton. Thus, in simulation, an assembly of one-dimensional rods with rectangular cross-sections constructs the skeleton, whose mechanical properties are essentially preserved. Detailed explanations are presented in Appendix 1.

Interactions within multiple filaments, and between filaments and environments are also included in the simulation. Repulsive forces are generated when the muscle is in contact with the pillars, eliminating all the interpenetrations. Formulations and implementations of the interaction schemes are also included in Appendix 1. Coulomb friction model is applied at the surface between the pillars and the ground, while hydrodynamic forces are applied to the entire body(26).

4.2.2 2D MYOBLAST CULTURE AND DIFFERENTIATION

C2C12 murine myoblasts were seeded at 0.3e6 cells/well in a cell culture six-well plate and cultured in muscle growth media (mGM) consisting of Dulbecco's Modified Eagle Medium with L-glutamine and sodium pyruvate (DMEM, Corning Cellgro) supplemented with 10% fetal bovine serum (Lonza), 1% L-glutamine and 1% penincillin-streptomycin (Cellgro Mediatech, Inc.). When cultures reached 80-90% confluency at approximately 2-3 days, media was switched

to muscle differentiation media (mDM). Differentiation media consisted of DMEM supplemented with 10% horse serum (Lonza), 1% L-glutamine and 1% penicillin-streptomycin. 2D differentiation was continued for 5 days, changing media daily. All cultures were kept in incubators at 37^{o}C and 5% CO_2.

4.2.3 FORMATION OF 3D SKELETAL MUSCLE TISSUE

The construction of myoblast formed (MB) skeletal muscle tissue followed previously published protocol.(6) In summary, each muscle ring was formed from a solution of 0.5e6 myoblasts mixed with 30% Matrigel (Corning), 4mg ml^{-1} fibrinogen (Sigma-Aldrich) and 1 U per mg$^{-1}_{Fibrinogen}$ of Thrombin (Sigma-Aldrich) and mGM was added for a total of 100uL of solution. Each cell-fibrin solution was dispensed to a PEGDA mold and permitted to compact for 3 days in mGM before being switched to mDM supplemented with 1X aminoproic acid (ACA, Sigma Aldrich).

Myotube formed (MT) skeletal muscle tissue rings were formed analogously to MB rings. Differentiated 2D myotubes were trypsinized with TrypLE and delicately triturated mechanically to achieve a single cell suspension without breaking the myotubes. Half the cell contents of a single well were used for a single MT ring by using the same ECM-Fibrin hydrogel composition used for MB rings.

4.2.4 DESIGN AND 3D PRINTING OF MOLD AND SKELETON STRUCTURES

Biobot ring molds and skeletons were 3D printed using a customized stereolithography apparatus (SLA 250/50, 3D Systems). Ring molds were fabricated using 20% w/v PEGDMA M.W. 1000 g mol^{-1} and skeletons were fabricated from 20% w/v PEGDA M.W. 700 g/mol. Both

solutions also contained 0.5% w/v of the photoinitiator Irgacure 2959 (Ciba). Fabricated parts were sterilized in 70% EtOH for 1 hour and then stored in PBS prior to use.

4.2.5 ELECTRIC STIMULATION

A waveform generator was used to depolarize muscle tissue by connecting to a AD797 inverting amplifier. Square pulses were converted into biphasic pulses by connecting a capacitor C in series turning the system into an RC circuit. This was done to avoid electrolysis of the cells. Two parallel platinum wires were held in place by a square acrylic well that could be fitted into the 6-well plates where the junction bots were places for measurement. Each wire was connected to the electrode contacts to run an electrical current perpendicular to the muscle from the cathode to the ground.

4.2.6 MEASUREMENT OF FORCE AND LOCOMOTION

Muscle actuation was recorded through a stereomicroscope (MZ FL III, Leica Microsystems) by using a digital microscope camera (Flex, SPOT Imaging Solutions) to image junction bots with pillars facing the camera at a frame rate of 6 f s^{-1}. The bending of the junction bot's beam was correlated to the pillar deflection in response to the contraction of the muscle. This displacement was measured in ImageJ (National Institutes of Health). Passive tension force was then calculated using the Euler-Bernoulli beam-bending theory:

$$P = k * \delta_{max}; for\ k = \frac{8EI}{L^2 l} \quad \text{(Equation 1)}$$

,where δ_{max} is the measured deflection displacement. The other constant values were calculated for the beam, where I is the moment of inertia, L is the longitudinal dimension and l is the moment arm from the point of applied force if the tissue to the beam. E represents the Young's

Modulus, which was previously measured to be 319 kPa, for the chosen fabrication parameters. Stimulated tension force was calculated with the same model, using the transient deflections displacements produced by the contractile force of the skeletal muscle tissue under electrical stimulation at varying frequencies.

4.2.7 IMMUNOFLUORESCENCE IMAGING

Prior to staining, muscle tissue was rinsed with PBS and fixed in 4% (v v^{-1}) of paraformaldehyde for 20 minutes on the skeleton structure to conserve the tissue structure during steady state. Samples were then washed with PBS three times and removed from the structure by cutting the PEGDA pillars. Triton-X was diluted to 0.25% (v v^{-1}) and used to permeabilize the tissue membrane for 20 minutes. After washing with PBS, samples were blocked and stored in 1% (w v^{-1}) bovine serum albumin (Sigma Aldrich) at 4 ^{o}C until ready to stain (no more than 2 weeks).

Cell membrane was immunolabeled with a 1:200 dilution of 488-conjugated antibody reactive to F-actin, by incubating overnight at 4 ^{o} C. The primary antibodies, mouse anti-myosin heavy chain (MF-20) and rabbit anti-α-actinin, were used to stain for myosin and the sarcomere respectively at a 1:500 dilution. Tissues were incubated with the primary antibodies for 12 hrs at 4 ^{o} C. Samples were then washed three times before staining with secondary antibodies. AlexaFluor-647 anti-mouse (ThermoFisher) and AlexaFluor-633 anti-rabbit (ThermoFisher) was used to stain MF-20 and α-actinin primary antibodies respectively and incubated for 2 hr at room temperature.

To be able to image 3D tissue without distorting the internal cellular structure, stained samples were fitted into a custom-made PDMS mold, embedded in 1% agarose and covered with

a coverslip to ensure the agarose surface would be even. These molds were plasma bonded to a microscope slide. For imaging, the slides were flipped with the agarose facing the objective for high resolution confocal imaging.

4.2.8 ALIGNMENT QUANTIFICATION

The orientation of myotubes was quantified using the Directionality plugin for ImageJ which uses Fourier component analysis, which computes a histogram which counts the amount of myotubes in a given direction, numbered as degrees.(28) Because myotubes show a preferred direction, the calculated histogram shows a singular peak at that orientation. A Gaussian fit is calculated from the highest peak.

Fluorescent imaging was used to visualize the myotube membranes on the junction stained with conjugated F-actin. Images were uploaded to ImageJ and cropped to include only the region of the muscle junction. Fourier power spectra was later computed using the Directionality plugin. All samples showed a goodness of fit above 0.9.

4.2.9 MYOGENIC MATURITY ASSAYS

Biobot muscle rings were rinsed in PBS, snap frozen in liquid nitrogen for 5 min, and stored at -80°C. To analyze muscle creatine kinase activity, samples were thawed at room temperature. The muscle tissue was broken up using a pair of micro-scissors, and 300 µL of RIPA buffer (Thermo Scientific) was added to the sample. Samples were vortexed, then rocked at 4°C for 30 min to break apart the tissue. Samples were then sonicated at a power of 1 Watt for approximately 10 seconds, or until no visible pieces of tissue remained. The samples were then centrifuged for 15 min at 14,000 G and 50 µL of supernatant was mixed with 1 mL of warm

creatine kinase working reagent, prepared according to the supplier's instructions (liquid creatine kinase reagent set, Pointe Scientific Inc). 100 µL of the mixture was then transferred to a 96 well plate, which was incubated at room temperature for 2 min. The plate was read at 340 nm, with seven readings taken at 1 min intervals at 37°C. MCK activity in U/L was calculated from the change in in absorbance with time.

4.2.10 VIABILITY ASSAY

The MTS assay working reagent was prepared by combining MTS solution (CellTiter 96 AQueous One Solution Cell Proliferation Assay, Promega) with warm DMEM (without phenol red) in a 1:5 ratio. Muscle rings were rinsed in PBS, placed in individual wells of a 24 well plate, and immersed in 360 µL of MTS working reagent. The reaction proceeded in the dark for 4 hours at 37°C. Absorbance at 490 nm was used to measure metabolic activity, and thus cell viability.

4.3 RESULTS

4.3.1 FORMATION OF BIOLOGICAL MACHINES THROUGH CRITICAL DESIGN PARAMETERS.

The design of the walker bio-bot consists of two pillars, or legs, connected by a beam. Differentiated muscle tissue is held between the two legs and as it contracts, it exerts force on these legs causing the flexible beam to bend. As the beam deforms, the tip of the pillars come close to each other and as the muscle relaxes so does the beam, returning the pillars to its original position. This muscle-pillar-beam design mimics the muscle-tendon-bone relationship found *in vivo.* The skeleton structure of the bio-bot is fabricated by using a modified stereolithography apparatus (SLA) to 3D print a poly (ethylene glycol) diacrylate (PEGDA) hydrogel from a

computer aided design tool. (Figure 4-2.a) The biohybrid tissue is then engineered by mixing a suspension of C2C12 mouse skeletal myoblasts with extra-cellular matrix (ECM) proteins fibrinogen and thrombin, and injecting the mixture into a 3D printed PEGDA mold, to allow for gelation (Figure 4-2.b). This results in cells engrafted in a web-like fibrin hydrogel (Figure 4-2.c).(29) The cell-laden gel subsequently compacts, and compaction is restricted by the stiff PEGDA mold, inducing tension across the fibrin gel, which serves as a mechanical cue to direct the aligned differentiation of myotubes. Differentiated muscle can then be electrically stimulated to contract cyclically, which elicits locomotion by a two-anchor gait.

Force production and functional output can be further engineered by visualizing the muscle tissue as a series of actuators (i.e. myotubes) bound together by an inert hydrogel, and addressing the geometrical parameters (Figure 4-2.d). The internal muscle contractile stresses may be modeled as:

$$\boldsymbol{F_{muscle} = n * F_{MT}(B) * sin(\theta_{avg}) = A_{tol} * \gamma * \sigma_{MT} * \sin(\theta_{avg})} \text{ (Equation 2)}$$

where F_{MT} and $\boldsymbol{\sigma_{MT}}$is the contractile force and stress of individual myotubes, $\boldsymbol{\theta_{avg}}$ is the mean angle of individual myotubes with respect to the lateral axis of skeleton actuation, $\boldsymbol{A_{tol}}$ is the cross sectional area and $\boldsymbol{\gamma}$ is the ratio of live actuatingto necrotic tissue. From this relation, the net force of the contracting tissue is a function of the force production of individual myotubes, which has been shown to be proportional to myotube length, B. (30) Thus, by increasing the number and length of myotubes, force can be linearly scaled up. This can be achieved by enlarging the tissue volume (*L*W*t*). However, there is a nutrient diffusion limitation of about 200μm from the tissue surface, which caps the practical *t* that can be designed before cell death occurs and a necrotic core forms impeding further force production. (31) Finally, Equation 1 implies that the net force for a given biohybrid muscle is maximized when all myotubes are

aligned parallel to the direction of actuation. Given this, the output force at the pillars can be also expressed as $F = k (\Delta x)$, where k is the stiffness constant of the scaffold against which the tissue is contracting, and Δx is the displacement of the scaffold pillars. Hence, if the tissue size and resulting myotube force is increased, the scaffold also must be redesigned to avoid collapse of the scaffold.

4.3.2 INCREASING FORCE PRODUCTION OF INDIVIDUAL MYOFIBER.

The first parameter that was targeted was the myotube length, as that would increase the force baseline for any subsequent design of any given biohybrid actuator. To increase the length of myotubes, we added a differentiation step in 2D prior to suspension of the cells in the 3D fibrin hydrogel as opposed to inducing differentiation of myoblasts (MB) in 3D fibrin hydrogel (Figure 4-3a). Substrate stiffness can profoundly affect myogenesis and longer myotubes can be obtained surfaces of higher stiffness.(32, 33) Stiffness of fibrin gels formed using a fibrinogen concentration of 4 mg mL^{-1} mixed with 1 unit $mg^{-1}_{fibrinogen}$ is typically <1 kPa, which is much softer than polystyrene plastic (~10^6 kPa).(34) Therefore, myoblasts were differentiated in 2D polystyrene for five days until elongated myotubes (MT) were observed (Figure 4-4a) and maturation markers were shown to plateau (Figure 4-5). Afterward, standard 3D seeding protocols were followed (See Materials and Methods section).

After engrafting myotubes in the 3D fibrin hydrogel, the bio-hybrid tissue showed no significant change in differentiation markers (Figure 4-6) indicating that bio-hybrid tissue development mainly consisted of myotube alignment and remodeling of extracellular matrix. After 2-weeks of maturation, MT tissue showed analogous structural characteristics comparted to MB tissue (Figure 4-4b; Figure 4-7). However, within the muscle, individual myotubes showed a

1.5-fold increase in length for MT samples (Figure 4-4.c; Figure 4-3b) indicating a higher degree of myogenic differentiation, which is corroborated by a significant increase in fusion index (FI) and concentration of the muscle creatine kinase (MCK) (Figure 4-3c,d).(35) It is important to note that there was no significant change in viability (MTS) between MT and MB tissue, indicating that changes in differentiation markers were not caused by increased cell numbers (Figure 4-3e).

The resulting forces were then compared between the MB and MT tissue, by installing them into the untethered 3D PEGDA skeletons (Figure 4-2b, Figure 4-4b). The force in these two constructs was correlated to the beam deflection using the Bernoulli-Euler model. After muscle maturation, the muscle develops a passive tension, which deflects the beam by a certain length. During electrical stimulation at constant frequency, both MB and MT bots showed cyclic contractions corresponding with the stimulation frequencies (Figure 3.d; Figure S1.f). Moreover, MT bots showed a substantial force increase when electrically stimulated. The force elicited per stroke from the MB bots was consistent in magnitude to previously reported constructs. (25) Contrastingly, the MT muscle tissue showed a 3-fold increase in force per stroke across different stimulation frequencies (Figure 4-4e). This indicated that the a priori differentiation of cells before they are integrated into the matrix results in increased myotube length leading to higher forces per stroke as expected.

4.3.3 ROD-BASED SIMULATIONS FOR DESIGN OF NEXT GENERATION BIOLOGICAL MACHINES.

In order to design a larger and stronger bot in a targeted fashion, we needed to optimize around both the biological and mechanical constraints. Aiming to effectively actuate on a skeleton structure 2X larger than previously reported walkers, a muscle structure capable of applying millinewton level forces was required.(19) This required a larger muscle structure. One of the limitations of designing biological tissue with a larger geometric latitude is that the nutrient and waste diffusion will be hampered past the limit of about 200 μm.(36) This will cause a necrotic core to form for cells farther than the diffusion distance, resulting in scar tissue and impeding the actuation and increase of force (Figure 4-2d). To overcome this, a mold was fabricated with a new design which was an integration of our prior muscle 'strip' and muscle 'ring' bio-bot design model (Figure 4-8a) (6). This new design can be implemented for larger planar geometries, while avoiding the necrotic core by controlling the thickness of the actuating tissue and maintaining the modularity of the process to increase the design window. Following the MT tissue differentiation protocol explained in Figure 4-4, myotube/ECM solution was dispensed on a mold with a shallow trench enabling the formation of a thin tissue region. This 400 μm deep trench would ensure that compacted tissue thickness was below the nutrient diffusion limit from either side.

This design was guided by the mechanical model of the muscle tissue, which was incorporated in a novel rod-based formalism for the simulation of arbitrary musculoskeletal structure .(37) (Appendix 1) The simulation approach aimed to model both the skeleton of the bot and the muscle tissues, with the capacity of capturing the dynamic responses during beam deformation and muscle contraction. Assembling of the junction bot for simulation purposes

consists in setting the force generation model of the skeletal muscle tissue (Figure 4-8b). Aiming to design bio-hybrid robots with arbitrary muscle arrangement and the structure of the skeleton, a general relationship was expanded from Equation 1 between the stimulated muscular stress $\boldsymbol{\sigma_{muscle} = F_{muscle}/A_{tol}}$ and force output to 3D scaffolds $\boldsymbol{F_{out}}$, where $\boldsymbol{A_{tol}}$ is the overall cross-sectional area of the muscle. A force model was thus proposed which involved, the ratio of the area of active muscle cells $\boldsymbol{\gamma = A_{act}/A_{tol}}$, and the average myotube alignment angle $\boldsymbol{\theta_{avg}}$. The relationship was defined as

$$F_{out} = A_{tol}\left(\gamma\sigma_{muscle} - \frac{\frac{E_{muscle}\varepsilon}{1-\varepsilon}}{}\right) \quad \text{(Equation 3)}$$

where E_{muscle} is the muscular Young's Modulus and ε denotes the strain of the muscle tissue. The latter term conveys the axial rigidity and the radial deformative behavior of the muscle. Furthermore, the overall stress is comprised of the passive and active elements, formulated as $\sigma_{muscle} = \sigma_{pas} + \sigma_{act}$.

In order to design a larger bot, or more general biohybrid bot with arbitrary configuration, σ_{muscle} has to be defined as the functional input. Here, σ_{muscle} is derived based on the force characterization of the MT bot, which has been demonstrated to have the desired force increase ($F_{out} = 2.6mN$). Thus, following Equation 2 and given the geometrical parameters ($A_{tol} = 1.08mm^2, \gamma = 0.83, \theta_{avg} \approx 90°$), we have σ_{muscle}=$10.39mN/mm^2$. For the muscle arrangement of the new bot design, the same muscle stress is proposed to apply since the same protocol is leveraged. It is also worth noticing that because of the thickness-controlled design, $\gamma \approx 1$. Therefore, from the muscle model, a muscle tissue with cross-sectional area around $1mm^2$ is expected to elicit forces F_{muscle}>$10mN$.

A complementary skeleton structure was also computationally designed to handle these levels of force and be capable of locomotion. The elastic modulus E of the PEGDA beam (See

Materials and Methods section, Equation 3) was kept the same (319.4 kPa) as the small skeletons for ease of fabricaiton. However, in order to accommodate the expected increase in force, the stiffness constant was increased by increasing the moment of inertia by ~ 5X (small skeleton: 0.04 mm^4; large skeleton: 0.2 mm^4) by increasing the beam dimensions accordingly to also be suitable for the designed tissue (Figure 4-9). By assembling the muscle tissue with the skeleton in simulation, the final configuration of the bot is shown in Figure 4-8b, with the passive muscle stress overcoming the intrinsic bending stiffness of the skeleton. The simulation result reveals a $1.4mN$ active force being applied on each pillar upon muscle stimulation, rendering a successful steady walking of the new bot. The details of the simulation results are presented later with the experimental characterizations.

These calculations permitted the fabrication of a centimeter-scale asymmetric skeleton, unto which the designed muscle structure could be modularly installed (Figure 4-8c). Due to the formation of a thickness-controlled muscle region bridging the tissues that wrap around the pillars, this tissue structure was labeled “junction bot”, and for ease of discussion will be referred to as such (Figure 4-8d, Figure 4-10).

4.3.4 EMPIRICAL CHARACTERIZATION OF THE JUNCTION BOT.

Once the junction bot design was successfully manufactured (Figure.4-8), it was confirmed that it could effectively elicit a macroscale deflection of the pillars when stimulated. The samples were electrically stimulated at multiple frequencies at 5, 10 and 15 days (5D, 10D and 15D) after seeding (Figure 4-11a). As expected, 5D samples showed contraction force below 3% of the total force (active + passive) calculated from the beam deflection. However, by 10D and more so at 15D, contraction force increased to 7.5% and 12.5% of the total achieved force. Passive tension

did not significantly change during maturation, averaging around 7.99±0.54 mN, 8.38±0.40 mN, and 8.45±0.86 mN for 5D, 10D, and 15D, respectively (Figure 4-11b). Passive tension is produced by the protein titin spanning across the half-sarcomere.(38) Therefore, the stable baseline in the passive force could be another indication that myotubes have reached steady state of differentiation prior to seeding. On the other hand, the active force per stroke increased significantly over time (Figure 4-11c). Rate of increase of active force from 10D to 15D was smaller compared to that from 5D to 10D, which could be interpreted as sign of plateauing of tissue maturation. At stimulation frequencies of 2 Hz and 4 Hz, junction bots were able to elicit stroke forces in the range of 1.10 ± 0.30 mN and 1.14 ± 0.25 mN, respectively, which are almost 6X higher than what was previously achieved for these skeletal muscle actuated walking bio bots.(19) Furthermore, similar to native tissue, this engineered skeletal muscle exhibited a positive force-frequency relationship, notable at 10D and 15D. (20) In addition, one standard deviation around the mean force per stroke at 15D coincided with the calculated force of 0.5 mN, 1mN, and 1.4 mN as compared to the stimulation frequencies of 0.5 Hz, 1 Hz and 2 Hz, respectively, and the resulting computed dynamic deflections of ~0.3mm, ~0.5mm, ~1mm, respectively (Figure 4-11d). This provided key confirmation that the muscle-scaffold model could serve as a predictive model for force output of engineered muscle tissue.

4.3.4.1 Empirical effects of geometrical parameters on force output.

Next, the junction geometry was examined as a parameter that could modulate force output. While dispensing myotube-ECM solution on the 3D molds, the solution entirely conformed to the mold dimensions followed by a compaction process as the fibrin hydrogel crosslinks (Figure 4-12a). To quantify the relation between junction dimensions and force production, molds with

trenches of initial seeding widths (W_o) of 3.5 mm ($W_{3.5}$), 7 mm (W_7) and 14mm (W_{14}) were used to dispense myotube-ECM solution and then tested at 15D (Figure 4-12b), at which final width had been reached (W_F). It was notable that the junction width did not compact linearly, relative to W_o (Figure 4-12c). The inter-quartile range (IQR) of the W_F for $W_{3.5}$ junctions was between 2mm and 3mm, which corresponds to a ~1.58-fold compaction ratio. However, for W_{14} junctions, the IQR spanned approximately 4 mm and 6 mm, corresponding to a compaction ratio of ~3.08-fold change. This relationship showed that the ratio by which these muscle junctions compacted was not constant (relative to W_0), but linearly correlated to the logarithm of W_0, with a slope of 0.75 (Figure 4-12c, top). This was in fact unexpected and could have occurred in response to nonlinear dynamics between muscle cells and fibrin hydrogels, and that could be intriguing to further study in the future.

Nevertheless, the resulting force was discernably affected by W (Figure 4-13). The passive tension significantly increased from 7.93 ± 0.3 mN for $W_{3.5}$, to 9.53 ± 0.68 mN for W_{14}, which constitutes on average a 1.2-fold increase (Figure 4-12d). This effect from W_0 was far more perceivable in the force per stroke evoked during stimulation. However, this stimulated force exhibited a significant decrease for larger W_0 (Figure 4-12e). While junctions seeded at $W_{3.5}$ reached forces during strokes of 0.97 ± 0.27 mN, junctions of W_7 were significantly weaker with stroke forces of 0.67 ± 0.26 mN. This trend was even more extensive for W_{14} junctions, reaching relatively weak forces of 0.47 ± 0.17 mN. This negative force per stroke dependence to W_0 was hypothesized to be a result of a lack of myotube alignment for wider junctions. It is well documented that cells align parallel to a hydrogel matrix under a uniaxial tension, by responding to both mechanical and topographical cues.(39, 40) Given that all the muscle tissues were subjected to the same tensile resistance by the skeleton beam, narrower junctions would result in

a more homogenous tension distribution and thus a more aligned cluster of myotubes, compared to wider junctions.(41) This would then result in more force per stroke during stimulation, as expressed in Equation 1.

4.3.4.2 Empirical effects of myotube alignment on force output.

To quantify this force-myotube alignment relationship, fluorescence microscopy was used to compare alignment of populations of myotubes within the muscle junction of samples to the evoked force response measured prior to fixing samples for imaging (Figure 4-14a). Fluorescent images stained for the cellular membranes in the muscle junction were analyzed by ImageJ, where myotubes were detected as single elements. By counting the elements at each degree between 0 to 180, normal histograms were obtained to quantify population mean (μ) and standard deviation (σ) (Figure 4-15). This was performed for junction bots at 5D, 10D and 15D (Figure 4-16). Distribution of myotube orientation evolved from an almost uniform distribution at 5D ($\sigma > 30$) to a normal distribution , plateauing by 15D ($\sigma \sim 15$), as cues from stiffer fibrin matrix fibers directed alignment (Figure 4-14b). Furthermore, during tissue maturation, the mean of the orientation distribution approached 90^{o}, aligned towards the direction of pillar actuation. To elucidate if there was a direct correlation between alignment and force production, the mean force per stroke was plotted against both the population mean, μ and the standard deviation, σ for three junction bots at 5D, 10D and 15D each. There were two possibilities. The first was that alignment played little role in general force production, but rather it was an effect of tissue maturation. The second was that either a net alignment of myotubes towards the direction of pillar actuation, or a homogenous alignment which minimized cancelation of force vectors from misaligned myotube components lead to a larger force production.

The produced force at different frequencies of stimulation did have, as expected, a positive relationship with μ, and a negative relationship with σ. However, there was no discernable trend with either. A positive linear relationship was observable when correlating force produced to the ratio of μ/σ (Figure 4-17), and within a same day of measurement, force values consistently showed a positive linear trend in relation to the ratio. Interestingly, regardless of the frequency of stimulation, the slope of the linear fits seemed to be consistent at around 0.15 ± 0.03 mN*$(\mu/\sigma)^{-1}$ (Figure 4-18).

Finally, force was also correlated with the alignment term of Equation 1 above at each day of the measurement (Figure 4-14c). As a physically relevant measurement of the influence of myotube alignment on actuation force, a normalized weighted average was defined as, $\overline{\boldsymbol{\chi_\theta}} = \sum_{\boldsymbol{i=0}}^{\boldsymbol{180}} \boldsymbol{\omega'_i} * \mathbf{sin}\ (\boldsymbol{\theta_i})$. Here, ω'_i is the value of the normalized magnitude component from the histograms for each respective degree of alignment in Figure 4-14b. These calculated values showed a very high linear relation with the measured force for each respective day, yet interestingly, also showed a clear dispersion for values across days. These empirical results confirm the relation between force and myotube alignment. This also seems to support our hypothesis regarding the effect of junction width to myotube alignment, with respect to force production as proposed in Figure 4-12 (Figure 4-18). Nevertheless, the dispersion for force with respect to $\overline{\boldsymbol{\chi_\theta}}$ across days of measurement would suggest that the model applies for a specific day of development as there might be other factors during tissue maturation that affect net contraction force. This is an opportunity for future work to fully elucidate such parameters for a model that accommodates time as a variable in the development of force.

4.3.5 PREDICTIVE MODEL FOR DYNAMICS FOR BIOLOGICAL MACHINES.

Another essential parameter to quantify during engineering of skeletal muscle-based biological machines is the dynamic functional output in response to the contraction force. Here, the skeletal muscle construct was fitted onto a PEGDA skeleton to achieve locomotion through a two-anchor gait. During stimulation, junction bots were placed with the pillars in contact with the substrate and tracked by a video camera as the cycling pillar displacement achieved net locomotion (Figure 4-19a). Similarly, by setting the pillars of the computational junction bot model in "contact" with a simulated surface with a roughness similar to polystyrene, two-anchor gait locomotion was also successfully simulated. Our simulation also demonstrates the dynamic variation of kinetic friction coefficients required for forward "inch-worm" locomotion (Figure 4-19b).(7) It is relevant to clarify that the simulated displacement was achieved by setting an input through the modeled tissue, and the skeleton would actuate as an output, thus resulting in an interaction with the simulated surface.

Both empirical and model-predicted position-time curves of junction bots depended strongly on stimulation frequency (Figure 4-19c), with the walking speed increasing with increasing stimulation frequency. While empirical results and model predictions matched well for 0.5 and 1Hz stimulation frequencies, agreement was poorer for 2 and 4Hz. This was not unexpected as simulating this slip-stick model of displacement is highly dependent on the initial state and, more importantly, the interplay between the forward and reverse friction coefficients of which the effects become more chaotic at higher frequencies. Therefore, we established that the high-accuracy of our computational model was limited to oscillation frequencies below 2 Hz (Figure 4-19b, c shaded area). On the other hand, it is worth pointing out that this larger and higher-force producing bio-bot design was able to reach speeds > 0.5 mm s^{-1} at 4 Hz (Figure 4-19d),

corresponding to a ~2-fold increase from previous designs.(6) This demonstrates the performance of these biological machines with respect to external stimuli as well as muscle geometry.

An analysis of work exercised on the pillars by the muscle tissue for junction bot showed no significant change between stimulation frequencies. However, when comparing with the work exercised during locomotion, which was defined as its efficiency, $\boldsymbol{\eta = \frac{Work\ during\ locomotion}{Work\ on\ Pillar}}$ (Figure 4-19d), there was a decrease from 0.71 ± 0.21 μJ μJ-1 at 0.5 Hz to 0.46 ± 0.02 μJ μJ^{-1} at 1 Hz, and then plateaued for higher stimulation frequencies. This implies that, even though stimulating at 4Hz can result in significantly higher speeds than at 0.5 Hz, the efficiency at 4Hz being only 0.52 ± 0.2 μJ μJ^{-1} implied higher slipping between the pillars and the substrate. This efficiency could be optimized by further treating pillar tips with surfactants or other fabrication processes to increase the friction coefficient. This would enable the engineering of biological machines to reach even higher speeds with decreased variability.

4.4 DISCUSSION

Tissue engineering has had a major focus of employing muscle cells as actuators capable of driving a large range of directed functionalities(42). Impressive breakthroughs have been achieved using self-contractile tissue, to engineer pumps and structures capable of locomotion. (1, 4, 5, 7, 43) However, the ability to modulate contractions for controlled outputs and functions has made engineering of skeletal muscle biohybrid actuators a central focus of the field (15, 19, 44, 45). Furthermore, skeletal muscle provides the possibility of engineering motor neuronal circuitry capable of controlling contractile output to a higher degree.

A critical part of advancing this field of study is to lay the foundation of principles that direct the engineering of next generation biological machines. To this purpose, the present work has developed a platform that links computational modeling to empirical validation for biological machines. This provides a proof of concept of the ability to start designing biohybrid actuators with more complex geometries and targeted force outputs which would result in the ability to engineer a wider range of function-specific performances. Here, we employed this concrete approach to intelligently increase the force output of autonomous biohybrid skeletal muscle biobots from ~200 μN to ~1.2 mN to actuate on a PEGDA scaffold that was twice as large as previous designs. By differentiating myoblasts on high stiffness substrates, versus 3D differentiation, their length was increased 1.5-fold and shown that these can still be effectively engrafted in a 3D construct without loss of viability. This length increase caused a force increase from each individual myotube actuator within the tissue, thus resulting in a net force increase from the entire structure. This length improvement could be further extended by differentiating myoblasts in groove-patterned substrates or the use of high-Connexin 43-expressing myoblasts.(46, 47)

Utilizing the computational model, we designed a fitting larger muscle structure by targeting and optimizing concrete design parameters while addressing the nutrient diffusion-based thickness limit by designing a new mold geometry. This increase of geometry of actuating muscle served to further increase the force, where the structures were enlarged from 6 mm (for its longest dimension) to 1.3 cm. It was further coupled with a walking skeleton structure designed to handle the scaled force. This work also aimed to characterize empirical factors in an effort to validate the proposed design criteria, primarily quantifying force to be correlated with the degree of alignment of the individual myotubes.

The resulting design could have the additional benefit of facilitating the introduction of other constructs, such as motor neuronal structures, by providing a physical platform on where to place such tissue. This is particularly advantageous since achieving adhesion in these types of suspended structures poses a real obstacle during modular approaches to multi-phenotypical tissue engineering.(48) Theoretically, a bundle of synthetic motor neuronal circuits that have been engineered to contain central pattern generators could be modularly placed on the junction for adherence, innervation and neuronal control of the structure.

We also developed a computational model that was able to simulate the dynamics of the muscle and its interaction with the skeleton. This model showed a high correlation with empirical force data, and, more importantly, effectively predicted the degree of the functional output, e.g. locomotion, with high accuracy. This could therefore be a great aid in the design of future biological machines that are able to exhibit more complex behaviors and achieve precise tasks with a high degree of control. Using this modeling approach, we can now computationally explore new skeleton designs that incorporate targeted modifications to critical structures and dimensions such as the beam thickness, pillar length, skeleton mass, etc., to acheieve a specific metrics of performance and functionality.

4.5 FIGURES

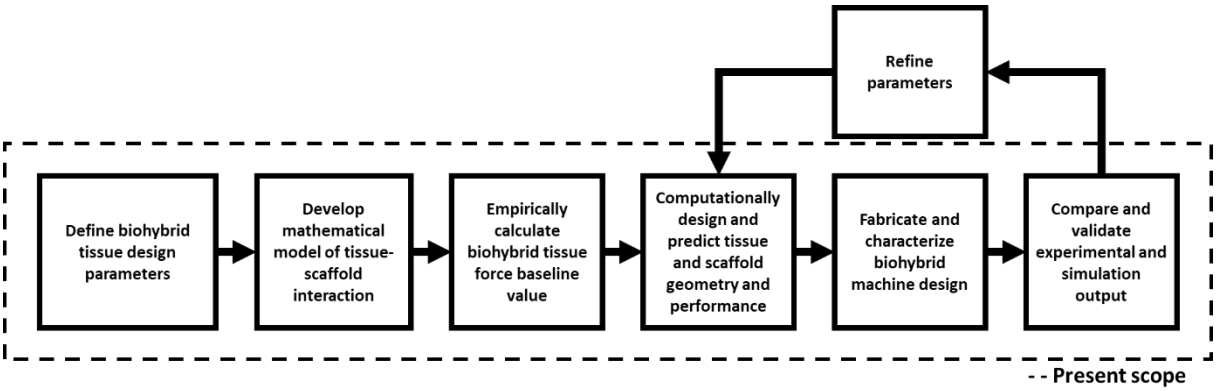

Figure 4-1. Process flow for the development of a computational predictive model for targeted forward engineering of biohybrid actuators

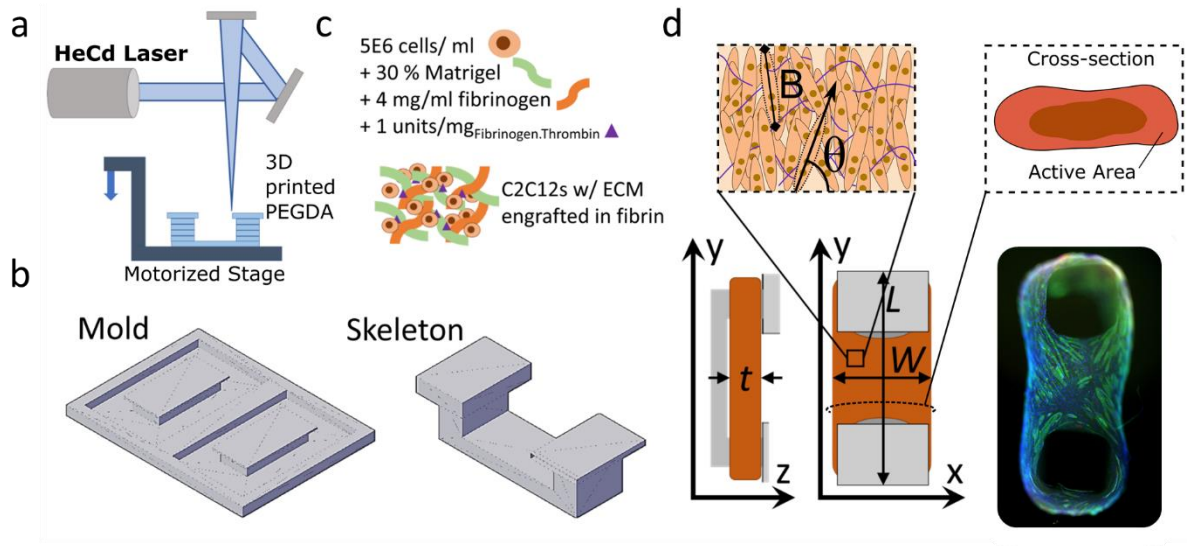

Figure 4-2. Design parameters of skeletal muscle biological machine. a) 3D sterelithography apparatus was used to 3D print PEGDA resin into the molding and skeleton structures (b) in order to guide the formation of muscle tissue and translate muscle contraction to locomotion, respectively. c) Biohybrid tissue is formed by mixing C2C12 myoblasts with ECM proteins. d) Forward engineering of muscle design for next generation biobots can be modeled as a function of muscle geometry of active tissue, and actuator length and alignment. (L: length, W: width, t: thickness, θ: myotube alignment, B: myotube length and active area).

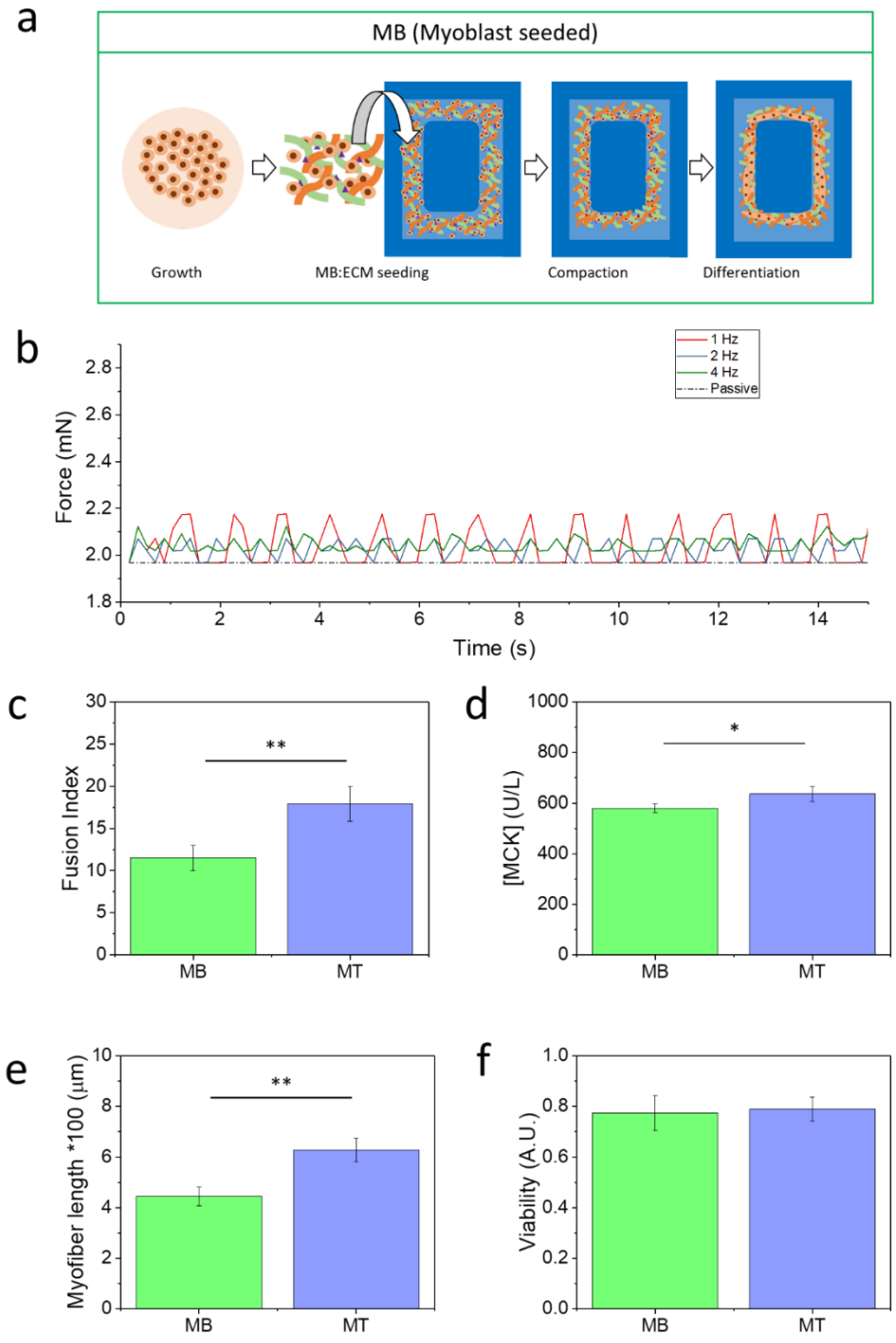

Figure 4-3. Myoblast a) (MB) formed biobot validation and comparison with myotube (MT) formed biobots. b) Viable MB bots showing response to multiple electrical stimulation frequencies, were compared against the MT bots in c) fusion index, d) muscle creatine kinase concentration, e) myotube length and f) tissue viability.

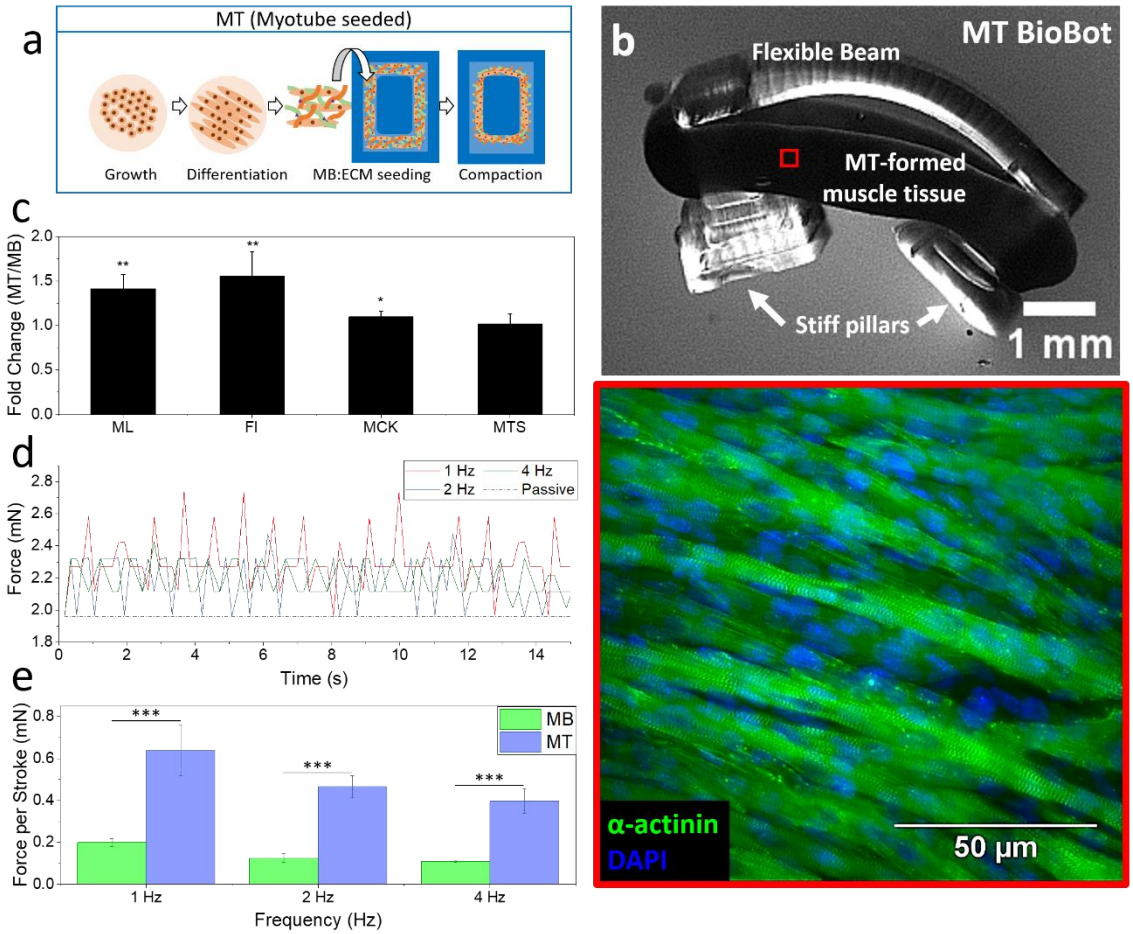

Figure 4-4. Increasing the force baseline by extending myotube length. a) Process flow diagram of muscle formation through seeding Myotubes (MT). b) Stereoscopic image an MT (b) bots exerting passive force on PEGDA skeleton (scale bar: 1mm). MT formed bio-bot consisting in striated bio-hybrid muscle in 3D. c) MT formed tissue was compared to myoblasts (MB) formed tissue through various parameters: (ML) myotube length (mean ± SD, n=20), (FI) fusion index – number of nuclei per multinucleated myotube— (mean ± SD, n=20), (MCK) muscle creatine kinase concentration (mean ± SD, n=4), and (MTS) cell viability (mean ± SD, n=4). d) Total force output of MT bio-bot for different frequencies of stimulation (0.5 Hz, 1 Hz, 2 Hz and 4 Hz). e) Force per stroke at different stimulation frequencies (mean ± SD, n=6) (*p<0.05, **p<0.005, ***p<0.0005, T-test)

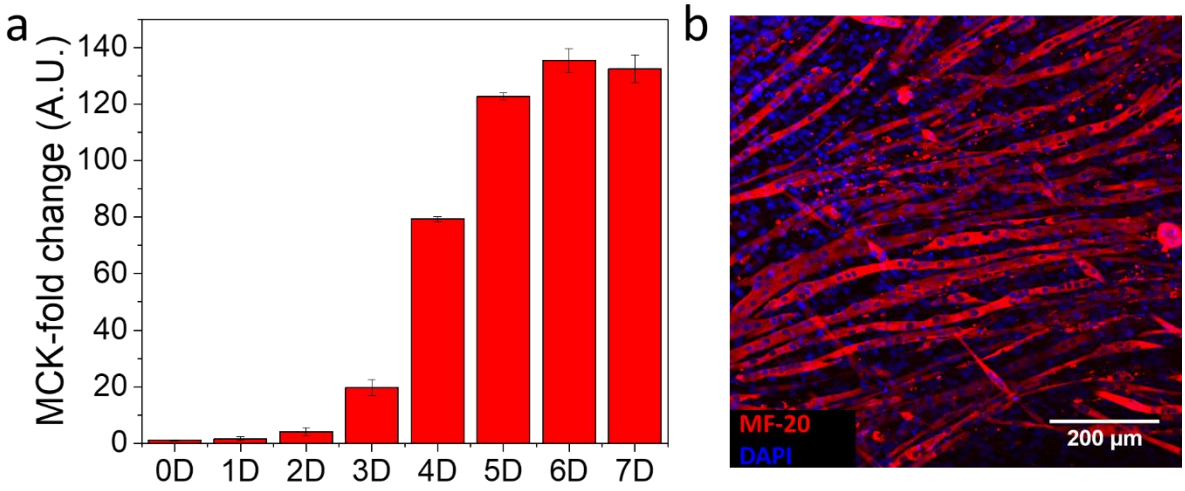

Figure 4-5. Muscle creatine kinase increase (left) during 2D differentiation (right)

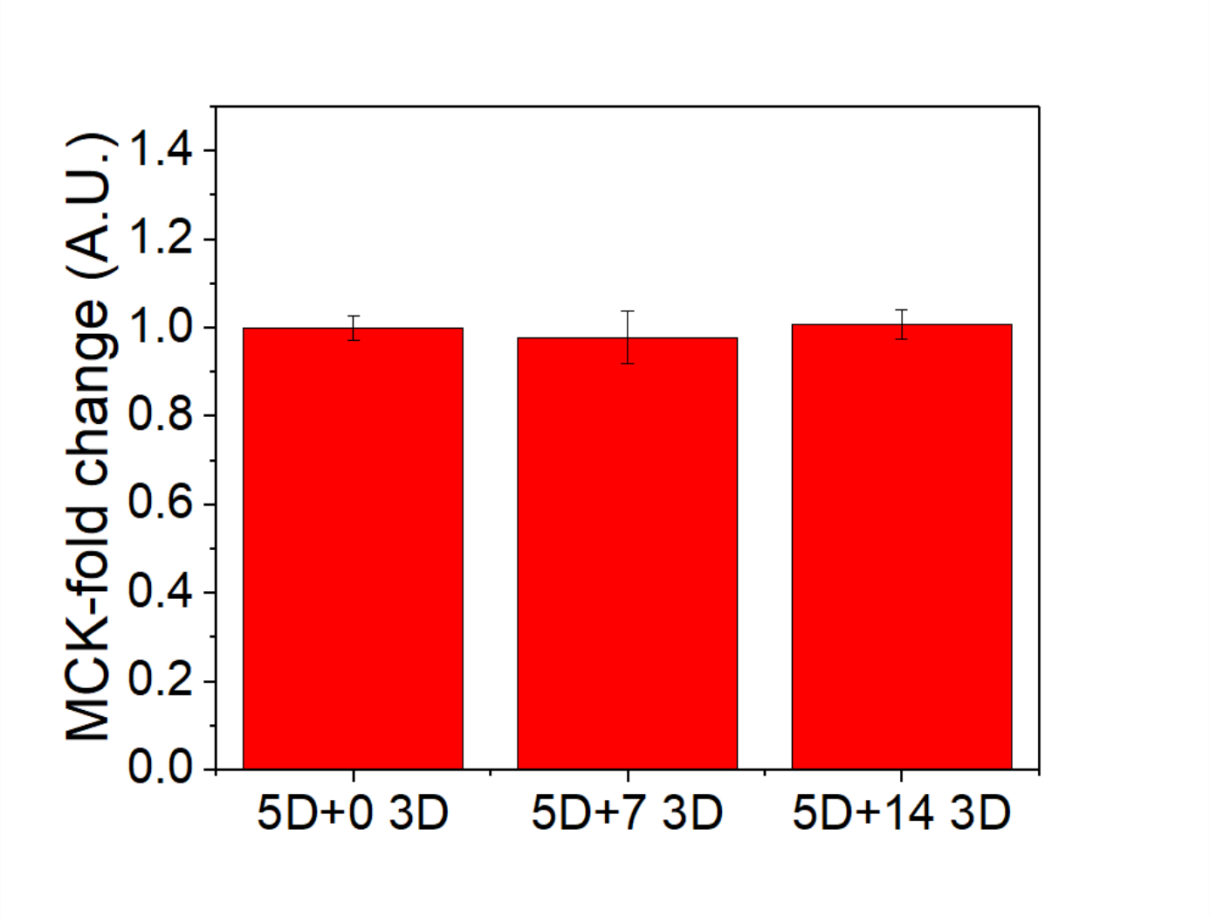

Figure 4-6. Concentration of muscle creatine kinase for MT formed muscle strips at 0, 7 and 14 days after seeding in the 3D mold.

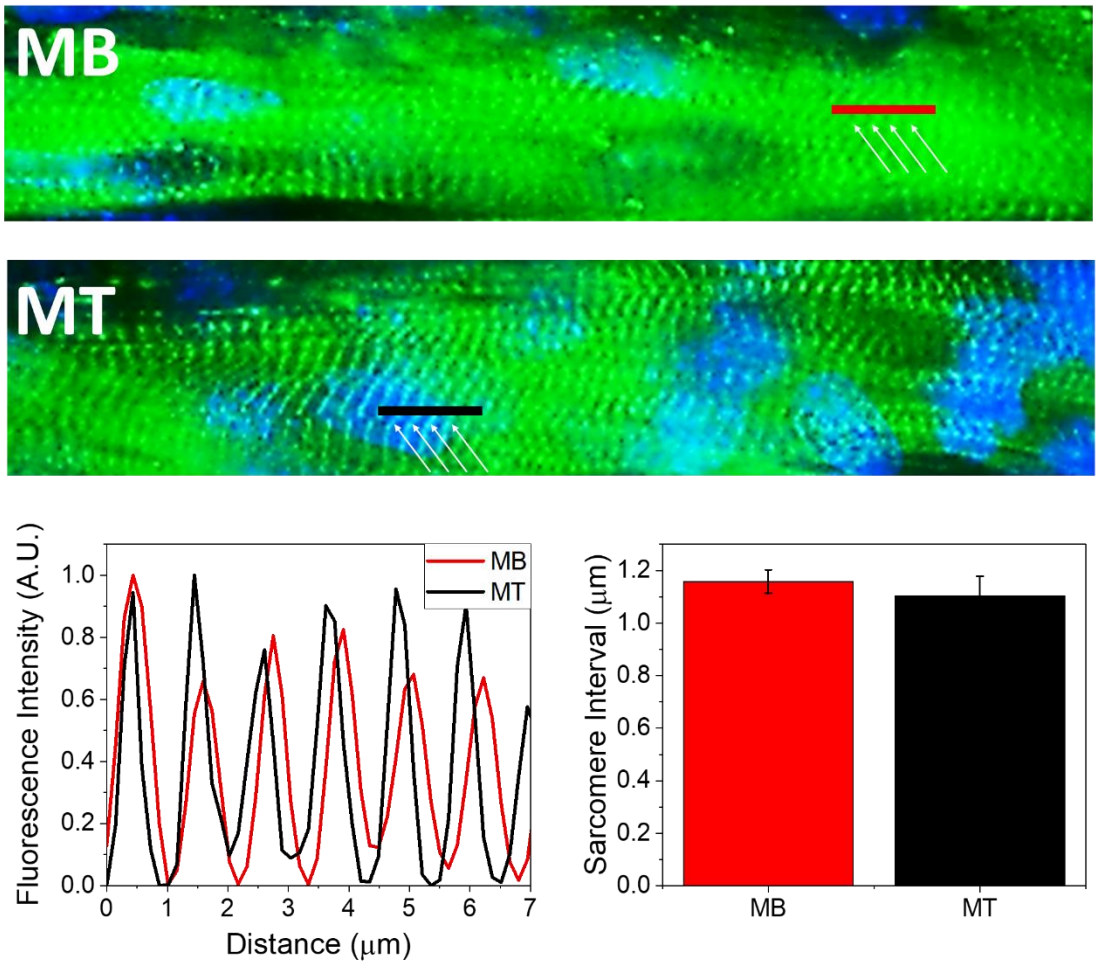

Figure 4-7. Myotube striation for MB and MT bio-bots showed no change in the interval between sarcomere bands.

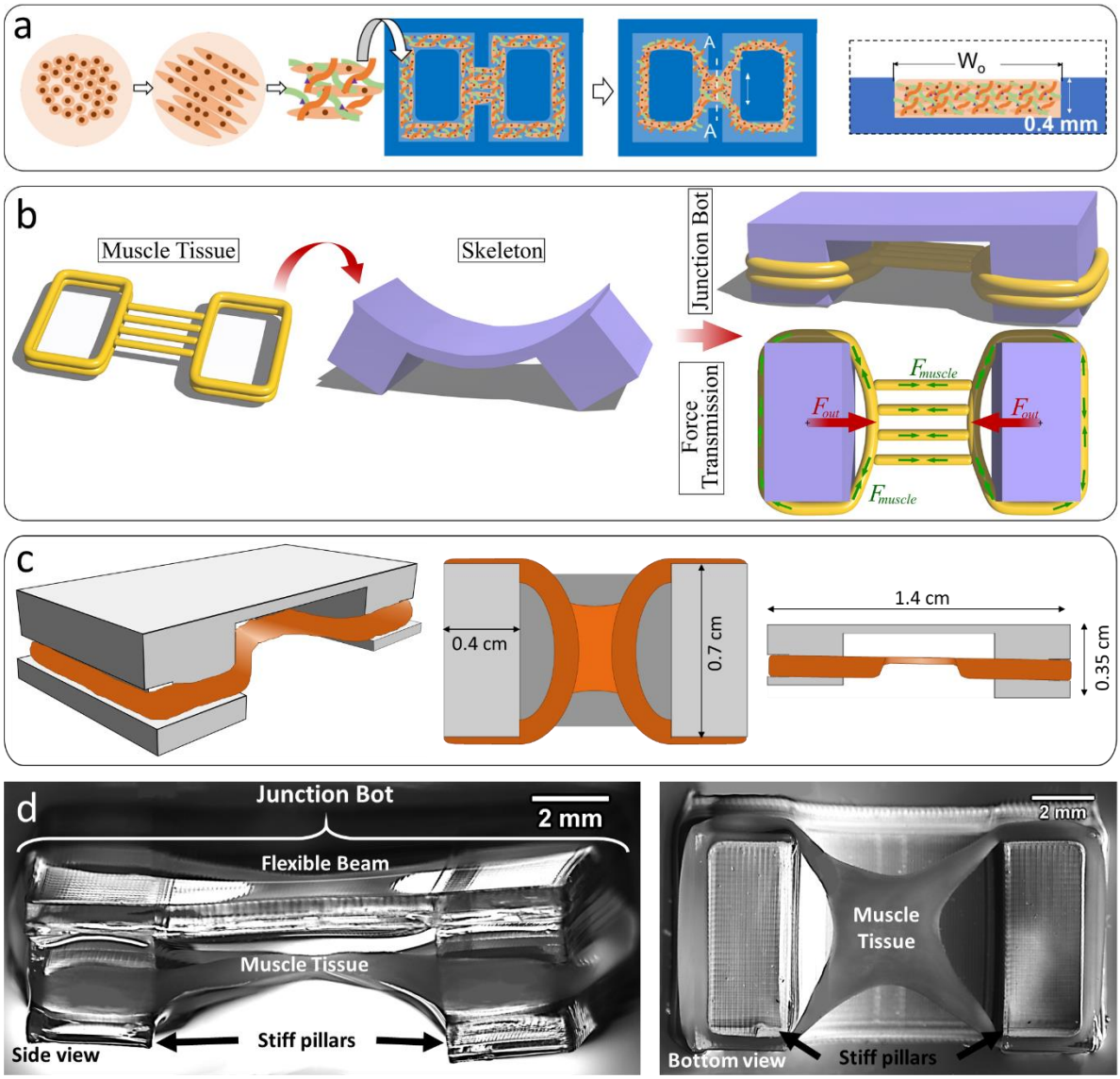

Figure 4-8. Formation of Junction Bot guided by rod-based simulations. a) Process flow diagram of myotube/gel solution seeding and tissue formation across a trench mold. b) Computational integration of muscle to designed skeleton to model the junction bot and study force transmission of the computational model. c) Representation of muscle tissue integrated onto a 3D printed PEGDA centimeter-scale skeleton (skeletons drawn to scale). d) (left) optical image angled side view of the entire junction biobot structure, (right) Phase contrast image of mature junction biobot from the bottom side showing the muscle and the printed hydrogel scaffold.

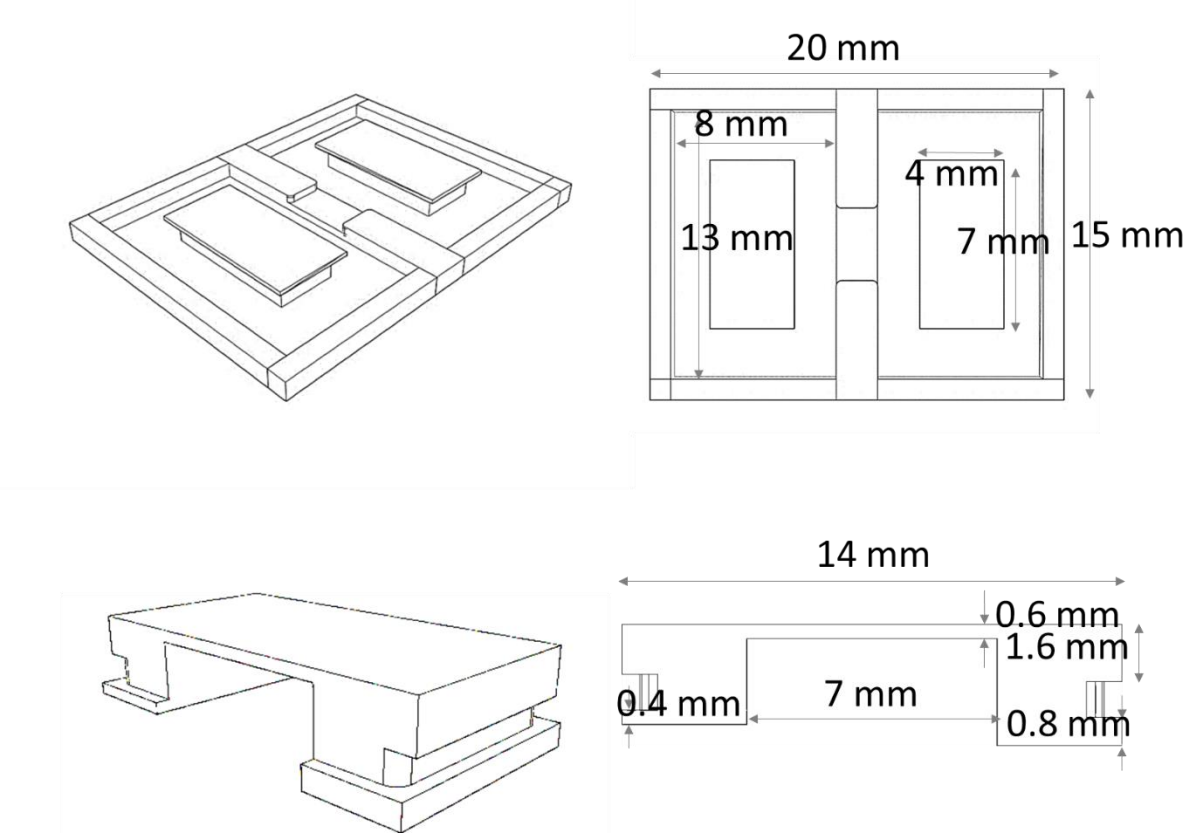

Figure 4-9. Dimensions of the mold and skeleton to form the junction bot

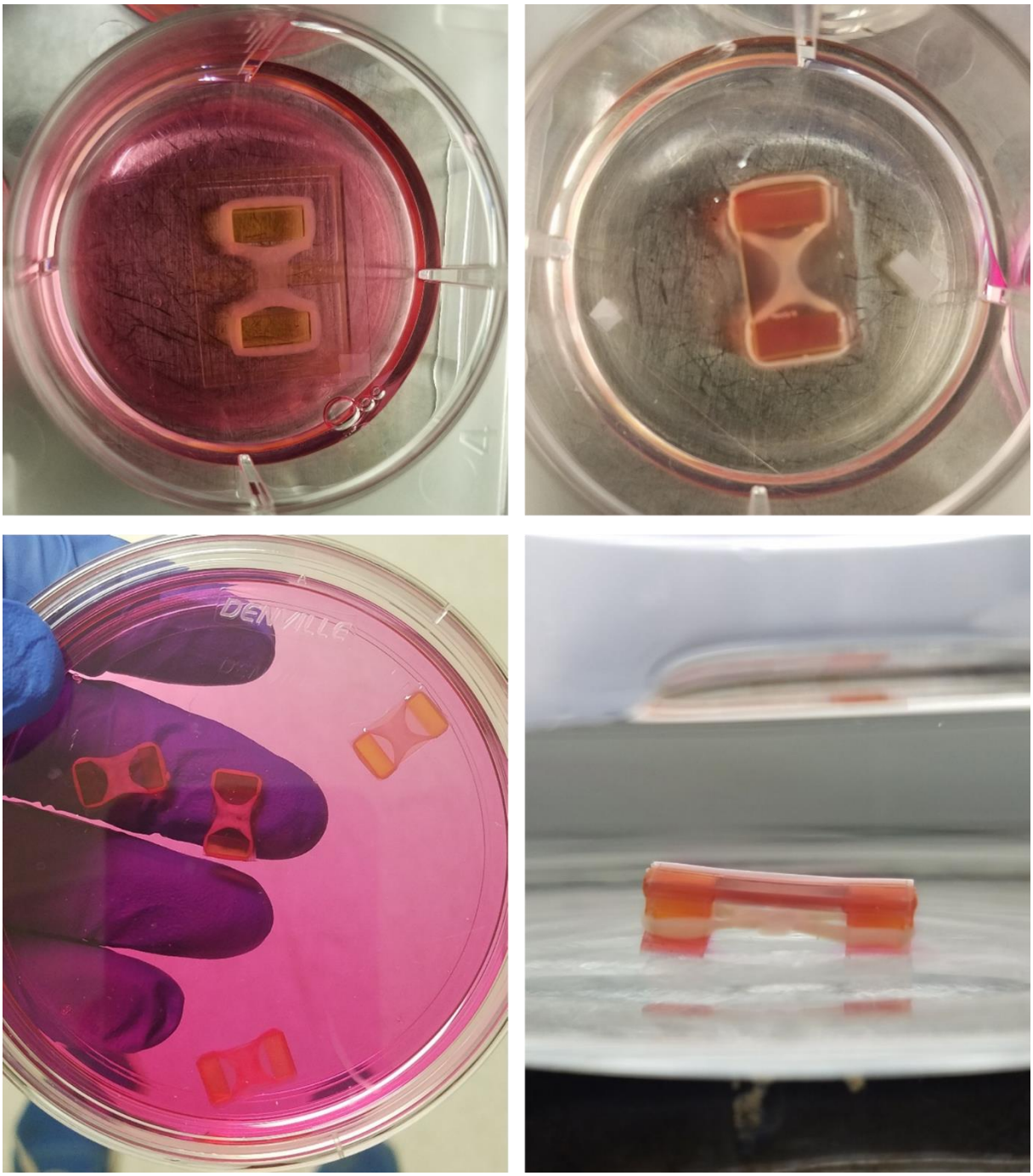

Figure 4-10. Representative photographs of Junction Bot.

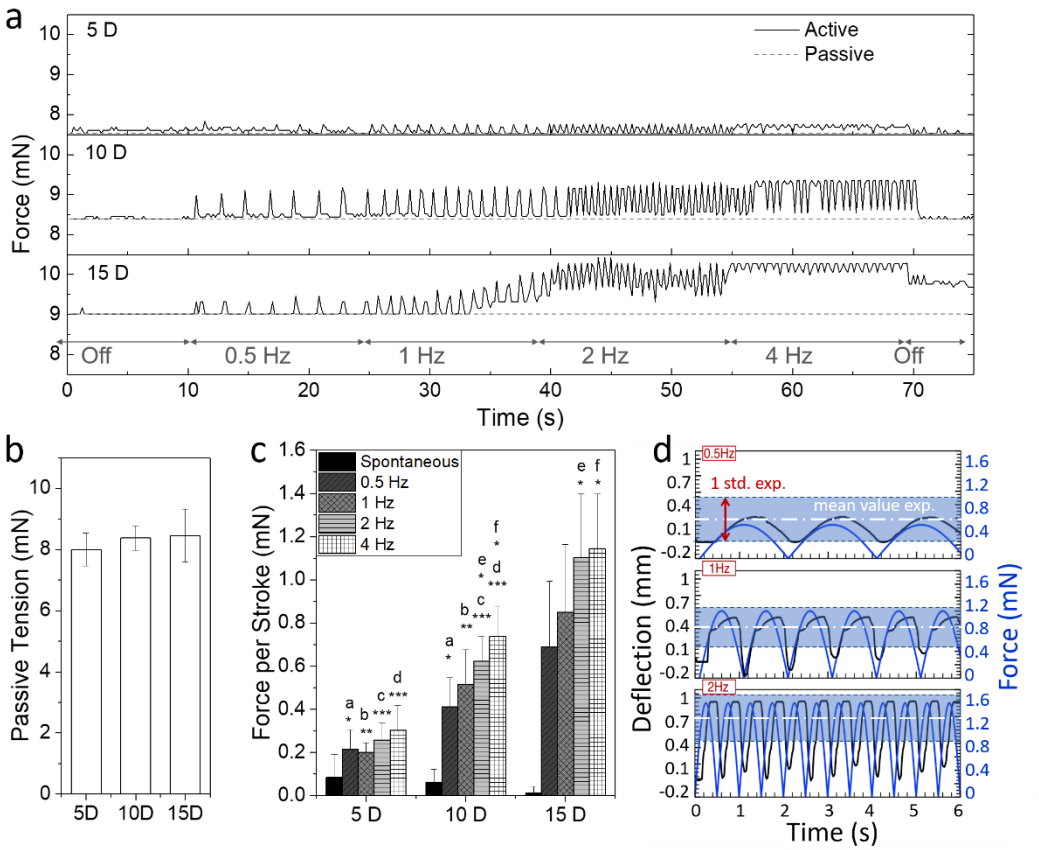

Figure 4-11. Force development of Junction Bot. a) Representative force (mN) response of muscle successively stimulated with an electrical field at increasing frequencies (0.5, 1, 2, 4 Hz) at 5 days (top), 10 days (middle) and 15 days (bottom) after seeding. b) Passive force at 5, 10 and 15 days of seeding. (mean ± SD, n=6). c) Force response at different frequencies of stimulation for each day of stimulation (5, 10 and 15 days) (mean ± SD, n=6). d) Computationally calculated deflection of pillars (black) and resulting force (blue) simulated for 0.5 Hz, 1 Hz and 2 Hz as predicted by the model, and falling within the 1 standard deviation of the empirical force of our bots at 15 D under respective frequencies of stimulation. . (*p<0.05; **p<0.005; ***p<0.0005, T-test).

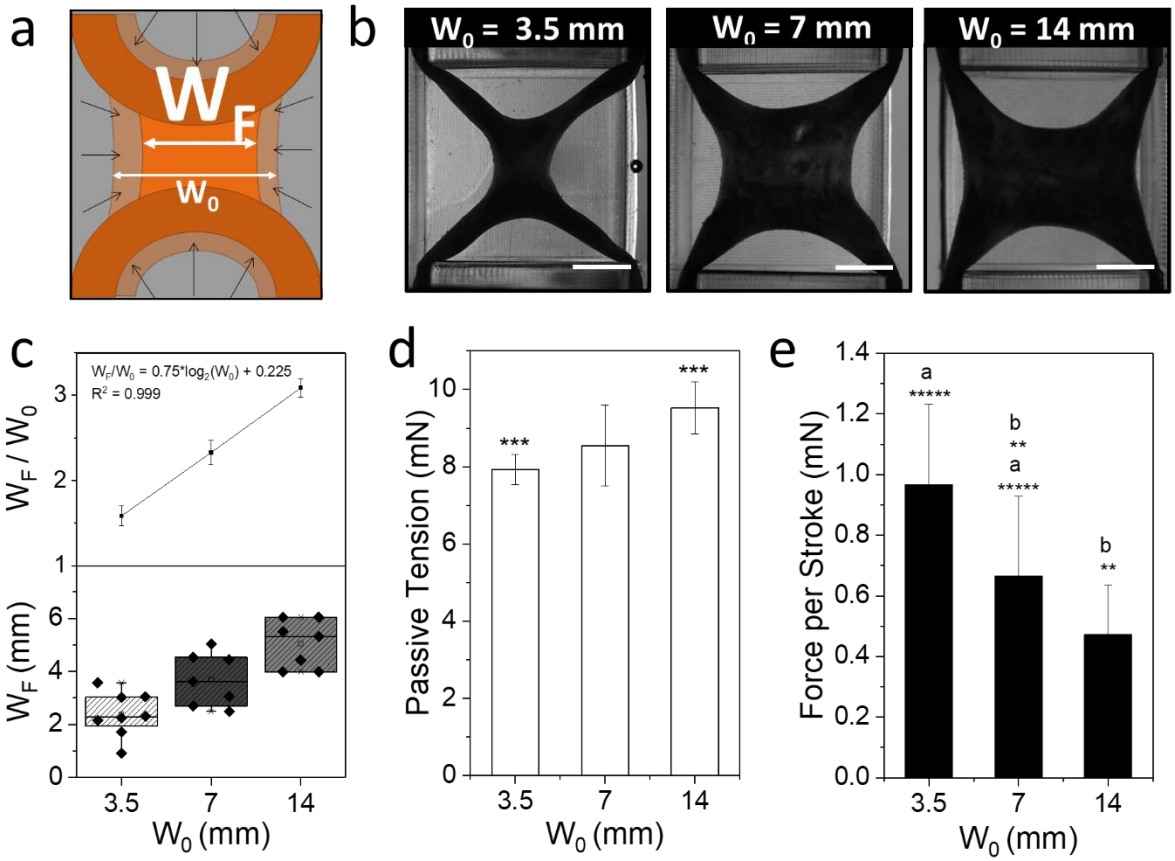

Figure 4-12. Force dependence to junction width. a) Representative image of the compaction process. b) Muscle after compaction from junction bots seeded on molds with varying trench width: 3.5mm (top), 7mm (middle) and 14mm (bottom) (Scale bar 2 mm). c) Compaction of biohybrid muscle, quantified by compaction ratio (W_F/W_0) (Top; mean ± SD, n=6) and final width (W_F) (Bottom) relative to the seeding width (W_0) (Bottom; Box plots range: 25/75 percentiles; n=6). d) Passive force (mN) of mature junction bots (mean ± SD, n=6) e) Average active force peak from mature bots at varying seeding trench widths. (mean ± SD, n=6). (**p<0.005; ***p<0.0005, T-test)

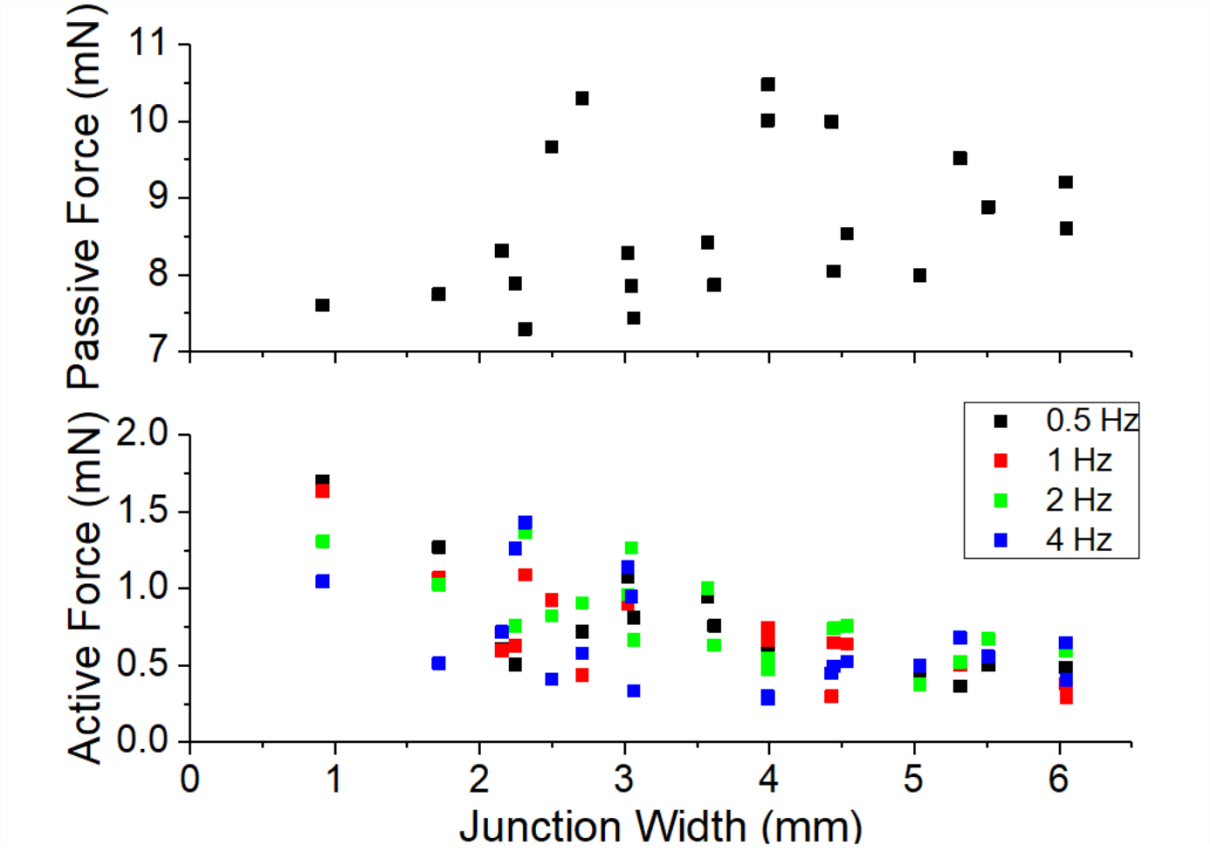

Figure 4-13. Force output of individual junction bots as a function of their respective final junction width.

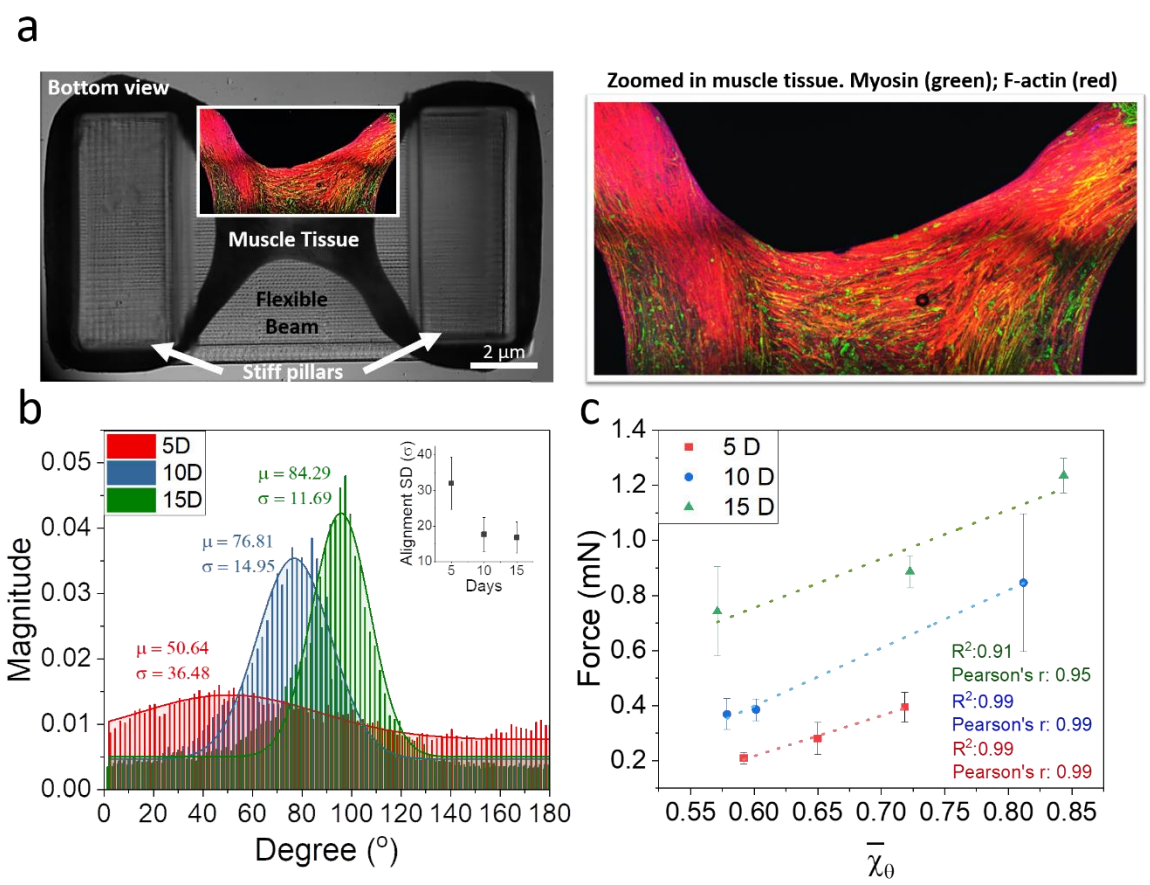

Figure 4-14. Force dependence to myotube alignment. a) Mature (15 D) junction bot showing myotube distribution and alignment through confocal microscopy. b) Representative histogram of magnitude of Fourier components versus degree of alignment for the myotubes at different days of maturation. The change of the dispersion of orientation of the myotubes was quantified with the standard deviation across the 5, 10 and 15 days. (Inlet; mean ± SD, n=3). c) Mean force produced per sample (mean ± SD, n=4) plotted against the degree score (angle of alignment (µ) divided by the standard deviation (σ)). Data points were linearly fitted ($P<0.01$, one-way ANOVA).

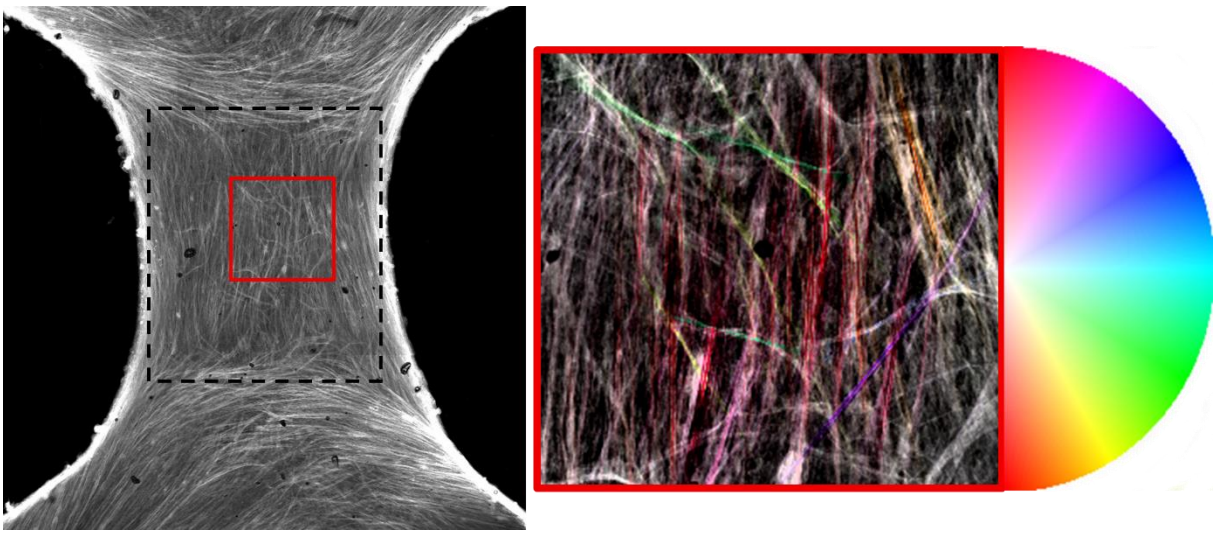

Figure 4-15. Representation of myotube alignment quantification.

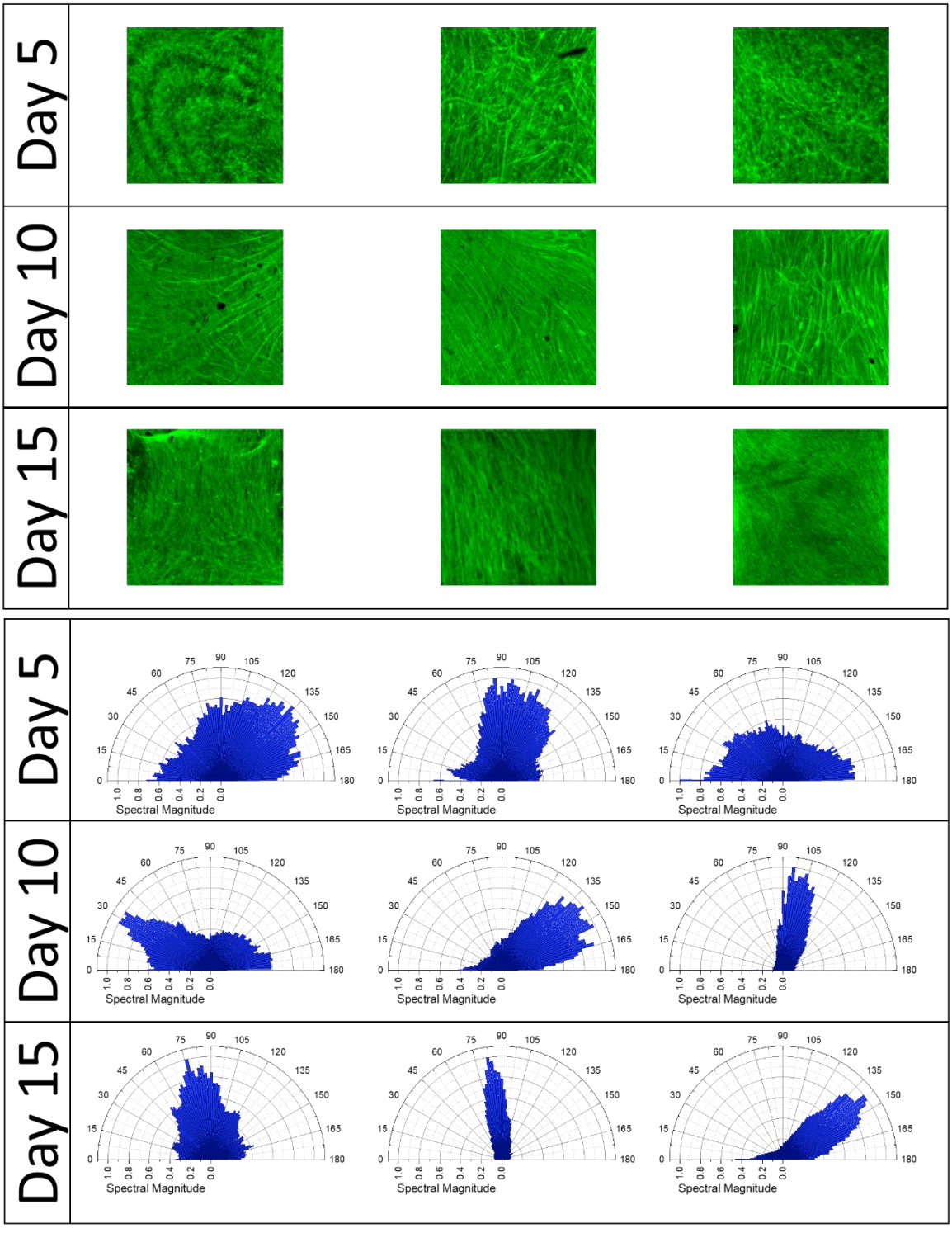

Figure 4-16. Polar histograms of myotube alignment.

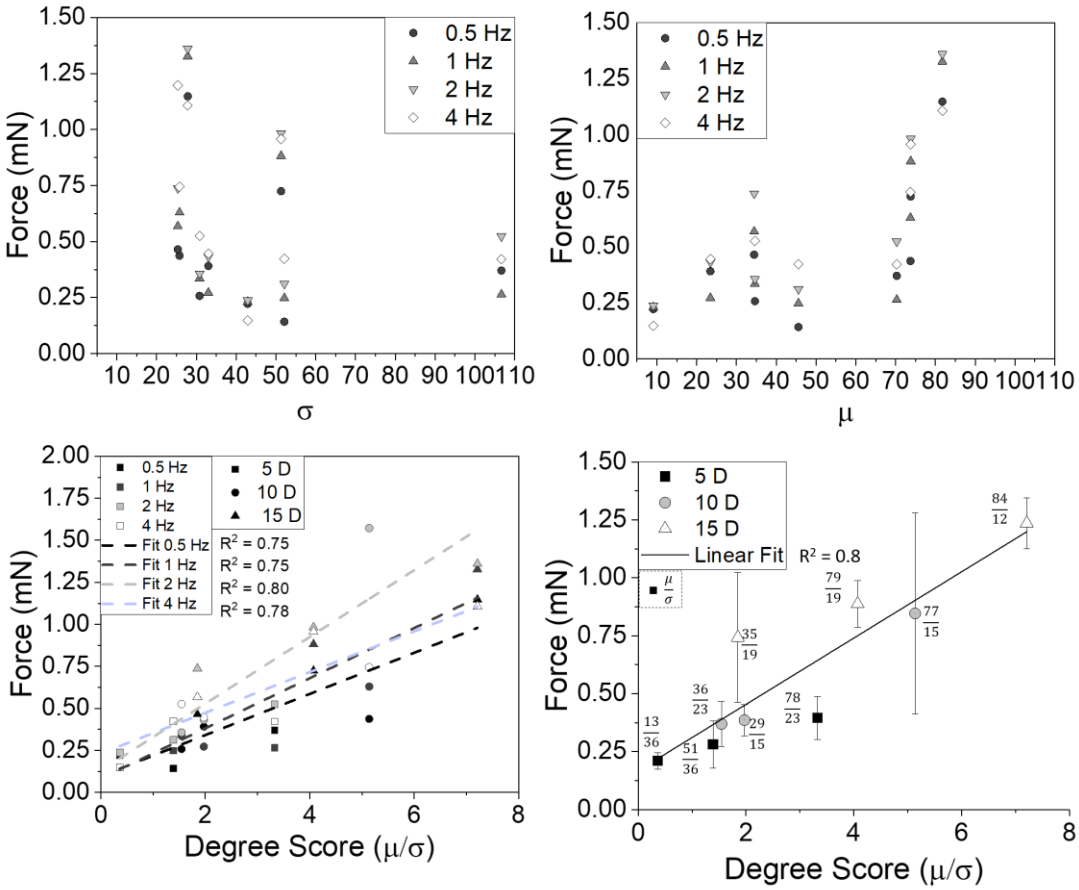

Figure 4-17. Junction bot correlation of force to standard deviation (σ) (top, left) and population mean (μ) (top, right) for individual stimulation frequencies. Junction bot correlation of force for individual stimulation frequencies (bottom, left) and the average force (bottom, right) to degree score (μ/θ).

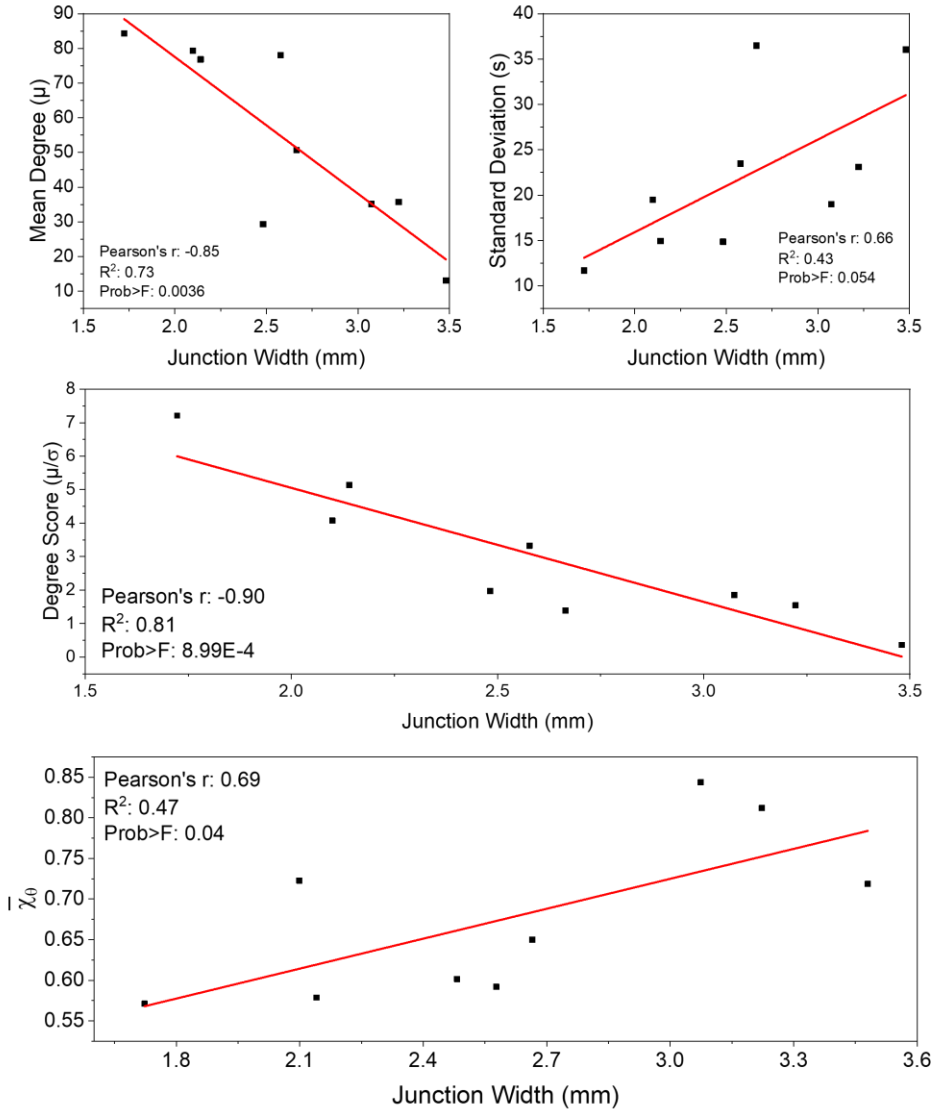

Figure 4-18. Correlation of junction width of bots to alignment parameters: orientation mean (μ) of myotubes, standard deviation (θ) of myotubes orientations, the degree score parameter defined as (μ/θ) and the normalized weighted mean of the sines of the myotube alignments (χ_θ).

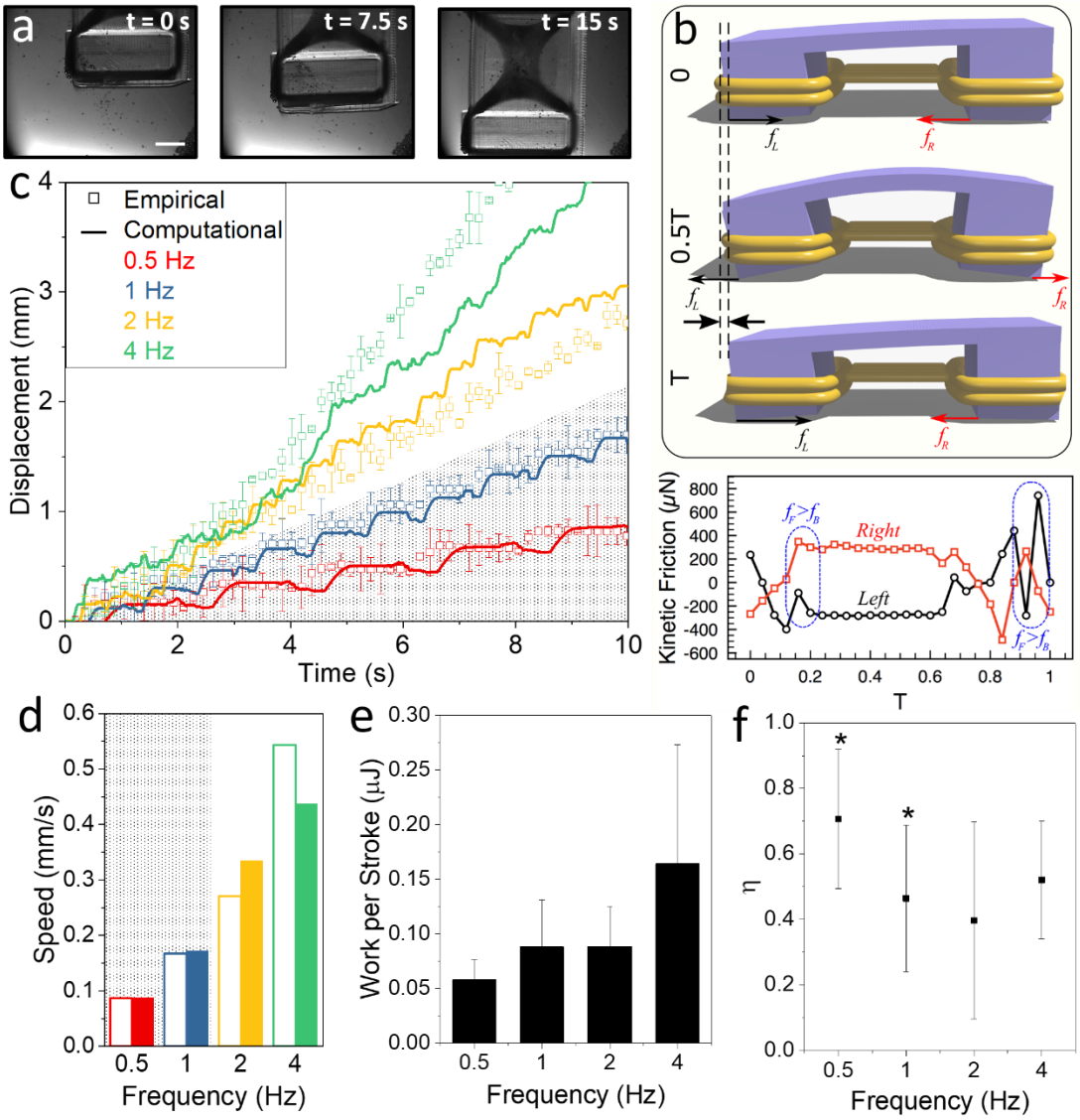

Figure 4-19. Functional output of junction bot. a) Snapshots of junction bot locomotion (scale bar: 2mm). b) Simulated gait for one period of junction bot displacement by a two-anchor mechanism of locomotion (top). The kinetic friction force change for each leg with respect to the period (bottom). c) Displacement versus time for different stimulation frequencies (0.5, 1, 2 and 4 Hz). Points are experimental data and solid lines are modeled junction bots at same frequencies of stimulation. d) Speed of displacement between experimental (clear bars) and computational (solid) results for different frequencies of stimulation. e) Work per stroke calculated from bot displacement multiplied by the force measured for that respective junction bot at the corresponding stimulation frequency. (mean ± SD, n=3) f) Efficiency (η) plotted against each stimulation frequency (mean ± SD, n=3). Efficiency was defined as $\eta = \frac{Work\ during\ locomotion}{Work\ on\ Pillar}$. (*p<0.05)

4.6 COSSERAT ROD THEORY

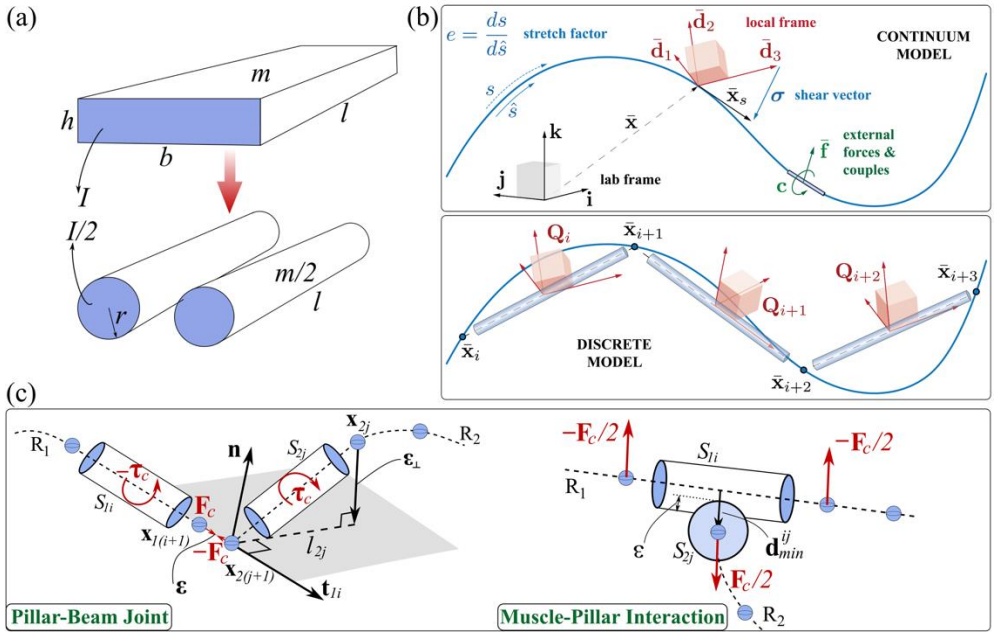

Figure 4-20. Junction bot correlation of force to standard deviation (σ) and population mean (μ) for individual stimulation frequencies.

Converting Beams into Rods Considering a beam shown in Figure 4-20a with length l, width b and thickness h, the mechanically equivalent conversion to two rods requires the matching of the bending stiffness and the total mass. Thus, the radius r and density ρ_r of each rod are given as

$$r = \sqrt[4]{\frac{bh^3}{3\pi}} \qquad \text{(Equation 4)}$$

$$\rho_r = \frac{bh\rho}{\pi r^2} \qquad \text{(Equation 5)}$$

where ρ is the original density of the skeleton.

Cosserat Theory We describe a rod by a centerline $\bar{\mathbf{x}}(s,t) \in \mathbb{R}^3$ and rotation matrix $\mathbf{Q}(s,t) \in \{\bar{\mathbf{d}}_1, \bar{\mathbf{d}}_2, \bar{\mathbf{d}}_3\}^{-1}$ which leads to a general relation between frames for any vector $\mathbf{v}$: $\mathbf{v} = \mathbf{Q}\bar{\mathbf{v}}$, $\bar{\mathbf{v}} = \mathbf{Q}^T\mathbf{v}$, where $\bar{\mathbf{v}}$ denotes a vector in the lab frame and $\mathbf{v}$ denotes a vector in the local frame. Here $s \in [0, L_0]$ is the material coordinate of a rest-length L_0 rod, L denotes the deformed filament length and t is time. If the rod is unsheared, $\bar{\mathbf{d}}_3$ points along the centerline tangent $\partial_s\bar{\mathbf{x}} = \bar{\mathbf{x}}_s$

while $\bar{\mathbf{d}}_1$ and $\bar{\mathbf{d}}_2$ span the normal-binormal plane. Shearing and extension shift $\bar{\mathbf{d}}_3$ away from $\bar{\mathbf{x}}_s$, which can be quantified with the shear vector $\boldsymbol{\sigma} = \mathbf{Q}\left(\bar{\mathbf{x}}_s' - \bar{\mathbf{d}}\right)_3 = \mathbf{Q}\bar{\mathbf{x}}_s' - \mathbf{d}_3$ in the local frame (Figure 4-20b). The curvature vector $\boldsymbol{\kappa}$ encodes $\mathbf{Q}$'s rotation rate along the material coordinate $\partial_s \mathbf{d}_j = \boldsymbol{\kappa} \times \mathbf{d}_j$, while the angular velocity $\boldsymbol{\omega}$ is defined by $\partial_t \mathbf{d}_j = \boldsymbol{\omega} \times \mathbf{d}_j$. We also define the velocity of the centerline $\bar{\mathbf{v}} = \partial_t \bar{\mathbf{x}}$ and, in the rest configuration, the bending stiffness matrix **B,** shearing stiffness matrix **S**, second area moment of inertia **I**, cross-sectional area A and mass per unit length ρ. Thus the dynamics of a soft slender body is then described by:

$$\rho A \cdot \partial_t^2 \bar{\mathbf{x}} = \partial_s \left(\frac{\mathbf{Q}^T \mathbf{S} \boldsymbol{\sigma}}{e} \right) + e \bar{\mathbf{f}} \qquad \text{(Equation 6)}$$

$$\frac{\rho \mathbf{I}}{e} \cdot \partial_t \boldsymbol{\omega} = \partial_s \left(\frac{\mathbf{B}\boldsymbol{\kappa}}{e^3} \right) + \frac{\boldsymbol{\kappa} \times \mathbf{B}\boldsymbol{\kappa}}{e^3} + \left(\mathbf{Q} \frac{\bar{\mathbf{x}}_s}{e} \times \mathbf{S}\boldsymbol{\sigma} \right) + \left(\rho \mathbf{I} \cdot \frac{\boldsymbol{\omega}}{e} \right) \times \boldsymbol{\omega} + \frac{\rho \mathbf{I} \boldsymbol{\omega}}{e^2} \partial_t e + e\mathbf{c} \qquad \text{(Equation 7)}$$

where Equation 6 and 7 represent linear and angular momentum balance at every cross section, $e = |\bar{\mathbf{x}}_s'|$ is the local stretching factor, and $\bar{\mathbf{f}}$ and $\mathbf{c}$ are the external force and couple line densities, respectively. The discretized model is also shown in Figure 4-20c, which is implemented numerically (37).

Interactions Between Filaments The connection between the beam and the pillar is established through force and torque exchanges. Consider the scenario where node $\mathbf{x}_{1(j+1)}$ in rod R_1 is stuck onto node $\mathbf{x}_{2(j+1)}$ in rod R_2, while R_1 and R_2 are perpendicular with respect to each other, as shown in Figure 4-20.c. Thus the constraining forces exerted to both nodes are proportional to the position difference:

$$\mathbf{F}_c = k(\mathbf{x}_{2(j+1)} - \mathbf{x}_{1(j+1)}) \qquad \text{(Equation 8)}$$

where k is the connecting stiffness of the joint. To ensure the verticality, any off-positional displacement should be eliminated by applying restoring torques $\boldsymbol{\tau}_c$ on adjacent segments, which are derived as

$$\varepsilon = [(\mathbf{x}_{2j} - \mathbf{x}_{2(j+1)}) \cdot \mathbf{n}]\mathbf{n} \quad \text{(Equation 9)}$$

$$\boldsymbol{\tau_c} = (\mathbf{x}_{2j} - \mathbf{x}_{2(j+1)} + \varepsilon) \times (\gamma\varepsilon) \quad \text{(Equation 10)}$$

where ε is an infinitesimal displacement, and $\mathbf{x}_{2j}$ denotes the nearest node from $\mathbf{x}_{2(j+1)}$. $\mathbf{n}$ is the normal vector of the plane defined by the beam and the pillar, and γ represents the rotating stiffness of the joint.

We also introduce collision checking between the filaments representing the muscles and the pillars (Figure 4-20c). The separating force is composed of linear elastic term, proportional to the interpenetration displacement, and a damping component that brings energy dissipation into the system for the better convergence. The force is then stated as

$$\mathbf{F_s} = H(\varepsilon)[\beta\varepsilon + \eta(\mathbf{v}_{1i} - \mathbf{v}_{2j}) \cdot \mathbf{d}_{min}^{ij}]\mathbf{d}_{min}^{ij} \quad \text{(Equation 11)}$$

where $\mathbf{d}_{min}^{ij}$ is the minimum distance vector between the two rods, rendering the interpenetration to be $\varepsilon = (r_{1i} + r_{2j} - d_{min}^{ij})$. r_{1i} and r_{2j} denote the radii of the segments that are in contact, with $\mathbf{v}_{1i}$ and $\mathbf{v}_{2j}$ indicating their velocities. $H(\varepsilon)$ is the Heaviside function governed by the sign of ε, while β and η are the stiffness and damping factors respectively.

Table 4-1 Parameters used in simulations

Parameters	Values	Parameters	Values
Skeleton Young's Modulus [a]	$319.4\ KPa$	Skeleton Density [a]	$1.12 \times 10^{-3}\ g/mm^3$
Muscle Young's Modulus	$25.0\ KPa$(49)Error! Bookmark not defined.	Muscle Density	$1.06 \times 10^{-3}\ g/mm^3$ (50)
Poisson Ratio [b]	0.5(51)	Muscle Cross-sectional area [a]	$0.687\ mm^2$
Static Friction Coefficient	0.42 (52)	Dynamic Friction Coefficient	0.3 (52)
k, β	10^8~5×10^8	η	1
γ	5×10^4		

[a] Material properties and geometrical parameters used in the experimental design

[b] Muscular incompressible material assumption

4.7 REFERENCES

1. B. J. Williams, S. V. Anand, J. Rajagopalan, M. T. A. Saif, A self-propelled biohybrid swimmer at low Reynolds number. *Nat. Commun.* **5**, 3081 (2014).

2. R. D. Kamm, R. Bashir, Creating Living Cellular Machines. *Ann. Biomed. Eng.* **42**, 445–459 (2014).

3. R. M. Duffy, A. W. Feinberg, Engineered skeletal muscle tissue for soft robotics: fabrication strategies, current applications, and future challenges: Engineered skeletal muscle tissue for soft robotics. *Wiley Interdiscip. Rev. Nanomed. Nanobiotechnol.* **6**, 178–195 (2014).

4. J. C. Nawroth, *et al.*, A tissue-engineered jellyfish with biomimetic propulsion. *Nat. Biotechnol.* **30**, 792 (2012).

5. B. McInroe, *et al.*, Phototactic guidance of a tissue-engineered soft-robotic ray. *Science* **353**, 154–158 (2016).

6. C. Cvetkovic, *et al.*, Three-dimensionally printed biological machines powered by skeletal muscle. *Proc. Natl. Acad. Sci.* **111**, 10125–10130 (2014).

7. V. Chan, *et al.*, Development of Miniaturized Walking Biological Machines. *Sci. Rep.* **2** (2012).

8. P. Bajaj, R. M. Schweller, A. Khademhosseini, J. L. West, R. Bashir, 3D biofabrication strategies for tissue engineering and regenerative medicine. *Annu. Rev. Biomed. Eng.* **16**, 247–276 (2014).

9. W. Bian, B. Liau, N. Badie, N. Bursac, Mesoscopic hydrogel molding to control the 3D geometry of bioartificial muscle tissues. *Nat. Protoc.* **4**, 1522–1534 (2009).

10. V. Chan, *et al.*, Directed cell growth and alignment on protein-patterned 3D hydrogels with stereolithography: In this tissue engineering application, PEG-based hydrogels with different fibronectin patterns were fabricated and the influence of the protein patterns on shape and direction of seeded cells was studied. *Virtual Phys. Prototyp.* **7**, 219–228 (2012).

11. M. P. Lutolf, J. A. Hubbell, Synthetic biomaterials as instructive extracellular microenvironments for morphogenesis in tissue engineering. *Nat. Biotechnol.* **23**, 47 (2005).

12. M. Calisti, G. Picardi, C. Laschi, Fundamentals of soft robot locomotion. *J. R. Soc. Interface* **14** (2017).

13. J. L. Drury, D. J. Mooney, Hydrogels for tissue engineering: scaffold design variables and applications. *Biomaterials* **24**, 4337–4351 (2003).

14. V. Chan, *et al.*, Multi-material bio-fabrication of hydrogel cantilevers and actuators with stereolithography. *Lab Chip* **12**, 88–98 (2012).

15. M. S. Sakar, *et al.*, Formation and Optogenetic Control of Engineered 3D Skeletal Muscle Bioactuators. *Lab. Chip* **12**, 4976–4985 (2012).

16. J. H. Jeong, *et al.*, "Living" Microvascular Stamp for Patterning of Functional Neovessels; Orchestrated Control of Matrix Property and Geometry. *Adv. Mater.* **24**, 58–63 (2012).

17. C. Cvetkovic, *et al.*, Investigating the Life Expectancy and Proteolytic Degradation of Engineered Skeletal Muscle Biological Machines. *Sci. Rep.* **7**, 3775 (2017).

18. T. Shimizu, *et al.*, Fabrication of Pulsatile Cardiac Tissue Grafts Using a Novel 3-Dimensional Cell Sheet Manipulation Technique and Temperature-Responsive Cell Culture Surfaces. *Circ. Res.* **90**, e40–e48 (2002).

19. R. Raman, C. Cvetkovic, R. Bashir, A modular approach to the design, fabrication, and characterization of muscle-powered biological machines. *Nat. Protoc.* **12**, 519–533 (2017).

20. C. S. Cheng, B. N. Davis, L. Madden, N. Bursac, G. A. Truskey, Physiology and metabolism of tissue-engineered skeletal muscle. *Exp. Biol. Med.* **239**, 1203–1214 (2014).

21. M. Linari, *et al.*, Force generation by skeletal muscle is controlled by mechanosensing in myosin filaments. *Nature* **528**, 276 (2015).

22. R. H. Fitts, K. S. McDonald, J. M. Schluter, The determinants of skeletal muscle force and power: their adaptability with changes in activity pattern. *J. Biomech.* **24 Suppl 1**, 111–122 (1991).

23. S. Gehlert, *et al.*, High force development augments skeletal muscle signalling in resistance exercise modes equalized for time under tension. *Pflugers Arch.* **467**, 1343–1356 (2015).

24. W. Herzog, T. R. Leonard, Force enhancement following stretching of skeletal muscle: a new mechanism. *J. Exp. Biol.* **205**, 1275–1283 (2002).

25. R. Raman, *et al.*, Optogenetic skeletal muscle-powered adaptive biological machines. *Proc. Natl. Acad. Sci.* **113**, 3497–3502 (2016).

26. M. Gazzola, L. Dudte, A. G. McCormick, L. Mahadevan, Dynamics of soft filaments that can stretch, shear, bend and twist (2016).

27. E. Cosserat, jt. auth.) Cosserat F. (François), *Théorie des corps déformables* (Paris, 1909) (January 7, 2018).

28. Z.-Q. Liu, Scale space approach to directional analysis of images. *Appl. Opt.* **30**, 1369–1373 (1991).

29. S. L. Rowe, S. Lee, J. P. Stegemann, Influence of Thrombin Concentration on the Mechanical and Morphological Properties of Cell-seeded Fibrin Hydrogels. *Acta Biomater.* **3**, 59–67 (2007).

30. D. E. Rassier, B. R. MacIntosh, W. Herzog, Length dependence of active force production in skeletal muscle. *J. Appl. Physiol.* **86**, 1445–1457 (1999).

31. M. Lovett, K. Lee, A. Edwards, D. L. Kaplan, Vascularization Strategies for Tissue Engineering. *Tissue Eng. Part B Rev.* **15**, 353–370 (2009).

32. R. N. Palchesko, L. Zhang, Y. Sun, A. W. Feinberg, Development of Polydimethylsiloxane Substrates with Tunable Elastic Modulus to Study Cell Mechanobiology in Muscle and Nerve. *PLOS ONE* **7**, e51499 (2012).

33. A. J. Engler, *et al.*, Myotubes differentiate optimally on substrates with tissue-like stiffness. *J. Cell Biol.* **166**, 877–887 (2004).

34. H. Duong, B. Wu, B. Tawil, Modulation of 3D Fibrin Matrix Stiffness by Intrinsic Fibrinogen–Thrombin Compositions and by Extrinsic Cellular Activity. *Tissue Eng. Part A* **15**, 1865–1876 (2009).

35. J. E. Johnson, B. J. Wold, S. D. Hauschka, Muscle creatine kinase sequence elements regulating skeletal and cardiac muscle expression in transgenic mice. *Mol. Cell. Biol.* **9**, 3393–3399 (1989).

36. J. Rouwkema, B. F. J. M. Koopman, C. A. V. Blitterswijk, W. J. A. Dhert, J. Malda, Supply of Nutrients to Cells in Engineered Tissues. *Biotechnol. Genet. Eng. Rev.* **26**, 163–178 (2009).

37. M. Gazzola, L. H. Dudte, A. G. McCormick, L. Mahadevan, Computational mechanics of soft filaments. *ArXiv160700430 Cond-Mat Physicsphysics* (2016) (February 10, 2018).

38. R. Horowits, E. S. Kempner, M. E. Bisher, R. J. Podolsky, A physiological role for titin and nebulin in skeletal muscle. *Nature* **323**, 160–164 (1986).

39. L. Wang, *et al.*, Patterning Cellular Alignment through Stretching Hydrogels with Programmable Strain Gradients. *ACS Appl. Mater. Interfaces* **7**, 15088–15097 (2015).

40. A. Tondon, R. Kaunas, The Direction of Stretch-Induced Cell and Stress Fiber Orientation Depends on Collagen Matrix Stress. *PLoS ONE* **9** (2014).

41. H. Aubin, *et al.*, Directed 3D cell alignment and elongation in microengineered hydrogels. *Biomaterials* **31**, 6941–6951 (2010).

42. L. Ricotti, *et al.*, Biohybrid actuators for robotics: A review of devices actuated by living cells. *Sci. Robot.* **2**, eaaq0495 (2017).

43. Y. Tanaka, *et al.*, An actuated pump on-chip powered by cultured cardiomyocytes. *Lab. Chip* **6**, 362–368 (2006).

44. K. Shimizu, *et al.*, Assembly of skeletal muscle cells on a Si-MEMS device and their generative force measurement. *Biomed. Microdevices* **12**, 247–252 (2010).

45. V. A. Webster, E. L. Hawley, O. Akkus, H. J. Chiel, R. D. Quinn, Effect of actuating cell source on locomotion of organic living machines with electrocompacted collagen skeleton. *Bioinspir. Biomim.* **11**, 036012 (2016).

46. M. Peckham, Engineering a multi-nucleated myotube, the role of the actin cytoskeleton. *J. Microsc.* **231**, 486–493 (2008).

47. C. c Yuan, *et al.*, Submicron-grooved culture surface extends myotube length by forming parallel and elongated motif. *IET Micro Nano Lett.* **8**, 440–444 (2013).

48. Y. Morimoto, M. Kato-Negishi, H. Onoe, S. Takeuchi, Three-dimensional neuron–muscle constructs with neuromuscular junctions. *Biomaterials* **34**, 9413–9419 (2013).

49. B. C. W. Kot, Z. J. Zhang, A. W. C. Lee, V. Y. F. Leung, S. N. Fu, Elastic modulus of muscle and tendon with shear wave ultrasound elastography: variations with different technical settings. *PloS One* **7**, e44348 (2012).

50. J. Mendez, A. Keys, Density and composition of mammalian muscle. (1961) (December 26, 2019).

51. C. W. J. Oomens, M. Maenhout, C. H. van Oijen, M. R. Drost, F. P. Baaijens, Finite element modelling of contracting skeletal muscle. *Philos. Trans. R. Soc. Lond. B. Biol. Sci.* **358**, 1453–1460 (2003).

52. S. Kheirandish, E. Jabbari, Effect of surface polarity on wettability and friction coefficient of silicone rubber/poly(acrylic acid) hydrogel composite. *Colloid Polym. Sci.* **284**, 1411–1417 (2006).

CHAPTER 5: CONCLUSIONS AND FUTURE DIRECTIONS

5.1 FUTURE DIRECTIONS

5.1.1 ASSEMBLY OF NEUROMUSCULAR BIOLOGICAL MACHINES

5.1.1.1 Determining appropriate culture conditions for long term stable bio-machine viability

From the data presented in this work, the next logical step is to take advantage of the biofabrication advances and install the neural tissue onto the muscle tissue and examine the processes to promote adhesion of these two tissue constructs and functional innervation. The latter was shown to be successful by simply placing the neural tissue on top of the junction bot muscle construct and incubating for 30 minutes (Figure 5-1a). Due to fibrin-fibrin interaction, this results in such strong adhesion that allows for the walker to be flipped, while the neural tissue remains adhered (Figure 5-1b). Furthermore, given that the neural tissue was optogenetic, some effective interaction was shown through the optical stimulation of the neuron which resulted in the contractile response from the non-optogenetic muscle (Figure 5-2a). However, given the spastic-like muscle response (contrary to the desired coordinated contraction), it was clear that the interaction was still not a functional one (i.e. resulting from stable neuromuscular junctions). While allowing to mature, assembled co-cultures were monitored while also stimulating the neurons and observing the muscle response. This not only showed that the muscles' response in response to the neural stimulation diminished with time, but that the spontaneous twitching of the muscle also subsided (Figure 5-2b).

Fearing that the health of the muscle was compromised, co-culture experiments were replicated, only this time electrical field was applied to the entire structure. This should have resulted in a stimulation of both the neural tissue and the muscle tissue. Therefore, even if the

neuromuscular interaction was being somehow impeded, a healthy muscle would still show coordinated contractions in response to the electrical pulses. However, within 72hrs, electrical stimulation stopped having effect on the muscle construct altogether (Figure 5-3). This indicated that the arrangement of the assembly was not only ineffective for developing functional interaction but was adversely affecting the myogenic health of the construct.

In the body, the spinal cord extends processes in the form of nerve extensions throughout the muscle fibers in the body, innervating each one individually. Furthermore, both tissues have their individual set of supporting cells that provide essential nutrients and growth factors specific to the functionality of the different cell types. While NMJ-driven functionality has been shown *in-vitro* to a certain extent, a lot is still unknown about the proper conditions needed to co-culture heterotypic constructs composed of neurons and muscle. For one, mimicking the body conditions seems to not be viable as these would share general media and thus nutrients, and the spatial arrangements as seen in mammals cannot be exactly reproduced for obvious technological limitations. Therefore, studies are required to determine effective media cocktails for the development of stable and functional NMJs. These would also include study of necessary growth factors and possible time dependence of these growth factors with respect to the maturation of the NMJ, similar to the time dependence of factors during the differentiation of stem cells. Furthermore, determining a compatible spatial arrangement that would effectively catalyze innervation might be required, whether it would require physical separation by an ECM or a fibroblast or endothelial barrier or a displacement in the positioning of the activating neural tissue with respect to the actuating muscle.

5.1.1.2 Implementing design principles to optimize and enhance emergence of functionality

The main factor towards achieving functional NMJs revolves around the adequate assembling of neural and muscle constructs such that the MuSK pathway is effectively activated. Once activated, MuSK initiates postsynaptic differentiation, preparing the muscle for innervation, through the clustering of Acetylcholine Receptors and secretion of factors that signal axons. Motor axons recognize the prepatterned muscle fibers, causing them to differentiate into specialized junctions. Therefore, since this pathway includes bidirectional communication that drives both muscle and neurons towards NMJ formation, engineering methods to trick the activation of this pathway could lead to global functional and stable innervation.

While MuSK becomes activated to a degree spontaneously in skeletal muscle, a molecule that catalyzes this activation is the agrin protein. Thus, an idea to achieve this activation is the integration of local agrin signaling. This can be achieved by the conjugation of agrin on beads that have a diameter similar to nerve terminals. These conjugated beads can be embedded during the engrafting of the myotubes in the liquid hydrogel. During compaction and muscle development, the conjugated agrin can drive the prepatterning of acetylcholine receptors. This would in turn catalyze the NMJ formation and differentiation when the neurons are allowed to extend processes across the prepatterned muscle. Through these means, this engineered emergence would also result in an interactive functionality capable of driving actuation (i.e. walking) of larger scaled biological machines.

5.1.1.3 Improving biofabrication method for neuromuscular heterotypic living constructs

While modularity is in many ways an asset to the engineering of these systems, they have a major downside: they require a substantial amount of manual processing. This manual handling

introduces a lot of heterogeneity in the system, which can result in variability and error. It follows that as more modular steps are added, the error propagation would only increase, resulting in systems that would not be reliable. As it stands, the proposed paths of assembly for heterotypic systems involve such large numbers of manual modular steps.

To address this, advances in biofabrication presented in this dissertation and proposed in the previous sections could be used to develop molds to integrate both neuronal tissue and muscle tissue in a single structure that would permit parallel development. This mold would likely consist of a similar reservoir used for the junction bot proposed in this dissertation, where the solution of myotubes and hydrogel would be added to permit compaction and tissue maturation. However, this initial reservoir would likely connect to a raised secondary reservoir with a bottom opening exposing the compacted muscle tissue as the "floor" of the secondary reservoir. This would then allow for the hydrogel and neuron solution to compact directly on the muscle, thus removing the necessity for installation of the neural tissue. This improved engineering approach to assembly heterotypic biological systems would greatly depend on the constraints and parameters determined in previous subsections of section 5.2.2 and would be an excellent example of the interconnection of biological parameters and forward engineering approach that this field is aimed towards.

5.1.2 EXPANDING FUNCTIONALITY OF 3D ENGINEERED NEURAL TISSUE

5.1.2.1 Engineering programming through training regimens in 3D neural tissue

In this dissertation a new approach to neural function modulation was provided by using a training regimen which consistent of a specific optogenetic pulse sequence applied for an hour every 24hrs. This finding evokes a series of intriguing questions. Were the resulting modulations

seen in the frequency profile as a function of the stimulation frequency? Would other frequencies for the stimulation protocol cause a different resulting frequency profile in the developed network? Would changing the rate of making the networks undergo the training regimens or prolonging the regimen itself enhance the effects seen in the networks or would they alter them altogether? These questions would require numerous splits and sample numbers but would be exceedingly useful in elucidating fundamental parameters towards the programming of engineered neural networks. Furthermore, this would result in an essential tool in translating these findings to the much more tissue engineering-relevant 3D tissues.

5.1.2.2 Engineering spatial tissue morphologies by connecting circuit specific neural phenotypes in 3 dimensions

One limitation of the biofabrication protocol of neural tissue mimics presented in this dissertation is the lack of control of neural populations in 3 dimensions. In the brain, neurons that do similar function cluster together, and interconnect across the regions. In a similar fashion driving differentiation of separate stem cells towards the enrichment of specific neurons such as excitatory, inhibitory and cholinergic neurons and then assembling them together could potentially improve the control in functionality of the tissue and enable the engineering of higher order complexity. Furthermore, certain clusters could be transfected to express channelrhodopsin, and thus be designated as input nodes for the 3D network. The goal would be to utilize controlled secretion of neurotransmitters to evoke and control activity of a neural tissue, by engineering tissues with specific phenotypes that can serve as input for other tissues grown in parallel and treated as the output nodes.

As a proof of concept, neurotransmitters with activation of ligand activated channel receptor pathways should be targeted first, due to their faster response time and ligand-specific response (i.e. it specifically responds inhibitory or excitatory to a specific ligand). On the other hand, metabotropic receptors would be hard to control, since they can have more nuanced activation pathways, at many times being both excitatory and inhibitory, while also being slower.

Something to consider in the design of this biological system is that a high (i.e. unbalanced) inhibitory/excitatory population would surely deteriorate or force the network to regulate and adapt likely by either expression of receptors that would equilibrate or through corresponding potentiation or depotentiation of synapses. Therefore, this should suggest that there would be a time dependence to the co-culture of the different type of nerve tissues that adequately aligns with the differentiation and maturation of the different populations.

5.1.2.3 Enhancing functionality of 3D engineered neural tissue through integration of conductive biocompatible materials

A major focus of this field is to achieve hyper-organs by forward engineering the functionality of the engineered biological systems beyond the functionality achieved endogenously by these systems. One approach is to integrate biocompatible biomaterials. Reduced graphene oxide has been shown to improve development of other electroactive cells, such as muscle cells, while neurons grown on graphene sheets have shown to improve their development. A possible explanation is the improvement of conductivity of the ECM may be aiding in the development of these constructs. Due to the connectivity presented in the neural tissue mimics proposed in this dissertation, along with the flexibility of arranging micro-electrodes in convenient arrays, acceleration of action potential propagation in response to the

presence of conductive microstructures, such as reduced graphene oxide embedded in the ECM, could be studied and designed. With this in mind, integrating reduced graphene oxide in 3D neural constructs in order to achieve higher levels of functionality, connectivity and signal transfer would be a relevant study towards determining biohybrid methods to engineer neural constructs to be implemented in neural-related engineered multi-cellular living systems.

5.2 FIGURES

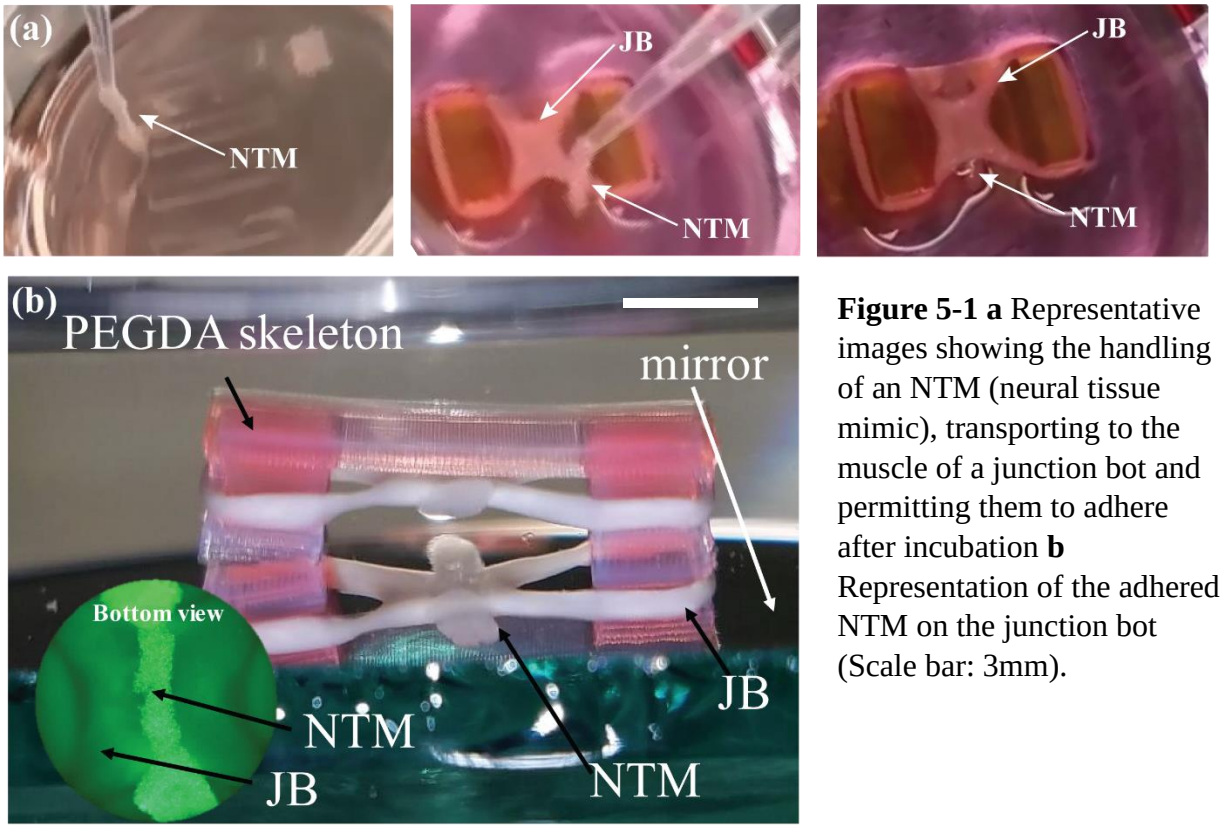

Figure 5-1 a Representative images showing the handling of an NTM (neural tissue mimic), transporting to the muscle of a junction bot and permitting them to adhere after incubation **b** Representation of the adhered NTM on the junction bot (Scale bar: 3mm).

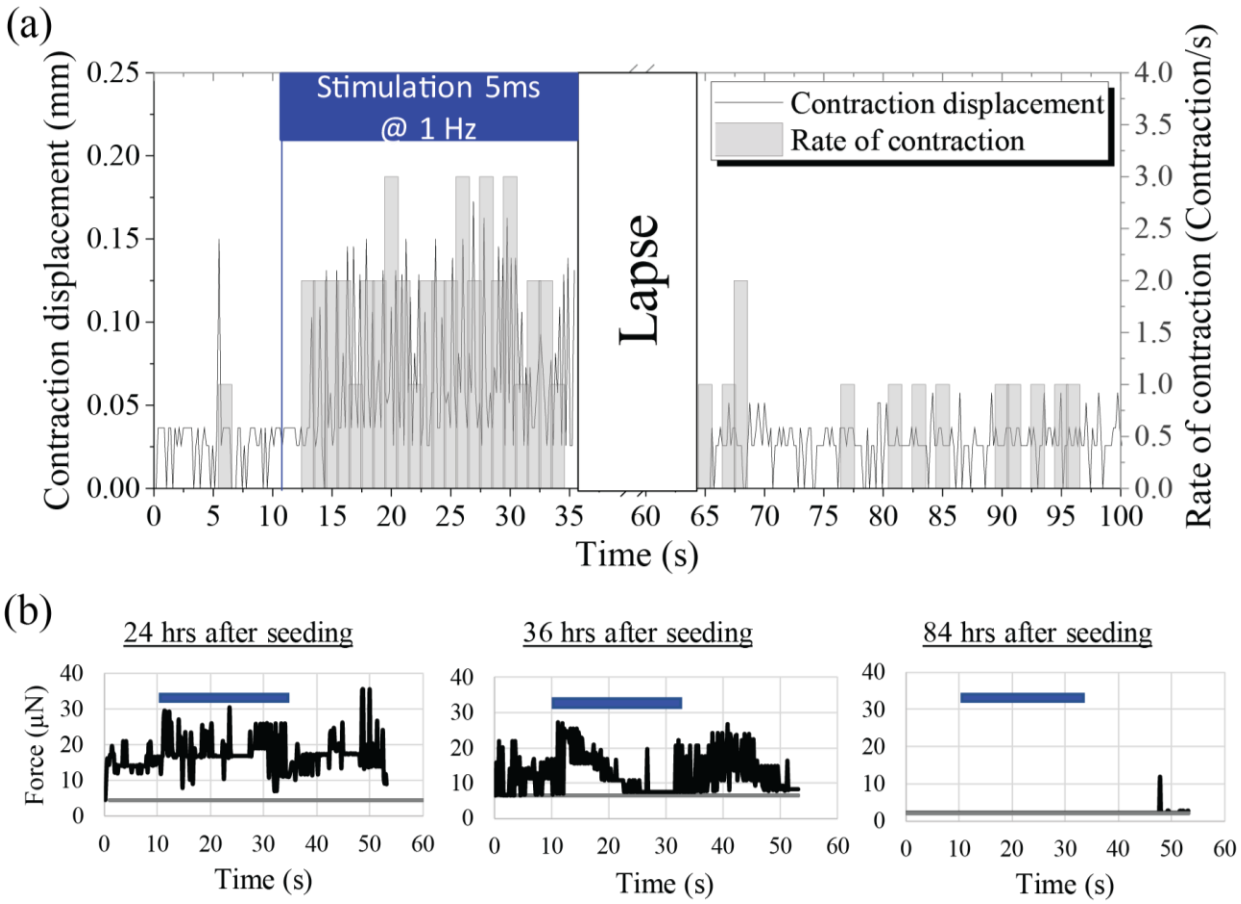

Figure 5-2 Response of muscle to optogenetic stimulation of adhered NTM **a** Plot showing the contraction displacement (left) and the rate of contraction(right) of a muscle from a junction bot as a result of the excitation of a neural tissue mimic through optogenetic stimulation. **b** Force generated by muscle as a result of stimulation of the adhered neural tissue at three different time points after adhering the NTM.

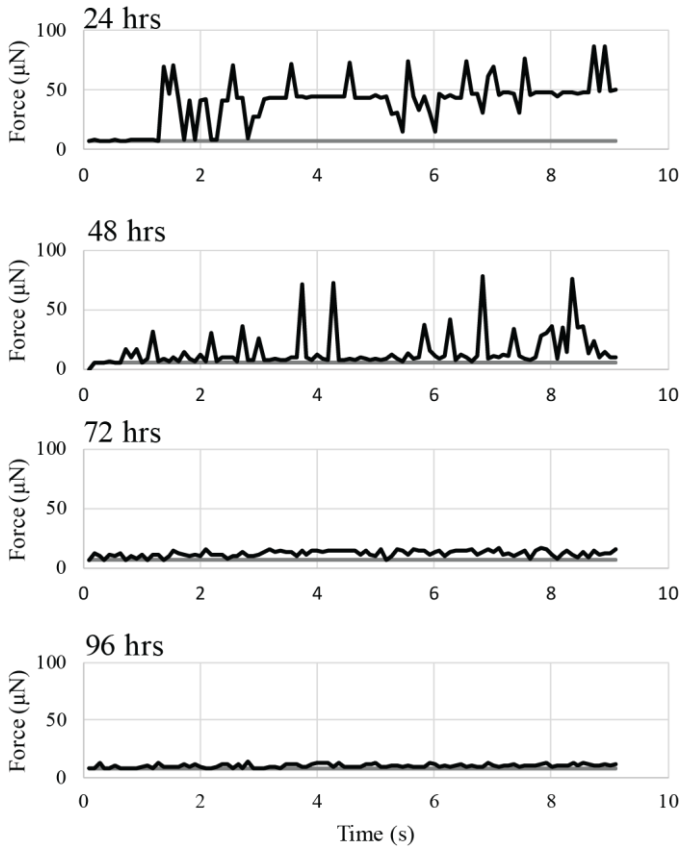

Figure 5-3 Force generation of a JB-NTM construction as a result of 1Hz global electrical stimulation at different time point after installation of the NTM.

5.3 CLOSING STATEMENTS

The present dissertation is a part of a focused effort within a quickly growing field of engineering complex, multi-cellular systems. This field combines concepts of synthetic biology, stem cell biology, tissue engineering and biomaterials, among others to guide the creation and understanding of the behavior of tissue constructs. With these tools, multiple studies have successfully proposed numerous kinds of biological machines as well as engineering heterotypic constructs that show successfully functional interactions. The trend of these advances indicates that there is a great potential in the use of multiple cells as smart biomaterials and guide the implementation of their cell specific functions to engineer higher-order forms of living machines. The implications of this goal propose a new engineering approach to understand the underlying

principles of the complexity observed in mammalian organisms. This in turn lays the groundwork for a functionality-driven conceptual designs of models designated for biomedical research as well as other real-world applications. Works like the one presented in this dissertation compose essential efforts that are needed to develop the nascent ideas in this emerging field. Nevertheless, in the humbling dancing process of understanding the rules of biology, while trying to direct them, even bend them and access the rich potential of functionalities found in the complexity of mammalian systems lies a beauty, an artistic architecture and a scientific challenge that would and should inspire every single engineer.